Stack Level Modeling and Validation of Low Temperature Fuel Cells and Systems for Active Water Management

by

Denise A. McKay

A dissertation submitted in partial fulfillment
of the requirements for the degree of
Doctor of Philosophy
(Environmental Engineering)
in The University of Michigan
2008

Doctoral Committee:

Professor Nikolaos D. Katopodes, Co-Chair
Professor Anna G. Stefanopoulou, Co-Chair
Associate Professor Aline J. Cotel
Associate Professor Christian M. Lastoskie

To my backpacking buddy, who has shown me the world...

Acknowledgments

First and foremost, I would like to thank my advisor, Dr. Anna Stefanopoulou, for providing me with both the rigor and the flexibility that I needed to succeed, along with a willingness to consider my unconventional approaches. I would also like to thank the many other professors at the University of Michigan, including Drs. Nikolaos Katopodes, Aline Cotel, Huei Peng, Christian Lastoskie, and Jeff Cook, who provided tremendous perspective, insight and encouragement throughout my graduate education. I have been fortunate to have such strong mentors that have each played a pivotal role in shaping my studies.

I would also like to gratefully acknowledge support from the U.S. Army Center of Excellence for Automotive Research at the University of Michigan, the National Science Foundation, and the U.S. Department of Energy who have funded my graduate research. In particular, Heather McKee, Erik Kallio, and Dr. Hosam Fathy provided a great deal of support which was critical to the success of my research.

I could not sufficiently give acknowledgement without mentioning the dedicated and humble team of researchers, both past and present, at the Schatz Energy Research Center. The Schatz team opened up a new world for me and quietly fed my passion for a renewable energy future. Special thanks to Ron Reid, Dr. Charles Chamberlin, and Dr. Peter Lehman who gave me a chance. Additionally, I would like to thank the research team at the Fuel Cell Control Laboratory, especially Jason Siegel, and Drs. Buz McCain, Amey Karnik, Ardalan Vahidi, and Katherine Peterson for the many engaging and demanding discussions about research, life and black holes.

Finally, to my family and friends...I could not have achieved this feat without their support. My deepest thanks go to my parents, who sacrificed to give me opportunities they never had and watched me stumble along my own path with loving patience. To all of my grandparents, who have had a profound impact on my life by living theirs fully. I extend my thanks to my brother David, who has always been one step ahead to point out the potholes. Lastly, to Danielle, who endured more than I can possibly imagine.

Acronyms

CFD...	Computational fluid dynamics
DAQ...	Data acquisition
GDL...	Gas diffusion layer
MEA...	Membrane electrode assembly
MFC...	Mass flow controller
ODE...	Ordinary differential equation
OLHP...	Open left half plane
PCI...	Peripheral component interconnect
PDE...	Partial differential equation
PEMFC...	Proton exchange (polymer electrolyte) membrane fuel cell
PI...	Proportional integral
1*D*, 2*D*, 3*D*...	One, two, or three-dimensional
VAC...	Volts alternating current
VDC...	Volts direct current
VFM...	Volumetric flow meter

Symbols

To differentiate theoretical and modeled values, x, from measured data or variables calculated using measurements, $\bar{x}$, an overbar is used. Additionally, estimated variables are denoted with a hat, $\hat{x}$. Time derivatives are denoted as $d()/dt$. Spatial derivatives are denoted as $\partial()/\partial y$.

A list of the variable symbols, definitions and units is provided below, any deviations from these units will be explicitly stated in the text:

$a\ldots$	water activity (unitless) or temperature amplitude (K)
$c\ldots$	molar concentration (mol/m^3)
$\langle D\rangle\ldots$	effective diffusivity (m^2/s)
$e\ldots$	error signal
$E\ldots$	open circuit voltage (V)
$h\ldots$	enthalpy (J/kg)
$\bar{h}\ldots$	heat transfer coefficient (W/m^{2}K)
$i\ldots$	current density (A/m^2)
$I\ldots$	PEMFC stack current (A)
$m\ldots$	mass (kg)
$n\ldots$	mole number
$N\ldots$	molar flux (mol/s/m^2)
$p\ldots$	pressure (Pa) or pole location
$p_c\ldots$	capillary pressure (Pa)
$Q\ldots$	heat transfer (W)
$r\ldots$	mass flow ratio
$R_{evap}\ldots$	evaporation rate (mol/s m^3)
$s\ldots$	fraction of liquid water volume to the total volume
$S\ldots$	reduced liquid water saturation
$t\ldots$	time (s)
$T\ldots$	temperature (K)
$U\ldots$	overvoltage (V)
$v\ldots$	total cell voltage (V)
$W\ldots$	mass flow rate (kg/s)
$x\ldots$	mass fraction
$y\ldots$	mole ratio (unitless) or spatial dimension (m)
$\Delta\dot{E}_{st}\ldots$	change in energy stored (J/s)
$\lambda\ldots$	membrane water content (mol H_2O/mol SO_3^-)
$\phi\ldots$	relative humidity (0-1)
$\omega\ldots$	humidity ratio

A list of the parameter symbols, definitions and units is provided below:

$A \ldots$	surface area available for heat transfer (m^2)
$A_{fc} \ldots$	fuel cell nominal active area (m^2)
$C_p \ldots$	constant pressure specific heat (J/kg K)
$C \ldots$	constant volume specific heat (J/kg K)
$D \ldots$	diffusion coefficient (m^2/s)
$D_w \ldots$	membrane vapor diffusion coefficient (m^2/s)
$F \ldots$	Faraday's constant (C/mol e^-)
k	orifice constant (m s)
$k_P \ldots$	controller proportional gain (W/K)
$k_I \ldots$	controller integral gain (W/K^2)
$K \ldots$	absolute permeability (m^2)
$K_{1-4} \ldots$	voltage parameters (various)
$K_{rl} \ldots$	relative permeability
$M \ldots$	molecular weight (kg/mole)
$n_{cells} \ldots$	number of cells in the PEMFC stack
$n_d \ldots$	electro-osmotic drag coefficient (mol H_2O/ mol H^+)
$R \ldots$	ideal gas constant (J/kg K)
$s_{im} \ldots$	level of immobile saturation
$t_{mb} \ldots$	PEMFC membrane thickness (m)
$t_{wl} \ldots$	tunable water layer thickness (m)
$T_s \ldots$	DAQ sample time (sec)
$V \ldots$	volume (m^3)
$\alpha_w \ldots$	tunable diffusion parameter
$\beta \ldots$	heat transfer coefficient parameters
$\delta \ldots$	deviation from nominal conditions
$\delta y \ldots$	discretization width (m)
$\gamma \ldots$	volumetric condensation coefficient (s^{-1})
$\varepsilon \ldots$	material porosity
$\lambda \ldots$	membrane water content (mol H_2O/mol SO_3^-)
$\theta_c \ldots$	contact angle (degrees)
$\mu \ldots$	viscosity (kg/m s)
$\rho \ldots$	density (kg/m^3)
$\sigma \ldots$	surface tension (N/m)
$\zeta \ldots$	damping coefficient

A list of the subscript and superscript symbols and definitions is provided below:

$a\ldots$	air
$amb\ldots$	ambient
$an\ldots$	anode
$bp\ldots$	bypass
$b\ldots$	control volume bulk materials
$c\ldots$	capillary
$ca\ldots$	cathode
$ch\ldots$	channel
$ct\ldots$	catalyst
$da\ldots$	dry air
$e\ldots$	electrode (*an* or *ca*)
$fc\ldots$	fuel cell stack
$gas, g\ldots$	gas constituent
$hm\ldots$	humidifier
$H_2\ldots$	hydrogen
$i, in\ldots$	into the control volume
$j\ldots$	index for gas constituents
$k\ldots$	index for discretization (in time or space)
$l\ldots$	liquid water
$mx\ldots$	mixer
$mb\ldots$	membrane
$N_2\ldots$	nitrogen
$O_2\ldots$	oxygen
$o, out\ldots$	out of the control volume
$p\ldots$	pore
$r\ldots$	reservoir
$rct\ldots$	reactions
$sat\ldots$	saturation
$st\ldots$	stack
$v\ldots$	water vapor
$w\ldots$	water (gas and liquid phase)
$wc\ldots$	water circulation system (humidifier, reservoir and water heater)
$wh\ldots$	water heater
$*\ldots$	desired/reference value
$^o\ldots$	nominal conditions

Table of Contents

Dedication ii

Acknowledgments iii

Acronyms iv

Symbols v

List of Tables xi

List of Figures xii

List of Appendices xv

Abstract xvi

Chapter 1 Background and Introduction 1
1.1 Fuel Cell System Operation 1
1.1.1 Reactant and Water Dynamics in PEMFC Stacks 4
1.1.2 Reactant Gas Humidification 5
1.2 Hardware Overview 6
1.3 Thesis Overview 8
1.4 Contributions 9

Chapter 2 Reactant and Water Dynamics in a PEMFC Stack 11
2.1 Fuel Cell Experimental Hardware 11
2.2 Fuel Cell Modeling Overview 13
2.3 Fuel Cell Nomenclature 16
2.4 General Modeling Assumptions 16
2.5 Gas Diffusion Layer Model Details 17
2.5.1 Liquid Water Capillary Transport 17
2.5.2 Gas Species Diffusion 19
2.6 Discretization of the Spatial Gradients 20
2.7 Boundary Conditions 22
2.7.1 Membrane Boundary Conditions 22
2.7.2 Boundary conditions at the cathode channel 25
2.7.3 Boundary conditions at the anode channel 26
2.8 Output Voltage Equation 27

2.9 Parameter Identification Approach . . . 30
2.10 Model Calibration Results . . . 32
2.10.1 Model Predictions . . . 34
2.10.2 Estimation Sensitivity to Tunable Parameters . . . 37
2.11 Model Validation Results . . . 41

Chapter 3 Membrane Based Humidification System Model . . . 44
3.1 Humidification System Operation . . . 44
3.1.1 System Description . . . 44
3.1.2 Experimental Hardware . . . 46
3.2 Model Development . . . 49
3.2.1 Modeling Assumptions Employed . . . 49
3.2.2 Humidifier Nomenclature . . . 50
3.2.3 Generic Two Volume Thermal Model . . . 50
3.2.4 Water Reservoir Model . . . 53
3.2.5 Water Heater Model . . . 54
3.2.6 Membrane Based Humidifier Model . . . 55
3.2.7 Air Bypass Model . . . 58
3.2.8 Mixer Model . . . 58
3.2.9 Relative Humidity Estimation . . . 60
3.3 Modeling Summary . . . 63
3.4 Parameter Identification . . . 65
3.4.1 Identification Methodology . . . 65
3.4.2 Experimental Identification Results . . . 67
3.5 Model Validation Results . . . 72

Chapter 4 Humidification System Control . . . 77
4.1 Nonlinear Feedforward for Air Mass Flow Control . . . 77
4.2 Reference Temperatures . . . 79
4.3 Plant Linearization . . . 80
4.3.1 Bypass Linearization . . . 82
4.3.2 Water Circulation System Linearization . . . 82
4.3.3 Mixer Linearization . . . 83
4.4 Thermostatic Control . . . 84
4.4.1 Water Circulation System Tuning with Describing Function Method . . . 85
4.4.2 Bypass and Mixer Tuning by Simulation . . . 88
4.5 PI Controller Tuning with Integral Anti-windup . . . 91
4.5.1 Mixer and Bypass PI Gain Tuning . . . 92
4.5.2 Water Heater PI Gain Tuning . . . 94
4.5.3 Integral Anti-windup Strategies . . . 95
4.6 Hardware Implementation of Controllers . . . 98
4.6.1 Models for Emulation of Hardware Constraints . . . 98
4.6.2 Simulated Closed Loop Performance . . . 99
4.6.3 Closed Loop Experimental Results . . . 103

Chapter 5 Conclusions and Future Work . . . 112
5.1 Fuel Cell Reactant and Water Dynamics . . . 112
5.2 Gas Humidification System . . . 113

5.3 Extensions of this Thesis 114
5.3.1 Fuel Cell Modeling and Validation 114
5.3.2 Humidification System 115
5.3.3 Extensions to Other Applications 116

Appendices 117

Bibliography 127

List of Tables

Table

2.1 Parameters required based on PEMFC stack specifications. 30
2.2 PEMFC modeling parameters found from published literature. 31
2.3 Experimentally identified parameter values 34
3.1 Sensor and Controller Specifications. 48
3.2 Calibrated model parameters based on material properties. 65
3.3 Tuned humidification system model parameters based on experimental identification. 67
4.1 Nominal conditions used for system linearization. 81
4.2 Open loop response time and DC-gain for the bypass, mixer and water circulation systems as total air mass flow rate is varied from 0.3-0.9 g/s. 81
4.3 Necessary error bounds to achieve desired amplitude for thermostatic regulation. . 85
4.4 Proportional Integral Controller Gains 92

List of Figures

Figure

1.1 Detailed diagram of the materials within a PEMFC and the inputs and outputs of a PEMFC stack. . . . 2
1.2 Schematic of capillary flow of liquid water through the fuel cell gas diffusion layers. 3
1.3 Schematic diagram of a membrane based humidifier. . . . 5
1.4 Test bench at the Fuel Cell Control Laboratory, University of Michigan. . . . 7
1.5 Schematic of the test bench hardware, including the computer interface as well as the hydrogen, air and water circulation subsystems. . . . 7
2.1 Experimental hardware employed and measurement locations. . . . 12
2.2 Instrumented PEMFC stack installed at the Fuel Cell Control Laboratory, University of Michigan. . . . 13
2.3 Experimental data comparing the impact of anode purging and cathode surging events on cell voltage. . . . 14
2.4 Flow chart of GDL model calculation algorithm. . . . 15
2.5 Spatial discretization of the gas diffusion layers. . . . 20
2.6 Summary of the calculation procedure to determine the membrane water vapor flux given GDL section (1) water vapor partial pressures. . . . 25
2.7 Block diagram indicating the inputs and outputs from the GDL and voltage models. 32
2.8 Experimental measurements used for model calibration. . . . 33
2.9 GDL model calibration results. . . . 35
2.10 Reactant dynamics during a load change and anode purging event. . . . 37
2.11 Water dynamics during a load change and anode purging event. . . . 38
2.12 Sensitivity of the voltage parameters on the water related tunable parameters. . . . 39
2.13 Voltage estimation error mean and standard deviation as a function of the water related tunable parameters. . . . 40
2.14 Influence of the water related tunable parameters on the accumulation of liquid water in the anode channel and the resultant voltage estimation. . . . 41
2.15 For fixed voltage parameters, the influence of the water related tunable parameters on the voltage estimation. . . . 42
2.16 GDL model validation results. . . . 43
3.1 External humidifier system overview, detailing the reservoir, water heater, humidifier, bypass, and gas mixer as well as the relationship of the humidification system to the fuel cell stack. . . . 45
3.2 External gas humidification system installed at the Fuel Cell Control Laboratory, University of Michigan. . . . 46
3.3 Schematic of the gas humidification system hardware, detailing sensor and actuator placement. . . . 47

3.4 Plan view of the external humidifier with the individual control volumes labeled. . 49
3.5 General description of the heat transfer mechanisms for control volumes containing bulk and gas states. 51
3.6 Simulation schematic of the general two volume system. 53
3.7 Inputs and outputs of the water reservoir. 54
3.8 Inputs and outputs of the water heater. 55
3.9 Two volume humidifier system. 56
3.10 Inputs and outputs of the air bypass. 58
3.11 Inputs and outputs of the gas mixer. 59
3.12 Experimental inputs to the mixer outlet relative humidity estimator. 61
3.13 Experimental validation of the mixer outlet relative humidity estimation by comparing the measured to estimated relative humidity under the range of operating conditions shown in Figure 3.12. 62
3.14 Temporal variation in the mixer outlet relative humidity estimation compared to the measurement. 62
3.15 Humidifier system indicating states, disturbances and measurements 64
3.16 Bypass experimental parameter identification results. 68
3.17 Mixer experimental parameter identification results. 69
3.18 Reservoir experimental parameter identification results comparing the measured and estimated liquid water outlet temperatures. 70
3.19 Experimental parameter identification results for the water heater control volume. . 70
3.20 Experimental parameter identification results for the humidifier control volume including both the air and liquid water states. 71
3.21 Model structure for open loop simulation of the gas humidification system. 72
3.22 Bypass experimental validation results. 73
3.23 Reservoir experimental validation results. 73
3.24 Water heater experimental validation results. 74
3.25 Humidifier experimental validation results. 75
3.26 Mixer experimental validation results. 76
4.1 Schematic of the humidification system control architecture indicating the locations of the temperature references with respect to the states. 78
4.2 Thermostatic differential gap indicating the relationship between the temperature error and the control signal. 84
4.3 Schematic comparing an unshifted versus a shifted relay with hysteresis. 86
4.4 Simulation of the temperature oscillations induced in the water circulation system with relay feedback along with the heater control input. 87
4.5 Influence of the mixer error bound on the simulated mixer outlet temperature limit cycle for a relay feedback system. 89
4.6 Sequential process used to tune the bypass and mixer thermostatic error bounds. . . 89
4.7 Thermostatic controller simulation with tuned deadbands under nominal conditions. 91
4.8 Bode plots of the mixer and bypass closed loop systems indicating gain and phase margins. 94
4.9 Bode plots of the water circulation system closed loop systems indicating gain and phase margins. 95
4.10 Proportional integral control schematic with convergence based integral anti-windup. 96
4.11 Proportional integral control schematic using logic to stop integrating the error signal when the actuator saturates. 96

4.12 Comparison of the reduced order mixer closed loop step response employing the PI controller using different anti-windup strategies. 97
4.13 Thermocouple temperature measurement and noise. 99
4.14 Simulated humidifier air outlet closed loop temperature response to a reference step, comparing the use of PI versus thermostatic control. 100
4.15 Simulated bypass air outlet closed loop temperature response to a reference step, comparing the use of PI versus thermostatic control. 101
4.16 Simulated mixer air outlet closed loop temperature response to a reference step, comparing the use of PI versus thermostatic control. 102
4.17 Simulated mixer gas outlet relative humidity response during a step in the reference temperature, comparing the use of PI versus thermostatic control. 102
4.18 Experimental humidifier air outlet closed loop temperature response to a reference step, comparing the use of PI versus thermostatic control. 103
4.19 Experimental bypass air outlet closed loop temperature response to a reference step, comparing the use of PI versus thermostatic control. 104
4.20 Experimental mixer air outlet closed loop temperature response to a reference step, comparing the use of PI versus thermostatic control. 105
4.21 Estimated experimental mixer gas outlet relative humidity response during a step in the reference temperature, comparing the use of PI versus thermostatic control. . . 106
4.22 Humidifier air outlet temperature thermostatic regulation during step changes in the reference temperature and the desired cathode inlet humidity. 107
4.23 Bypass air outlet temperature thermostatic regulation during a step change in the desired cathode inlet temperature. 108
4.24 Mixer air outlet temperature thermostatic regulation during step changes in the reference temperature and the desired cathode inlet humidity. 109
4.25 Humidification system response for PI regulation during step changes in the reference temperature, desired cathode inlet humidity, a reservoir fill event, and varying ambient temperature. 111
A.1 Experimental back-pressure flow data used to tune the cathode orifice constant. . . 119
A.2 Comparison of the experimental and modeled back-pressure flow relationship for the cathode channel. 120
B.1 Comparison of water sorption curves for Nafion 117 at 80^{o}C and 30^{o}C. 123
B.2 Summary of published water vapor diffusion coefficient models. 126

List of Appendices

Appendix

A Fuel Cell Orifice Constants 118

B A Review of Back Diffusion Models 121

Abstract

Fuel cells are gaining increased attention as viable energy generators for a range of applications. To optimize performance, these systems require active coordination leveraging an understanding of the system dynamics. This thesis describes a reproducible process for modeling, calibrating, and experimentally validating system dynamics for control applications, applied to two membrane-based systems, namely a proton exchange membrane fuel cell (PEMFC) stack and a gas humidification system.

A two-phase dynamic model that predicts the experimentally observed temporal behavior of a PEMFC stack and a methodology to experimentally identify tunable physical parameters, namely the membrane water vapor diffusion coefficient and the thickness of the liquid water film restricting the fuel cell active area, is presented. The temporal calculation of the species concentrations through the gas diffusion layers, the water vapor transport through the membrane, and the degree of water flooding in the gas channels, enables a prediction of temporal voltage degradation. The calibrated model is validated under anode flooding conditions for a 24 cell, 300 cm^2 stack with a supply of pressure-regulated hydrogen.

To regulate the humidity of the supplied reactants to actively manage water within the PEMFC, a membrane based gas humidification system is designed and constructed. This apparatus utilizes a gas bypass and a series of heaters to regulate gas temperature while maintaining the desired relative humidity of the gas supplied to the PEMFC. To design and calibrate the heater controllers, as well as the fraction of air diverted through the bypass, a low order, control-oriented model based on first principles is developed. As with the fuel cell model, the humidification system model is parameterized and validated using experimental data under a wide range of operating conditions. A relative humidity estimator is employed, for the air-vapor mixture leaving the humidifier system (supplied to the PEMFC), to eliminate the need for a bulky and expensive humidity sensor. With this validated model of the humidification system thermal dynamics, on/off and variable heat controllers are designed and tested for accurate and fast humidity control despite changes in the PEMFC air mass flow rate due to load disturbances.

Chapter 1

Background and Introduction

For control applications, a critical step in developing dynamic models is determining the minimal complexity necessary to capture the fundamental dynamics of interest. Several strategies have been used for developing low order models for control applications. These strategies typically apply either physics based or phenomenological tools to predict component and system dynamics. As models generated for use in embedded control must be capable of processing and sampling under the constraints associated with real time digital signal processing, a fundamental tradeoff then exists between model complexity, which impacts controller response time, and the model uncertainty associated with neglecting particular dynamics. For control, the simplest models are desired that are capable of capturing important dynamics under the range of expected system operating conditions.

This work applies first principles in the derivation of control-oriented models to two solid polymeric membrane based systems, namely a fuel cell and a gas humidifier. These two system models are parameterized and experimentally validated with similar sensor measurement and placement constraints. However, these two systems exhibit very different mass and energy transport characteristics as well as response times and actuation constraints. Because these models are intended for use in embedded control, each model is intentionally derived employing low cost input/output measurements, with no sensor information available with respect to the internal states. The ability of these lumped parameter models to capture the dynamic output response of systems with spatially distributed characteristics is of critical importance.

1.1 Fuel Cell System Operation

A fuel cell is an electrochemical engine, different from batteries in that it requires a fuel source. When fuel supply, humidification and cooling systems are well managed, fuel cells provide clean, quiet and reliable power. There are many types of fuel cells currently in development, such as solid oxide or phosphoric acid. The distinction between different types of fuel cells is made based on the electrolyte (transfer ion), and the operating temperature. Polymer electrolyte membrane fuel cells (PEMFCs) hold the most promise for applications demanding low temperatures, pressures, or rapidly changing power demands. Because of the numerous applications to which PEMFCs are

advantageous, such as vehicular or remote applications, PEMFCs are rapidly gaining attention as a promising source of energy. [7] [35]

Typically operating below the boiling point of water, PEMFC stacks utilize the chemical energy from the reaction of hydrogen and oxygen to produce electricity, water and heat. A PEMFC stack consists of numerous fuel cells electrically combined in series. Treating the PEMFC stack as a black box, the basic inputs and outputs are shown in Figure 1.1. Hydrogen gas (fuel) and oxygen from the air are supplied to the individual cells within the stack through internal manifolds. These manifolds direct gas to the individual cells in parallel. The fuel cell provides useful work through an external circuit, where each cell is electrically connected in series.

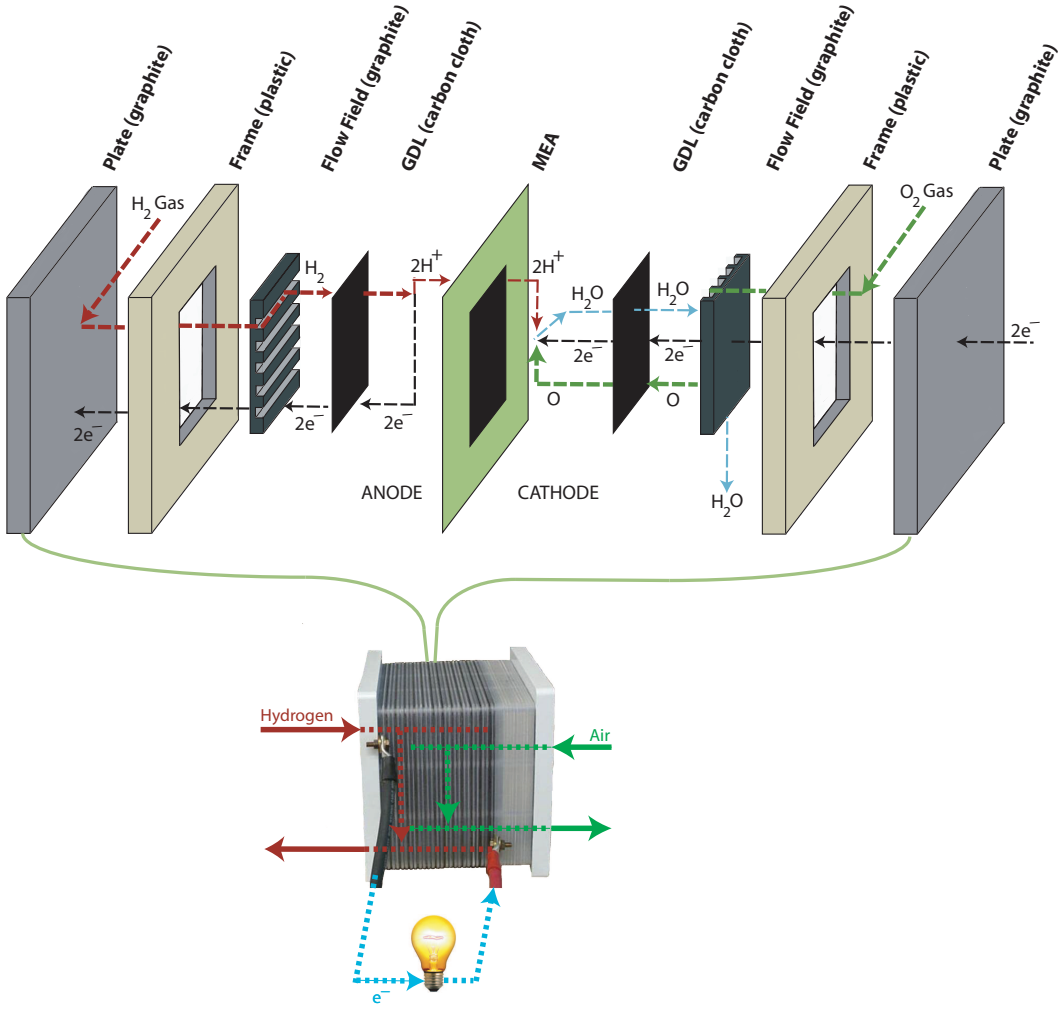

Figure 1.1: Detailed diagram of the materials within a PEMFC and the inputs and outputs of a PEMFC stack.

A detail of the cell structure is also provided in Figure 1.1. Fuel travels from the internal manifolds to flow fields (gas channels), then diffuses through conductive porous gas diffusion layers (GDL) to the thin polymeric membrane. The membrane, sandwiched in the middle of the cell, typically contains catalyst and microporous diffusion layers along with gaskets as a single inte-

grated unit referred to as a Membrane Electrode Assembly (MEA). The catalyst layer at the anode ionizes hydrogen. The membrane permits ion transfer (hydrogen protons), requiring the electrons to flow through an external circuit before recombining with protons and oxygen at the cathode to form water. This migration of electrons through the external circuit produces useful work. The electrochemical half-reactions for the anode and cathode are:

$$\textbf{Anode} \quad 2H_2 \longrightarrow 4H^+ + 4e^-$$

$$\textbf{Cathode} \quad O_2 + 4H^+ + 4e^- \longrightarrow 2H_2O$$

$$\textbf{Overall} \quad 2H_2 + O_2 \longrightarrow 2H_2O$$

The management of water is critical for optimizing performance of a PEMFC stack. Because the ionic conductivity of the membrane is dependent upon its water content [79], a balance must be struck between reactant (hydrogen and oxygen) delivery and water supply and removal. Depending upon the operating conditions of the PEMFC stack, the flow patterns in the anode and cathode channels, and the design of the anode gas delivery system (dead-ended or flow through), this liquid water can accumulate within the gas diffusion layers (GDLs) and channels [23, 51, 70, 82], as shown in Figure 1.2. Whether obstructing reactant flow or reducing the number of active catalyst sites, the impact of flooding is a reduction in the power output of the fuel cell stack, seen by a decrease in cell voltage [10]. Thus, a real-time estimation of the degree of flooding within the cell structure and its impact on the cell electrical output with standard, low cost, and reliable sensors is critical for active water management. Moreover, a low order control-oriented model must be derived for further considering such issues as identifiability, observability, and controllability [39].

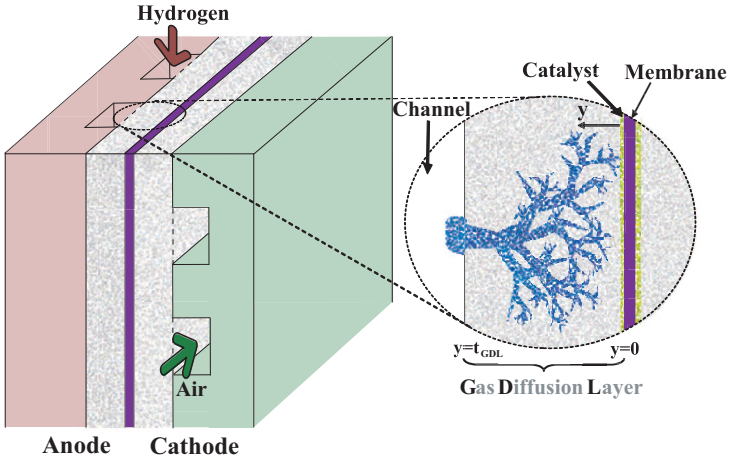

Figure 1.2: Schematic of capillary flow of liquid water through the fuel cell gas diffusion layers.

The work by [27], provided a systematic analysis of the appropriate methodology for removing liquid water accumulating in the electrodes, considering both anode recirculation and the humidity conditions of the supplied reactants. They postulate a need for feedback control to adjust the relative humidity of the supplied air, along with the degree of water removal from the anode, dynamically. With a model of the reactant and water dynamics within a PEMFC, the degree of electrode flooding

and resulting decay in voltage performance can be estimated online in real time. This online estimation can then be coupled with active control of the supplied reactants to manage water within the cell structure.

The following sections survey published literature on two phase PEMFC modeling and experimental techniques employed to image liquid water within the cell structure, followed by the introduction of methodologies used to humidify reactant gases supplied to a PEMFC. Note, the PEMFC stack is used as a power generator, whereas the gas humidification system preconditions the fuel supplied to the generator.

1.1.1 Reactant and Water Dynamics in PEMFC Stacks

To gain a better understanding of reactant and water transport within the GDL and catalyst layers, many CFD models have been developed to approximate the two or three dimensional flow of hydrogen, air, and water at steady-state within the cell structure [5, 16, 18, 50, 77, 78]. Using experimental steady-state polarization (voltage versus current) data for parameter identification, [20] and [6] investigated the sensitivity of the cell performance to the identified parameters. Further, using a model to simulate polarization data with a given set of parameters, constrained quadratic programming was then used to identify these given parameters [68] and address parameter identifiability and uniqueness issues [67].

While these models are ideal for investigating transport phenomena with two phase flow and spatial gradients, examining parameter sensitivity, or the influence of material properties on cell performance, experimental validation of these models, often completed by comparing measured to estimated polarization curves, is still lacking. A few publications with steady-state validation efforts (i) point to a mismatch between model prediction and spatially resolved experimental data [25] indicating that different spatial distributions can correspond to a similar averaged polarization curve [25, 67], and (ii) achieve good prediction of steady-state and spatially resolved current density measurements after tuning parameters to several orders of magnitude of their theoretical values [4].

Although steady-state polarization measurements do not offer a conclusive data set for model validation, the transient polarization response provides useful data for model validation especially during unsteady operation such as flooding [46]. Several transient models have been reported to illicit the relationship between critical material properties and operating conditions on the dynamic fuel cell response [45, 59, 61, 72, 73], however few have been validated against transient experimental data and are of sufficient complexity for implementation in real time control applications.

Control-oriented transient models have been developed to account for the formation of liquid water within the gas channels [52] or within both the channels and the GDL [56], however they do not relate the effect of flooding to decreased cell potential, a key indication of how flooding impacts cell performance. We establish a relationship between flooding and cell performance, as originally introduced in [40] and leveraged by other authors [14], using the notion of apparent current density to relate the accumulation of liquid water in the gas channels to a reduction in the cell active area,

in turn increasing the cell current density and lowering cell voltage.

1.1.2 Reactant Gas Humidification

Membrane-type humidifiers, directing a gas flow across one surface of a polymer membrane and liquid water (or humidified gas) across the other membrane surface, have been used for humidifying PEMFC reactants [55, 60]. Water vapor and thermal energy are exchanged through the membrane from the liquid water to the dry gas. The humidifier membrane is similar to that employed in the PEMFC but without a catalyst or microporous layer. Figure 1.3 provides a general overview of a membrane humidifier.

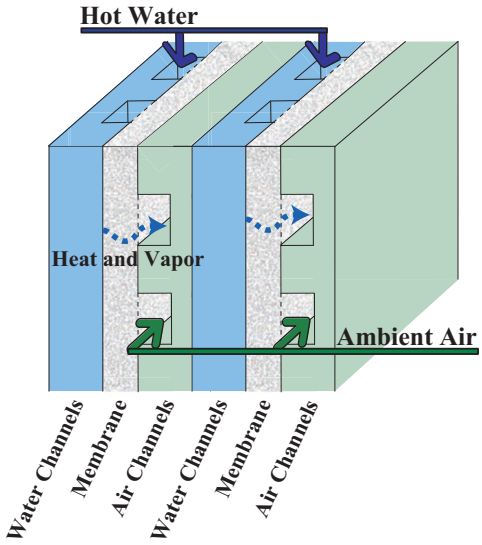

Figure 1.3: Schematic diagram of a membrane based humidifier.

The work in [9], [43], and [66] employs an internal membrane humidifier that is an integrated unit within the PEMFC stack. These internal humidifiers use coolant water leaving the power producing portion of the stack, humidified reactant exhaust streams can also be used, to heat and humidify the incoming reactants. While these internal humidifiers are relatively compact and simple with respect to control, they prohibit active humidity regulation and couple reactant humidity requirements to the PEMFC cooling demands. To overcome the humidity constraints, sliding plates were considered to activate and deactivate gas channels within the humidifier and control the contact area between the liquid and gas [8]; however, this concept has not yet been realized in hardware.

Alternatively, various bubbler or sparger external humidifiers have been developed for independently controlling relative humidity and temperature of gas streams [54, 38]. These devices utilize a column of water through which the reactant streams bubble. To avoid controlling bubble size, these devices are designed with a long column of water (large residence time) to provide a saturated gas stream at a controlled temperature. The relative humidity of the gas stream can then be adjusted by further heating the gas upon exit from the bubbler. While these systems provide a relatively simple method of controlling temperature and relative humidity of reactant streams, they are not tolerant of

large gas flow rates [54] and are relatively heavy and bulky due to the large stored volume of water.

Our methodology decouples the passive humidifier from the PEMFC cooling loop, with the addition of an external bypass, to provide independent control of both temperature and relative humidity irrespective of the stack operating temperature, conceptually similar to that proposed by [75]. The operation of the humidifier consists of a dry reactant gas and liquid water delivered to a membrane humidifier to produce a saturated gas. A different stream of dry reactant gas bypasses the humidifier. The combination of the saturated and dry gas streams produces a reactant-vapor mixture at a desired relative humidity.

For thermal regulation, resistive heaters are used to achieve a desired reactant gas temperature and minimize condensation during the mixing of the saturated and dry reactant streams. To design adequate controllers for thermal regulation (using resistive heaters) and humidity control (for the gas flow split between the humidifier and the bypass), we developed a low order, control-oriented model based on first principles. Similar to engine thermal management systems employing either a valve or servo motor to bypass coolant around the heat exchanger [11, 58, 71], the coordination of the heaters and the bypass valve is challenging during fast transients due to the different time scales, the actuator constraints, and the sensor responsiveness.

1.2 Hardware Overview

Many different experiments were conducted and are described throughout this thesis. First, a model of the reactant and water dynamics of a 24-cell, 300 cm^2 PEMFC stack was experimentally calibrated and validated. Then, a membrane based external humidification system was installed and operated as a stand-alone system to calibrate and experimentally validate a model of the system thermal dynamics. Following the validation of the humidifier system model and controller development, additional experiments were completed to verify the closed loop humidification system controller response.

All experimental hardware presented in this thesis was installed in the Fuel Cell Control Laboratory at the University of Michigan in collaboration with the Schatz Energy Research Center. An image of the test bench is shown in Figure 1.4.

This test bench is comprised of a data acquisition and signal conditioning subsystem, control and monitoring software, a deionized water cooling subsystem, a hydrogen gas delivery subsystem, an air delivery subsystem, an electrical subsystem, and test bench hardware safeties. An overview of the interaction of the main system components is provided in Figure 1.5. Digital input and output (DIO) and analog input and output (AIO) communication is indicated with black and grey dashed lines, respectively.

The control and monitoring system consists of software coded in LabVIEW® and employed on a standard desktop PC computer. This computer is equipped with PCI data acquisition cards connected through a signal conditioning system to the instruments. Analog output signals from the computer are conditioned to the appropriate voltage or current range using Analog Devices 5B

Figure 1.4: Test bench at the Fuel Cell Control Laboratory, University of Michigan.

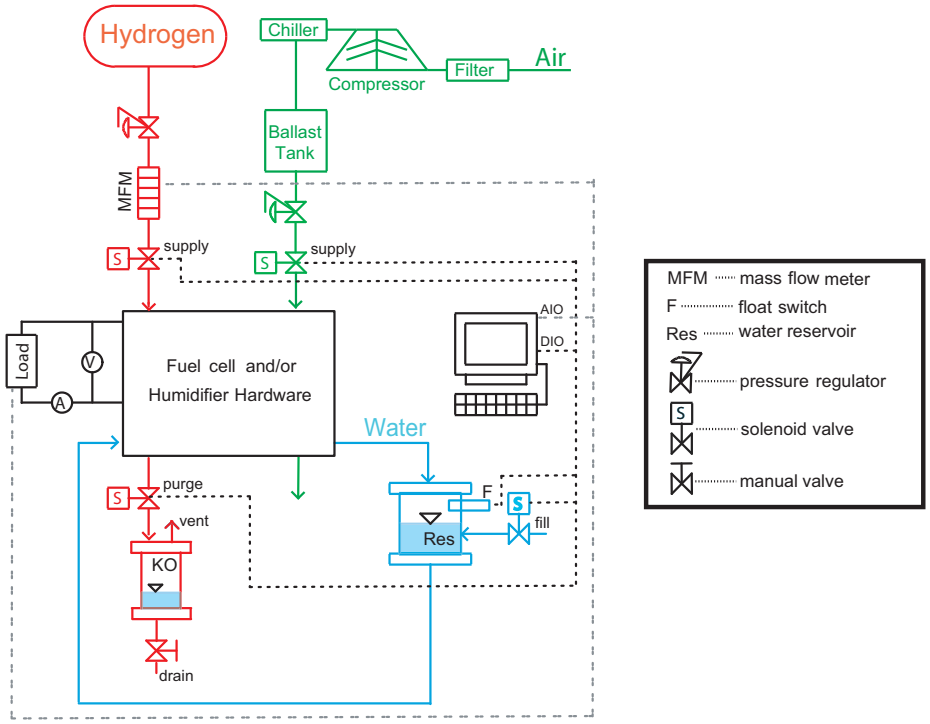

Figure 1.5: Schematic of the test bench hardware, including the computer interface as well as the hydrogen, air and water circulation subsystems.

Series signal conditioning modules, prior to being transmitted to the actuators. The analog input signals, received by the computer through a 16 bit PCI multifunction card, are also conditioned using 5B Series signal conditioning modules with 4Hz filters. While the signal scan rate is approximately 10 Hz, the data file is updated at a rate of 2 Hz. Finally, the digital inputs and outputs are processed

through an Opto-22 digital backplane with optically isolated solid state relays. These relays are used to switch different voltage ranges, including 24VDC and 120VAC.

Pure dry hydrogen is pressure regulated to replenish the hydrogen consumed by the fuel cell in the chemical reaction. The hydrogen stream is dead ended, implying no flow leaving the PEMFC stack, using a purge solenoid valve located downstream of the stack. Hydrogen can be momentarily purged through the fuel cell anode to remove condensed water accumulating in the gas diffusion layers, flow channels and manifolds. Liquid water contained in the hydrogen gas stream is condensed and removed in a knock-out drum before being vented to the atmosphere. The air system utilizes mass flow controllers (MFCs) directing air through the fuel cell or humidifier systems. The combined air-vapor mixture leaving the system is vented to the atmosphere. Deionized water is circulated through the system with the capability of either adding heat using external heat tape, or rejecting heat with fans mounted to a heat exchanger.

1.3 Thesis Overview

This thesis is divided into three main sections detailing the modeling and validation of both the PEMFC stack, in Chapter 2, and the humidification system, in Chapter 3, as well as the humidification system controller development and implementation, in Chapter 4. Concluding remarks are provided in Chapter 5 along with areas of future study. The Appendices contain supplementary materials detailing functional relationships employed, in Appendix A, and a survey of membrane water transport models in Appendix B. For a detailed list of the nomenclature used, refer to the Symbols Section at the front of this thesis.

The experimental hardware used to calibrate and validate the PEMFC model is presented in Section 2.1. Then an overview of the PEMFC model structure is provided in Section 2.2, along with the modeling assumptions in Section 2.4, followed by the detailed description of GDL liquid water capillary transport and gas diffusion in Section 2.5. The spatial discretization employed to solve the partial differential equations is presented in Section 2.6 along with the GDL boundary conditions at the membrane and channel shown in Section 2.7. The voltage output equation which relates the liquid water accumulation in the anode gas channel to voltage performance is given in Section 2.8. The detailed process used to experimentally identify the tunable parameters is provided in Section 2.9. Finally, the experimental calibration and validation results in Sections 2.10 and 2.11 are given along with a parameter sensitivity analysis.

Following the presentation of the PEMFC reactant and water dynamics in Chapter 2, the humidification system modeling effort is presented in Chapter 3. An overview of the humidification system is presented in Section 3.1, providing both a description of the system operation along with hardware used. Next, the model is developed in Section 3.2, including the modeling assumptions, the general two-volume model approach applied for each control volume, followed by the detailed models developed for each volume. A summary of the resulting model is presented in Section 3.3 including the relations between the modeled states and measured outputs. The methodology used

to experimentally identify the unknown heat transfer coefficients is given in Section 3.4 along with the identification results. Finally, the humidification system model validation results are shown in Section 3.5.

Using the validated humidification system model developed in Chapter 3, controllers are designed and implemented in Chapter 4. First, the nonlinear static feedforward map used to regulate air flow is developed in Section 4.1. Then, the reference temperatures used for thermal regulation are selected in Section 4.2. Each plant is then linearized about a set of nominal conditions, as described in Section 4.3. Using these linear approximations, thermostatic controllers are designed in Section 4.4 using both a describing function and simulation based technique and proportional-integral controllers with integral anti-windup are designed in Section 4.5. The controllers are implemented in hardware as described in Section 4.6.

1.4 Contributions

With a given PEMFC design and set of materials, we contribute to the field of dynamic systems and control for active fuel cell performance optimization. Due to the rapid advancement in fuel cell material development, control-oriented modeling efforts should be capable of relating physical material properties to the resulting fuel cell performance as new materials are discovered. Thus, a major contribution of this work was in devising a systematic and reproducible, physics-based, methodology to experimentally identify and validate fuel cell and system dynamics employing standard numerical techniques and off-the-shelf sensors and actuators. These modeling, identification and experimental validation techniques were employed on a fuel cell stack, and external gas humidification system to account for heat and mass transport in these two low temperature membrane based systems under a range of operating conditions. These two systems involve very different modeling assumptions with respect to heat and mass transport, yet employ similar nonlinear optimization techniques for model calibration.

In modeling and validating the fuel cell reactant and water dynamics, and then designing and controlling the gas humidification system for active fuel cell water management, several additional accomplishments were realized. The control-oriented fuel cell modeling effort was advanced by:

- Establishing that a physics-based, one-dimensional (through the GDL), two-phase, isothermal model can be experimentally calibrated to accurately predict the fuel cell output voltage dynamics due to the accumulation of liquid water in the lumped parameter zero-dimensional anode gas channels by relating the occurrence of anode water flooding to fuel cell voltage output. Although other authors have modeled the accumulation of liquid water in the GDL and gas channels, to the best of our knowledge, none had related this accumulation to the dynamic fuel cell voltage response under anode water flooding conditions which occur at low to moderate current densities. The establishment of this relationship allows for an accurate dynamic voltage estimation under a range of operating conditions, which is a necessary step towards further:

  - Investigating observability and controllability as well as ultimately designing feedback

controllers, and
  - Comparing the implications of anode water management strategies, such as exhaust gas recirculation, flow-through with a controllable fuel excess ratio, or dead-ended purge operation, on hydrogen fuel utilization efficiency and system design and control.

The field of fuel cell reactant humidification was advanced by:

- Designing an apparatus to enable independent control of temperature and humidity of reactant gases supplied to the PEMFC stack. Although the concept of using a gas bypass and humidifier to regulate fuel cell reactant humidity is not unique [75], we are unaware of any attempt to regulate both temperature and humidity, which are strongly coupled.
- Developing a simple, physics based model of the gas humidification system. Due to the substantial difference in response times of each of the system volumes, a model of the humidification system was developed for analysis and controller design to achieve thermal tracking while adequately rejecting system disturbances. This was the first low-order model, to our knowledge, of a membrane-based gas humidification system.
- Developing a control strategy for simultaneously achieving thermal and humidity regulation. Previously, only humidity feedback control reliant on a relative humidity sensor had been claimed [75]. In developing this strategy, a critical step was accomplished by properly selecting the controller references used for temperature feedback. Although this may at first seem like a simple step, the selected temperature references have a profound impact on the resulting thermal and humidity regulation. If not properly considered, the system response could be unnecessarily slow or produce an undesireable excursion in humidity.
- Eliminating reliance on a humidity sensor to achieve adequate humidity regulation by first developing an accurate gas relative humidity estimator and then using nonlinear static-feedforward to control gas flow through the humidification system. Due to the notoriously slow response of humidity transducers, especially near saturated conditions, this accomplishment not only advances the field of fuel cell reactant pre-treatment but could also impact other applications reliant on humidity measurements.
- Providing a thorough comparison of the use of on/off versus variable gas heaters in achieving thermal regulation. While desirable for controller simplicity, on/off gas heaters induce temperature limit cycle oscillations. This work provides a clear comparison between these two control strategies to better inform the controller selection process.

Chapter 2

Reactant and Water Dynamics in a PEMFC Stack

This chapter presents a two-phase flow dynamic model that predicts the experimentally observed temporal behavior of a proton exchange membrane fuel cell stack. This model is intended for use in embedded real time control where computational simplicity is of critical importance, thus motivating several simplifying assumptions. A reproducible methodology is presented to experimentally identify six (6) tunable physical parameters based on the estimation of the cell voltage, the water vapor transport through the membrane and the accumulation of liquid water in the gas channels. The model equations allow temporal calculation of the species concentrations across the gas diffusion layers, the water vapor transport across the membrane, and the degree of flooding within the cell structure. The notion of apparent current density then relates this flooding phenomena to cell performance through a reduction in the cell active area as liquid water accumulates. Despite the oversimplification of many complex phenomena, this model provides a useful tool for predicting the temporal variation in cell voltage during electrode flooding conditions. The calibrated model and tuning procedure is demonstrated with a 1.4 kW (24 cell, 300 cm^2) stack, using pressure regulated pure hydrogen supplied to a dead-ended anode, under a range of operating conditions typical for multi-cell stacks.

The model of the reactant and water dynamics is presented in the following sections, first a general overview of the model structure is presented in Section 2.2; followed by a summary of the general modeling assumptions in Section 2.4, then a description of the capillary transport of liquid water and the diffusion of gases within the GDL is provided in Section 2.5; followed by the process used to separate the gas diffusion layer into discrete volumes using standard finite difference techniques to approximate the spatial gradients in Section 2.6; and finally, details of the time varying boundary conditions at the membrane and gas channel interfaces are given in Section 2.7.

2.1 Fuel Cell Experimental Hardware

The fuel cell experimental hardware, designed in collaboration with the Schatz Energy Research Center at Humboldt State University, is installed at the Fuel Cell Control Laboratory at the Univer-

sity of Michigan. A schematic of the major experimental components along with the measurement locations is depicted in Figure 2.1 for the fuel cell hardware components. A description of the test bench operation was provided in Section 1.2 detailing the computer controlled system that coordinates air, hydrogen, cooling, and electrical subsystems.

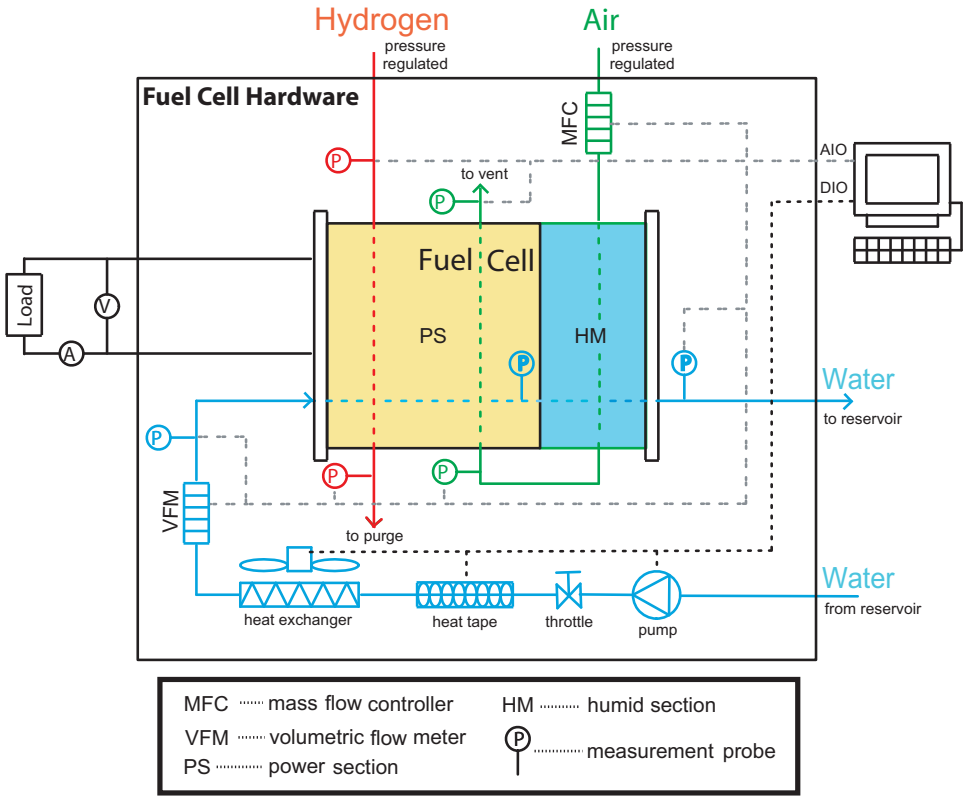

Figure 2.1: Experimental hardware employed and measurement locations. This figure is modified from [57].

Dry pure hydrogen is pressure regulated at the anode inlet to a desired setpoint. This pressure regulation system replenishes the hydrogen consumed in the chemical reaction. For the majority of the operational time, the hydrogen stream is dead-ended with no flow external to the anode. Using a purge solenoid valve, hydrogen is momentarily purged through the anode to remove water and inert gases. Humidified air (generated using a membrane based internal humidifier) is mass flow controlled to a desired stoichiometric ratio. Deionized water is circulated through the system to remove heat produced due to the exothermic chemical reaction. A fan is used to thermostatically control (on-off) the stack outlet coolant to a desired temperature. Measurements of the dry gas mass flow rates supplied to the PEMFC stack are taken along with the temperature, pressure and relative humidity in the inlet and outlet manifolds.

Experimental results are collected from a 24-cell PEMFC stack which can deliver 1.4 kW continuous power, capable of peaking to 2.5 kW. The instrumented PEMFC stack is shown in Figure 2.2. The cell membranes are comprised of GORE^{TM} PRIMEA® Series 5620 membrane electrode assemblies (MEAs). The MEAs utilize 35 μm thick membranes with 0.4 mg/cm^2 and 0.6 mg/cm^2

Pt/C on the anode and cathode, respectively, with a surface area of approximately 300 cm^2. The GDL material, which distributes gas from the flow fields to the active area of the membrane, consists of double-sided, hydrophobic, version 3 ETek^{TM} ELATs® with a thickness of 0.43 mm. The flow fields are comprised of machined graphite plates with gas channels that are approximately 1 mm wide and 1 mm deep. The flow pattern consists of semi-serpentine passages on the cathode (30 channels in parallel that are 16.0 cm in length with two 180^o turns) and straight passages on the anode (90 channels in parallel that are 17.1 cm in length).

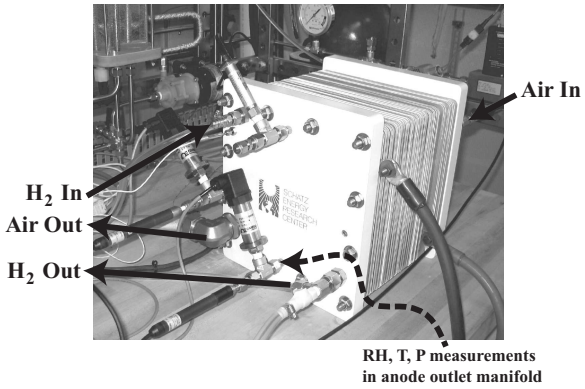

Figure 2.2: Instrumented PEMFC stack installed at the Fuel Cell Control Laboratory, University of Michigan. The arrows indicate the reactant inputs and outputs to and from the stack.

Due to the lack of a practical means to directly measure the accumulation of liquid water within a multi-cell stack, consecutive anode purges and cathode surges (momentarily increasing the gas mass flow rates) were used to indicate the presence of liquid water in either the anode or cathode channels, as shown in Figure 2.3. At approximately 240 seconds the cathode was surged, causing an increase in oxygen partial pressure and cell voltage. However, this momentary voltage increase is not sustained following the surge and the general voltage decay due to flooding in the anode persists. Following an anode purge, the voltage quickly improves and then gradually decays until the next anode purge event is initiated. It is important to note that this gradual decay in cell voltage could be attributed to the accumulation of nitrogen in the anode which would also be expelled during and anode purge event. However, during purge events a significant mass of liquid water can be visually detected leaving the anode. Thus, this work focuses on the impact of anode flooding on cell voltage and assumes nitrogen is not the culprit.

2.2 Fuel Cell Modeling Overview

The anode volume contains a mixture of hydrogen and water vapor, whereas the cathode volume contains a mixture of oxygen, nitrogen, and water vapor. The species concentrations in the channel are calculated based on the conservation of mass assuming the channel is homogeneous, lumped-parameter, and isothermal. Under load, we assume product water is formed in the vapor phase.

This product water vapor, combined with the water vapor supplied with the cathode gas stream,

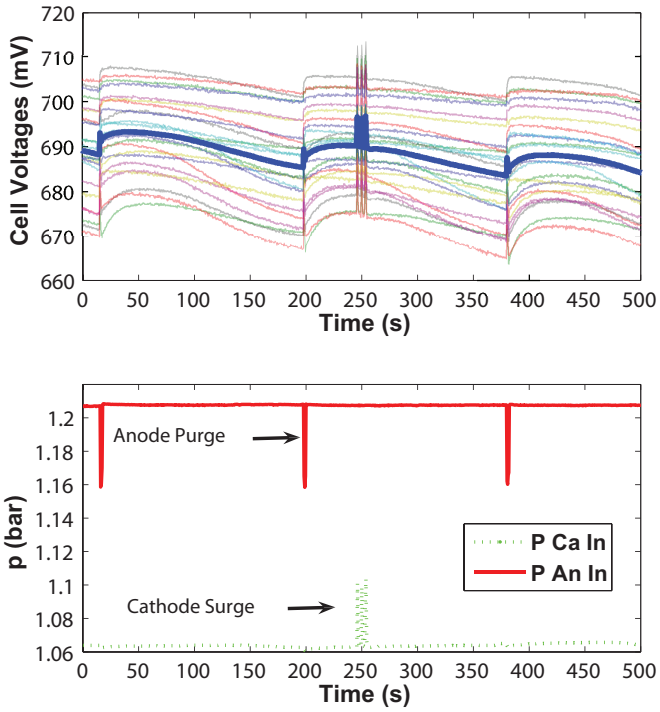

Figure 2.3: Experimental data comparing the impact of anode purging and cathode surging events on cell voltage. These conditions were taken at a constant nominal current density of 0.3 A/cm^2 and an operating temperature of T=65^{o}C. The first subplot shows the 24 individual cell voltages in thin lines along with the average cell voltage with a thick line. The second subplot shows the anode and cathode inlet total absolute pressures.

is exchanged between the anode and the cathode through the hydrophilic membrane. The protons, liberated at the anode, transport water to the cathode through electro-osmotic drag, while back diffusion transfers vapor due to a water vapor concentration gradient across the membrane. The net flux of vapor through the membrane depends on the relative magnitudes of these transport mechanisms. Although there are many efforts to experimentally quantify back diffusion ([65], [19], [42], [76]), conflicting results suggest an empirically data-driven identification of water vapor diffusion might be a practical approach to this elusive subject. Constant parameters have been used to scale back diffusion models for PEMFCs with different membrane materials [56] [26]. Using a similar methodology as [56], in this paper the membrane water transport algorithm employs a tunable parameter to scale the membrane water diffusion model in [19].

When the production or transport of water vapor overcomes the ability of the vapor to diffuse through the GDL to the channel, the vapor supersaturates and condenses. The condensed liquid water accumulates in the GDL until it has surpassed the immobile saturation limit at which point capillary flow will carry the liquid water to an area of lower capillary pressure (the GDL-channel interface). Liquid water in the GDL occupies the pore space, reducing the diffusion of the reactant gases. However, we have found that the reduction of the reactant concentrations due to the changes in the gas diffusivity alone is not significant enough to degrade the voltage by the magnitude exper-

imentally observed. Similar observations lead to the consideration of the reactant diffusion in the catalyst layer [36].

We follow here a different approach and instead of adding the catalyst layer complexity to the model, we consider the effects of flooding on the area available for diffusion. The water (in liquid and vapor phase) that wicks out of the hydrophobic GDL to the channel ultimately obstructs the area that reactants can diffuse through. This effect is not easily modeled because the GDL surface roughness makes it difficult to predict how much GDL surface area is blocked by a given volume of liquid water. For this reason, we assume the liquid water at the GDL-channel interface forms a layer of uniform thickness. This water layer spreads across the surface of the GDL as the volume of liquid water in the channel increases, thus reducing the surface area, which increases the calculated current density, in turn lowering the cell voltage at a fixed total stack current. In this model the thickness of the water layer is an experimentally tuned parameter.

The estimation of the average cell voltage is a function of the reactant concentrations at the surface of the membrane, the membrane water content, temperature, and the calculated current density based on the reduced active area, which in turn is a function of liquid water present in the gas channel. There are four experimentally tunable voltage parameters which are determined using linear least squares for a given set of membrane diffusion and water thickness parameters. By comparing the average measured cell voltage to the model prediction, these parameters can be re-adjusted to match the rate of decay and magnitude of the voltage degradation. This iterative process allows all six tunable parameters to be identified. Figure 2.4 provides an overview of the causal structure of the algorithm used to implement the model.

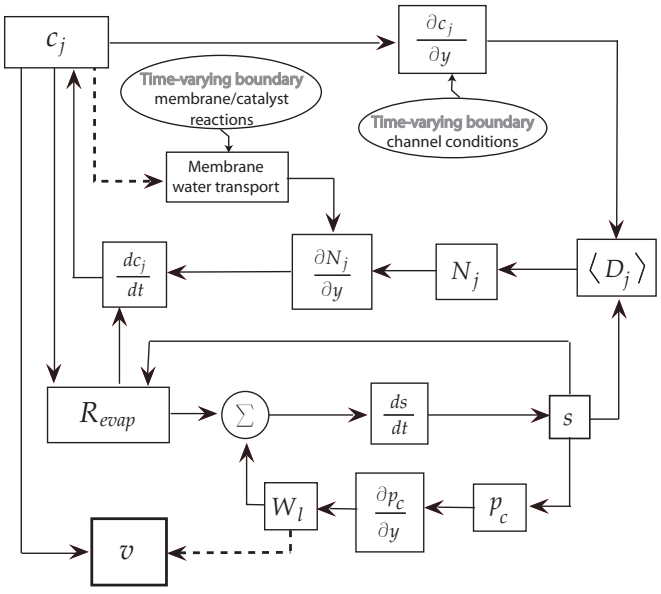

Figure 2.4: Flow chart of GDL model calculation algorithm. The dashed lines indicate the signal flow paths influenced by the tunable parameters.

2.3 Fuel Cell Nomenclature

A list of the model parameters and variable is provided in the front matter, along with values and units. Time derivatives are denoted as $d(\,)/dt$. Spatial derivatives through the GDL thickness in the membrane direction (y) are denoted as $\partial(\,)/\partial y$. In the presented model, all equations have SI units of *Pa*, *N*, *m*, *kg*, *s*, and *J* unless explicitly stated.

The symbol a is used for water activity, c for molar concentration (mol/m^3), $\langle D \rangle$ for effective diffusivity (m^2/s), D_w for water vapor diffusion coefficient (m^2/s), E for the theoretical open circuit voltage (V), i for the nominal current density (A/cm^2), i_{app} for the apparent current density (A/cm^2), i_o for the exchange current density (A/cm^2), I for the total stack current (A), K_{rl} for relative permeability, n_d for electroosmotic drag coefficient (mol H_2O/ mol H^+), N for molar flux (mol/s/m^2), p for pressure (Pa), p^{sat} for the water vapor saturation pressure (Pa), R_{evap} for the evaporation rate (mol/s m^3), s for the fraction of liquid water volume to the total volume, S for the reduced liquid water saturation, T for temperature (K), U_{act} for the activation voltage loss (V), U_{ohmic} for the ohmic voltage loss (V), U_{conc} for the concentration voltage loss (V), $\bar{v}$ for the measured terminal cell voltage (V), $\hat{v}$ for the estimated terminal cell voltage (V), W for mass flow rate (kg/s), x for the mass fraction, and y for the mole ratio. Greek letters are used where ε is for the GDL porosity, λ for membrane water content (mol H_2O/mol SO_3^-), ϕ for relative humidity (0-1), and ω for humidity ratio.

The subscript *amb* is used to represent ambient conditions, *an* for anode, *c* for capillary, *ca* for cathode, *ch* for channel, *ct* for catalyst, *da* for dry air, *dg* for dry gas, *e* for electrode (*an* or *ca*), *fc* for fuel cell stack, H_2 for hydrogen, *in* for the control volume inlet or input, j as an index for gas constituents, k as an index for discretization (in time or space), l for liquid water, *mb* for membrane, N_2 for nitrogen, O_2 for oxygen, *out* for the control volume outlet or output, p for pore, *rm* for return manifold, v for water vapor, and w for water (gas and/or liquid phase).

2.4 General Modeling Assumptions

In summary, the following general assumptions were made in developing the model presented:

A1 The volume of liquid water within the GDL does not restrict the volume occupied by the gases. The authors in [1] indicated that the diffusion of gas through the GDL occurs through a hydrophobic macroporous structure, where as the liquid water travels through the non-wet proofed pores (a microporous structure), implying that the pore volume occupied by gases is fixed. Examining the time scale decomposition of the reactant and water dynamics [39], this assumption primarily influence the liquid water dynamics and due to the relatively small change in liquid water volume between the GDL sections, has a negligible impact. However, if different boundary conditions were applied which significantly modified the spatial distribution of liquid water in the GDL sections, this assumption should be revisited.

A2 The internal cell structure (gas channel, GDL and membrane) is assumed to be isothermal and equal to the time varying coolant outlet temperature. However, the gas inlet temperatures vary and are used to calculate the water vapor mass flow rates entrained with the supplied

reactants. Although it is true that a multi-cell stack with a large active area will undoubtedly have thermal gradients within the cell structure and impact water transport [15], this assumption is adequate for estimating the temporal evolution in cell voltage experimentally observed under both flooding and drying conditions, as will be shown in Section 2.10. Accounting for dynamic thermal states within the gas diffusion layer adds a significant degree of model complexity which, while useful for design, may not be appropriate for control.

A3 The gas channels are treated as homogeneous and lumped parameter. Additionally, flow through the GDL is modeled in one dimension which neglects the difference in transport mechanisms for flow under the ribs versus under the channels. Although models do exist which characterize all these complex phenomena, the inclusion of this additional dimension has a significant impact on the number of internal states in the model.

A4 The only mechanism for removing liquid water from the gas channels is through evaporation. Although this is a common modeling assumption, it could result in an underestimation of the total mass of water (liquid and vapor) removed from the anode during purges. The tuned model parameters may compensate for this underestimation but the identified values were physically reasonable and within ranges reported in literature as discussed in Section 2.9. It has been shown [33] that liquid water droplet instability and the resultant detachment from the GDL to the gas channel can be a significant liquid water removal mechanism at high current density (high gas velocity). Therefore, if this model is to be extended to high current density operation, this assumption should be revisited.

A5 All gases behave ideally. The range of system operating temperatures and pressures permits the assumption of ideal gas behavior for the gas constituents of interest.

A6 Hydrogen, oxygen and nitrogen molecules do not crossover through the membrane. Although these thin polymeric membranes permit the crossover of molecules when there is a concentration gradient across the membrane [31], only the water crossover at steady-state has been considered in this work for the sake of model simplicity.

A7 Due to the relatively small gas flux within the GDL at the current density range considered, the convective transport of gas due to bulk flow was neglected.

2.5 Gas Diffusion Layer Model Details

The diffusion of gas species in the GDL is a function of the concentration gradient, transferring gas from regions of higher concentration to regions of lower concentration. As the GDL pore space fills with liquid water, the capillary pressure increases, causing liquid water to flow to an adjacent pore with less water. The models used to describe the interrelationship between gas transport and liquid water flow are presented in the following subsections.

2.5.1 Liquid Water Capillary Transport

In hydrophobic GDL material, as the GDL pore spaces fill with liquid water, the capillary pressure increases, causing liquid water to flow to adjacent pores with less water. This process creates a flow of liquid water through the GDL, resulting in an injection of liquid into the channel. Applying the conservation of mass to the GDL volume, the liquid water dynamics, which arise from capillary

liquid water mass flow, W_l, and the molar evaporation rate, R_{evap}, can be calculated by

$$\frac{ds}{dt} = \left(\frac{1}{\rho_l \varepsilon A_{fc}}\right) \frac{\partial W_l}{\partial y} - \frac{R_{evap} M_v}{\rho_l} \,, \tag{2.1}$$

where the mass of liquid water in the GDL is expressed in terms of liquid water saturation, s, which represents the fraction of the liquid volume to the pore volume ($s = V_l/V_p$), A_{fc} is the nominal fuel cell active area, ρ_l is the liquid water density, M_v is the molecular weight of water, and ε is the GDL porosity.

The flow of liquid water through the GDL is a function of the capillary pressure gradient [28, 44] described by

$$W_l = -\frac{\varepsilon A_{fc} \rho_l K K_{rl}}{\mu_l} \left(\frac{\partial p_c}{\partial S}\right) \left(\frac{\partial S}{\partial y}\right) \,, \tag{2.2}$$

where p_c is the liquid water capillary pressure, K is the absolute permeability, μ_l is the viscosity of liquid water, and $K_{rl} = S^3$ is the relative permeability of liquid water. The relative permeability function suggests more pathways for capillary flow are available as liquid water saturation increases, and is a function of the reduced liquid water saturation, S, shown by

$$S = \begin{cases} \dfrac{s - s_{im}}{1 - s_{im}} & \text{for} \quad s_{im} < s \leq 1 \\ 0 & \text{for} \quad 0 \leq s \leq s_{im} \end{cases} \,, \tag{2.3}$$

where, s_{im} is the value of the immobile saturation describing the point at which the liquid water path becomes discontinuous and interrupts capillary flow. This capillary flow interruption occurs when $s < s_{im}$. The results of capillary flow experiments using glass beads as porous media show that $s_{im} = 0.1$ [44].

Capillary pressure is the surface tension of the water droplet integrated over the surface area. The Leverett J-function describes the relationship between capillary pressure and the reduced water saturation, S,

$$p_c = \frac{\sigma \cos\theta_c}{\sqrt{K/\varepsilon}} \underbrace{\left[1.417S - 2.120S^2 + 1.263S^3\right]}_{J(S)} \,, \tag{2.4}$$

where σ is the surface tension between water and air, and θ_c is the contact angle of the water droplet [44].

Finally, the molar evaporation rate is

$$R_{evap} = \gamma \frac{p^{sat} - p_v}{RT} \,, \tag{2.5}$$

where γ is the volumetric condensation coefficient [44], R is the ideal gas constant, T is temperature, p_v is the water vapor partial pressure, and p^{sat} is the water vapor saturation pressure which itself is a function of temperature,

$$p^{sat} = 6.853193e-4\, T^4 - 0.74324595\, T^3 + 304.1375\, T^2 - 55613.63\, T + 3831801 \,. \tag{2.6}$$

Data from steam tables in [64] were used to approximate the water vapor saturation pressure relation. When the partial pressure of water vapor is greater than the saturation pressure, R_{evap} is negative, representing the condensation of water. A logical constraint must be included such that if no liquid water is present ($s \leq 0$)) and the saturation pressure is greater than the water vapor pressure, then water can not be evaporated ($R_{evap} = 0$).

2.5.2 Gas Species Diffusion

The diffusion of gas species in the GDL is a function of the concentration gradient, transferring gas from regions of higher concentration to regions of lower concentration. The molar concentration of gas species j is denoted c_j and is a function of the number of moles of gas within the pore volume, V_p, where

$$c_j = \frac{p_j}{RT} \, . \tag{2.7}$$

Diffusion of hydrogen and water vapor occurs in the anode GDL and the diffusion of oxygen and water vapor occurs in the cathode GDL. As a result, both the anode and cathode gas diffusion can be modeled assuming binary diffusion. It is important to note that nitrogen gas is present in the cathode. As a result, the nitrogen concentration in the channel is calculated and assumed to the constant through the GDL since it is not involved in the reduction reaction at the catalyst. Ternary diffusion must be assumed at both the anode and the cathode if nitrogen cross-over were to be considered. The total molar flux is related to the concentration gradient, represented by

$$N_j = -\langle D_j \rangle \frac{\partial c_j}{\partial y} \, , \tag{2.8}$$

where $\langle D_j \rangle$ is the effective diffusivity of the gas constituents in the GDL,

$$\langle D_j \rangle = D_j \varepsilon \left(\frac{\varepsilon - 0.11}{1 - 0.11} \right)^{0.785} (1-s)^2 \, , \tag{2.9}$$

for two dimensional bulk diffusion with flow perpendicular to the GDL carbon fibers, where D_j is the gas diffusion coefficient. Porosity, effective diffusivity and liquid water saturation for carbon Toray® paper GDL, are modeled from [44].

Finally, the general temporal derivative of gas concentration as a function of the local molar flux gradient and the local reaction rate, R_j, of the particular gas species forms a partial differential equation (PDE),

$$\frac{dc_j}{dt} = \frac{\partial N_j}{\partial y} + R_j \, , \tag{2.10}$$

where Equations 2.8-2.10 are combined to yield a second order PDE.

2.6 Discretization of the Spatial Gradients

Each gas diffusion layer is separated into (L=3) discrete volumes, shown in Figure 2.5, to approximate the solution of Equations 2.1 and 2.10 for each of the constituents in the GDL. Spatial discretization of the GDL yields eighteen coupled ordinary differential equations (ODEs), describing the gas constituent concentrations and liquid water saturation, that approximate the solution of the original PDEs.

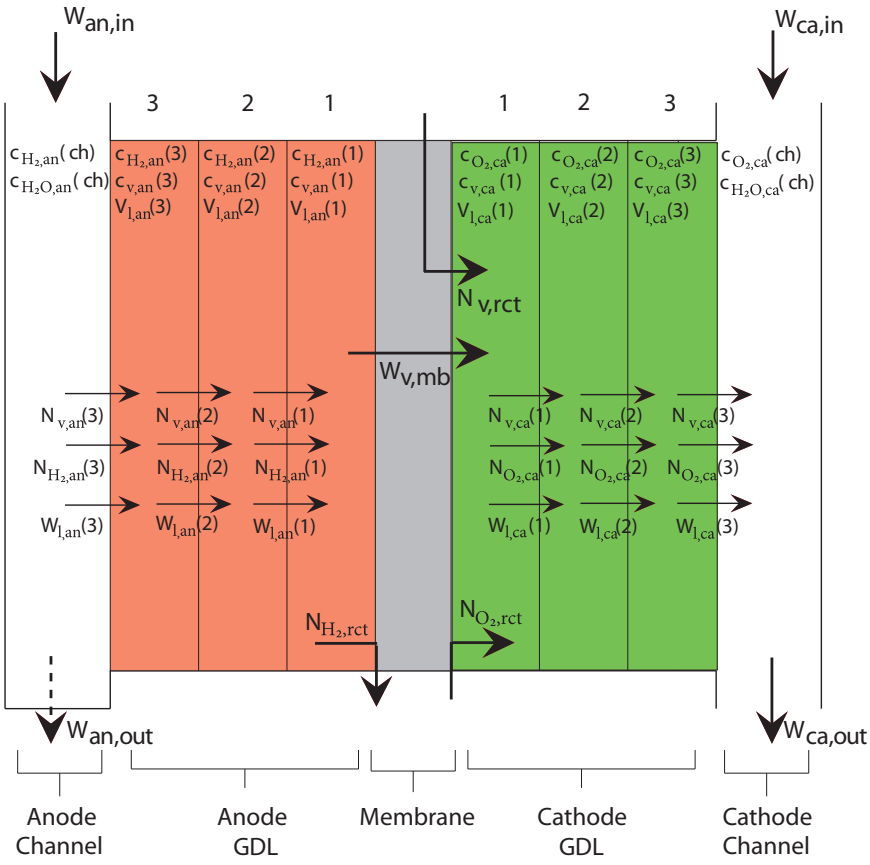

Figure 2.5: Spatial discretization of the gas diffusion layers. The direction of the assumed mass flow rate is indicated with a solid arrow. The dashed arrow is used to indicate periodic mass flow rates.

In the discretized GDL model, spatial gradients are approximated by difference equations. Gas concentration and reduced water saturation gradients are calculated using a forward difference approximation,

$$\frac{\partial \psi_{an}}{\partial y}(k) = \frac{\psi_{an}(k) - \psi_{an}(k+1)}{\delta y}\,, \tag{2.11a}$$

$$\frac{\partial \psi_{ca}}{\partial y}(k) = \frac{\psi_{ca}(k+1) - \psi_{ca}(k)}{\delta y}\,, \tag{2.11b}$$

where $\psi_{an} \in \{c_{H_2,an}, c_{v,an}, S_{an}\}$, and $\psi_{ca} \in \{c_{O_2,ca}, c_{v,ca}, S_{ca}\}$ denote the variables of interest and

$k \in [1, L]$ is the spatial discretization index. Note, the different indices used here for the anode and cathode arise from the numbering system chosen for the discrete GDL layers, shown in Figure 2.5.

The molar flux between GDL sub-volumes is calculated from the gas concentration gradients by applying Equation 2.8 for each gas constituent, shown generally by

$$N_{j,e}(k) = -\langle D_j(k) \rangle \frac{\partial c_{j,e}}{\partial y}(k) \,, \tag{2.12}$$

where the subscript e has been introduced to refer generally to an electrode (either the anode or cathode), and the effective diffusivity is calculated using the liquid water saturation of the k'th section from Equation 2.9. The following backward difference equations are used to calculate the gas molar flux spatial gradients:

$$\frac{\partial N_{j,an}}{\partial y}(k) = \frac{N_{j,an}(k-1) - N_{j,an}(k)}{\delta y} \,, \tag{2.13a}$$

$$\frac{\partial N_{j,ca}}{\partial y}(k) = \frac{N_{j,ca}(k) - N_{j,ca}(k-1)}{\delta y} \,. \tag{2.13b}$$

The temporal ODEs describing the dependence of the gas concentrations on the molar flux gradients in each electrode are,

$$\frac{dc_{j,e}}{dt}(k) = -\frac{\partial N_{j,e}}{\partial y}(k) \,, \quad j \in \{H_2,\, O_2\} \tag{2.14a}$$

$$\frac{dc_{v,e}}{dt}(k) = -\frac{\partial N_{v,e}}{\partial y}(k) + R_{evap,e}(k) \,, \tag{2.14b}$$

where the water evaporation rate, $R_{evap,e}(k)$, is calculated from Equation 2.5 with the water vapor partial pressure, $p_{v,e}$ of the k^{th} section.

The spatial gradient of liquid water flow described in Equation 2.1 is discretized to express the temporal derivative of the liquid water saturation,

$$\frac{ds_{an}}{dt}(k) = \frac{-V_p M_v R_{evap,an}(k) - W_{l,an}(k-1) + W_{l,an}(k)}{V_p \rho_l} \,, \tag{2.15a}$$

$$\frac{ds_{ca}}{dt}(k) = \frac{-V_p M_v R_{evap,ca}(k) + W_{l,ca}(k-1) - W_{l,ca}(k)}{V_p \rho_l} \,, \tag{2.15b}$$

where the mass flow rate of liquid water from Equation 2.2 is a function of the reduced water saturation gradient and the capillary pressure, p_c, written generally for the electrode as

$$W_{l,e}(k) = -\frac{\varepsilon A_{fc} \rho_l K K_{rl,e}(k)}{\mu_l} \frac{\partial p_{c,e}}{\partial S}(k) \frac{\partial S_e}{\partial y}(k) \,, \tag{2.16}$$

where $\frac{\partial p_{c,e}}{\partial S}(k)$ is calculated analytically from Equation 2.4.

2.7 Boundary Conditions

The membrane and gas channels serve as time-varying boundary conditions for the GDL model. This section presents the application of mass conservation in the channel as well as the model for the water vapor exchange between the anode and cathode through the membrane. It is important to remember that the spatial gradients within the GDL are approximated with finite difference equations. A variable taken from a GDL section that is adjacent to the boundary of interest will be denoted by $\psi(1)$ or $\psi(L)$, where $(L = 3)$ indicates the section next to the gas channel and (1) indicates the section next to the membrane.

2.7.1 Membrane Boundary Conditions

The reaction at the catalyst surface of the membrane results in a loss of hydrogen and oxygen at the anode and cathode, respectively. These fluxes, $N_{j,e}(0)$, are used in the calculation of the molar flux spatial gradients, described by

$$N_{j,e}(0) = \frac{I}{\varepsilon A_{fc} 2\xi F} \text{ with } \begin{cases} \xi = 1 & \text{for } j = H_2 \\ \xi = 2 & \text{for } j = O_2 \ , \end{cases} \tag{2.17}$$

where I is the total current drawn from the stack and F is the Faraday constant. The molar flux of water vapor at the GDL-membrane boundary, $N_{v,e}(0)$, is influenced by the generation of water vapor at the cathode membrane surface as well as the flow of water vapor through the membrane,

$$N_{v,an}(0) = \frac{1}{\varepsilon} N_{v,mb} \ , \tag{2.18a}$$

$$N_{v,ca}(0) = \frac{1}{\varepsilon} \left(\frac{I}{2FA_{fc}} + N_{v,mb} \right) \ . \tag{2.18b}$$

Note, a scaling factor of $1/\varepsilon$ is used here to ensure that the water vapor mass flow rate through the membrane is equal to the mass flow rate entering the GDL at the membrane boundary.

The water content of the membrane influences the membrane vapor transport which establishes a time-varying boundary condition for both the anode and the cathode. These membrane properties, described in [65], are assumed to be invariant across the membrane surface. The spatial variation of water vapor throughout the membrane is neglected due to the significant difference in thickness between the GDL (432 μm) and the membrane (35 μm). It is important to note that the membrane transport properties presented in this section are taken from experimental work conducted at steady-state. Non steady-state phenomena, such as membrane swelling and hysteresis, could be added in the future to improve model fidelity.

As with the other volumes, the membrane is considered to be homogeneous and lumped parameter. The flux of water vapor through the membrane, $N_{v,mb}$, accounts for the effects of both

back-diffusion and electro-osmotic drag, suggested by [65],

$$N_{v,mb} = n_d \frac{i}{F} - \alpha_w D_w \frac{(c_{v,ca,mb} - c_{v,an,mb})}{t_{mb}}, \tag{2.19}$$

where i is the nominal fuel cell current density (I/A_{fc}), n_d is the electro-osmotic drag coefficient, D_w is the membrane water vapor diffusion coefficient, and t_{mb} is the membrane thickness. The parameter α_w is a tunable parameter that will be identified using experimental data. The convective water transport mechanisms suggested in [15, 77, 12] are neglected due to the relatively small water pressure gradients at these operating conditions. For a detailed review of published literature on membrane water vapor transport models refer to Appendix B.

The electro-osmotic drag coefficient, described by [65], is calculated using:

$$n_d = \frac{2.5\lambda_{mb}}{22} \quad . \tag{2.20}$$

where the membrane water content, λ_{mb} is defined as the ratio of water molecules to the number of charge sites.

The water vapor concentration in the electrode at the membrane surface is

$$c_{v,e,mb} = \frac{\rho_{mb,dry}}{M_{mb,dry}} \lambda_e \ , \tag{2.21}$$

where $\rho_{mb,dry}$ is the membrane dry density, $M_{mb,dry}$ is the membrane dry equivalent weight, and λ_e is the membrane water content at the surface of the membrane next to either the anode or cathode GDL.

The water vapor diffusion coefficient for a perflourinated ionomeric membrane, Nafion® 117, was determined at 25^{o}C by [19] by applying a mass balance to determine the water vapor flux through the membrane, resulting in

$$D_w = 3.5 \times 10^{-6} \left(\frac{\lambda_{mb}}{14} \right) exp \left[\frac{-2436}{T} \right]. \tag{2.22}$$

Two different cubic polynomials were presented by [65] and [24] to relate water activity to membrane water content at 30^{O}C and 80^{o}C, shown as

$$\lambda_j^{30^oC} = 0.043 + 17.81 a_j - 39.85 a_j^2 + 36.0 a_j^3 \ , \tag{2.23a}$$

$$\lambda_j^{80^oC} = 0.300 + 10.8 a_j - 16.0 a_j^2 + 14.1 a_j^3 \ , \tag{2.23b}$$

where a is the water activity and the subscript j is used here to distinguish between the anode or cathode membrane surface and within the membrane itself, $j \in \{an,\ ca,\ mb\}$. To estimate the water content at intermediate temperatures and sub-saturated conditions, [13] suggested a linear

interpolation between the two uptake isotherms shown in Equation 2.23, such that

$$\lambda_j = \left(\lambda_j^{80^oC} - \lambda_j^{30^oC}\right)\left(\frac{T-303}{353-303}\right) + \lambda_j^{30^oC} \quad . \tag{2.24}$$

It is important to note that these two uptake isotherms are applicable only when water is in the vapor phase ($a_j \leq 1$).

In [65] it was shown that a membrane equilibrated with liquid water has a water content of λ=16.8 at 80^{o}C, which differs from the water content when the membrane is equilibrated with a saturated vapor. It was further indicated that the water content is sensitive to temperature when equilibrated with liquid water, but assumed to be a linear relationship between [λ=14,a=1] and [λ=16.8,a=3] regardless of temperature, due to a lack of data regarding the membrane equilibration for water in both the liquid and vapor phase. Similarly, we assume a linear relationship between the membrane water content when equilibrated with water vapor, shown in Equation 2.24 for a_j=1, and the value of $\lambda = 16.8$ at a=3 published by [65], such that

$$\lambda_j = \left(\frac{16.8 - \lambda_j^{a=1}}{3-1}\right)(a_j - 1) + \lambda_j^{a=1} \tag{2.25}$$

for $1 < a_j < 3$. Further experimental results from [81] and [24] provided data regarding the temperature sensitivity of the membrane water content equilibrated with liquid water. However, fitting this data points to a non-monotonic behavior of λ=f(a), at some temperatures within the operating range of the PEMFC, during the transition between water in the vapor and liquid phases ($a = 1$), hence this relationship is not considered in this work.

Finally, the membrane water activity is assumed to be the average between the anode and cathode water activities (defined by the GDL sections closest to the membrane surface), described by

$$a_{mb} = \frac{a_{an}(1) + a_{ca}(1)}{2} \text{ and } a_e(1) = \frac{p_{v,e}(1)}{p^{sat}}, \tag{2.26}$$

where $p_{v,e}(1)$ is the water vapor pressure in the GDL layer next to the membrane, calculated using the water vapor concentrations.

Note: it is assumed that reactant molecules do not transfer through the membrane between the anode and the cathode. Additionally, only water vapor can penetrate the membrane, not liquid water, implying $W_{l,e}(0) = 0$.

The calculation algorithm for the membrane boundary condition used to relate these GDL water vapor partial pressures to the membrane vapor flux is shown in Figure 2.6. In summary, the water vapor partial pressures in the GDL section closest to the membrane surfaces are used to determine the water activity in the first GDL section, which is assumed to be equal to the membrane water activity at the membrane-GDL interface. These two membrane water activities are averaged to calculate the lumped membrane water activity, which influence diffusion and electro-osmotic drag. Finally, the net water vapor flux is calculated, given diffusion, drag and the water vapor concentrations at the

membrane surfaces.

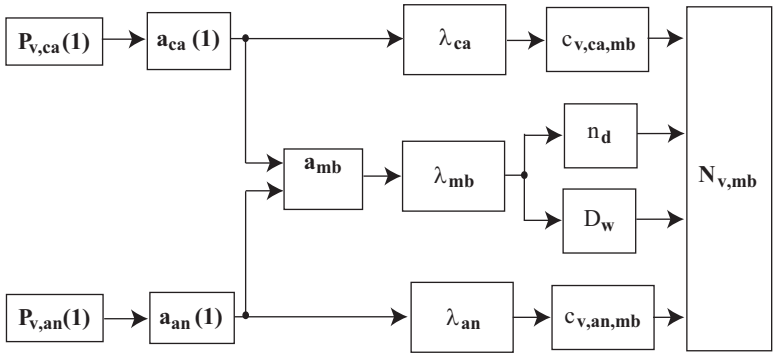

Figure 2.6: Summary of the calculation procedure to determine the membrane water vapor flux given GDL section (1) water vapor partial pressures.

2.7.2 Boundary conditions at the cathode channel

The concentration of oxygen and water vapor in the cathode channels, $c_{O_2,ca}(L+1)$ and $c_{v,ca}(L+1)$, are used for the calculation of the gas concentration gradient for the GDL section next to the channels, $\frac{\partial c_{j,ca}}{\partial y}(L)$. Mass conservation for the gas species in the cathode is applied using the cathode inlet conditions as inputs, requiring measurements of the dry air mass flow rate, $W_{da,ca,in}$, temperature, $T_{ca,in}$, total gas pressure, $p_{ca,in}$, and humidity, $\phi_{ca,in}$, along with the cathode outlet pressure, $p_{ca,out}$. After completing several experiments under a range mass flow rates and temperatures, it was found that the cathode inlet total gas flow was fully humidified and the cathode outlet total pressure was approximately atmospheric, motivating the assumptions that $\phi_{ca,in}$=1 and $p_{ca,out}$=p_{atm}.

The mass flow rate of the individual gas species supplied to the cathode channel are calculated as follows:

$$\begin{aligned} W_{O_2,ca,in} &= x_{O_2,ca,in} W_{da,ca,in}, \\ W_{N_2,ca,in} &= x_{N_2,ca,in} W_{da,ca,in}, \\ W_{v,ca,in} &= \omega_{ca,in} W_{da,ca,in}, \end{aligned} \tag{2.27}$$

where the humidity ratio, ω, is generally defined by

$$\omega = \frac{M_v}{M_{dg}} \frac{\phi\, p^{sat}}{p - \phi\, p^{sat}} , \tag{2.28}$$

for a gas-water vapor mixture, with the mass fraction of oxygen and nitrogen in the dry air (da) defined as $x_{O_2} = y_{O_2} M_{O_2}/M_{da}$ and $x_{N_2} = (1-y_{O_2}) M_{N_2}/M_{da}$, where $M_{da} = y_{O_2} M_{O_2} + (1-y_{O_2}) M_{N_2}$ and y_{O_2} is the oxygen mole fraction in dry air.

The gas species mass in the cathode channel are balanced by applying mass continuity:

$$\begin{aligned} \frac{dm_{O_2,ca}(L+1)}{dt} &= W_{O_2,ca,in} - W_{O_2,ca,out} + W_{O_2,ca}(L), \\ \frac{dm_{N_2,ca}(L+1)}{dt} &= W_{N_2,ca,in} - W_{N_2,ca,out}, \\ \frac{dm_{w,ca}(L+1)}{dt} &= W_{v,ca,in} - W_{v,ca,out} + W_{w,ca}(L). \end{aligned} \tag{2.29}$$

The cathode channel pressure is calculated applying Dalton's law such that

$$p_{ca}(L+1) = \underbrace{\frac{RT}{V_{ca}}\left(\frac{m_{O_2,ca}(L+1)}{M_{O_2}} + \frac{m_{N_2,ca}(L+1)}{M_{N_2}}\right)}_{p_{dg,ca}(L+1)} + \underbrace{\min\left[p^{sat}, \frac{RTm_{w,ca}(L+1)}{M_v V_{ca}}\right]}_{p_{v,ca}(L+1)}. \tag{2.30}$$

Although in the physical system the cathode air mass flow rate may be responsible for removing some liquid water from the cathode channel, for modeling purposes it is assumed that all water exiting the cathode is in the form of vapor.

The mass flow rate of gases exiting the cathode are calculated as:

$$\begin{aligned} W_{ca,out} &= k_{ca}(p_{ca}(L+1) - p_{ca,out}), \\ W_{da,ca,out} &= \tfrac{1}{1+\omega_{ca,out}} W_{ca,out}, \\ W_{O_2,ca,out} &= x_{O_2,ca,ch} W_{da,ca,out}, \\ W_{v,ca,out} &= W_{ca,out} - W_{a,ca,out}, \\ W_{N_2,ca,out} &= (1 - x_{O_2,ca}) W_{da,ca,out}, \end{aligned} \tag{2.31}$$

where k_{ca} is an orifice constant found experimentally. For a detailed description of the process used to identify the orifice constants with experimental data, refer to Appendix A. Although the mole fraction of oxygen at the cathode inlet is assumed to be constant, $y_{O_2,ca,in} = 0.21$, the mole fraction of oxygen in the channel (driving the outlet mass flow rates) is dependent upon the oxygen mass (pressure) state in the channel, such that $y_{O_2,ca} = p_{O_2,ca}/p_{ca}$.

Finally, the oxygen and total water mass flow rates between the GDL and the channel, $W_{O_2,ca}(L)$ and $W_{w,ca}(L)$, must be calculated to solve the mass conservation equations shown in Equation 2.29. The oxygen mass flow through the GDL-channel interface is a function of the oxygen molar flux, $N_{O_2}(L)$. The total water mass flow rate, $W_{w,ca}(L)$, exchanged between the GDL and channel is a function of the liquid water mass flow, $W_{l,ca}(L)$, and the water vapor flux, $N_{v,ca}$. Both the oxygen and total water mass flow rates are described by

$$\begin{aligned} W_{O_2,ca}(L) &= N_{O_2}(L) M_{O_2} \varepsilon A_{fc} n_{cells}, \\ W_{w,ca}(L) &= (W_{l,ca}(L) + N_{v,ca}(L) M_v \varepsilon A_{fc})\, n_{cells}\ , \end{aligned} \tag{2.32}$$

where the assumption $S_{ca}(L+1) = 0$ is employed in the calculation of the reduced water saturation gradient to determine the liquid water mass flow rate between the GDL-channel interface, $W_{l,ca}(L)$. Within the channel, the volume of liquid water is assumed to be negligible compared with the total channel volume, motivating this assumption that $S_{ca}(L+1)$ =0.

2.7.3 Boundary conditions at the anode channel

Similarly to the cathode, the inputs for the anode calculations are the measured anode inlet conditions including the dry hydrogen mass flow rate, $W_{H_2,an,in}$, the supply manifold temperature, $T_{an,in}$,

the total pressure, $p_{an,in}$, and the relative humidity, $\phi_{an,in}$. Dry hydrogen is supplied to the anode, as a result $\phi_{an,in}$= 0. The resulting mass balances for hydrogen and water are:

$$\begin{array}{ll} \frac{dm_{H_2,an}(L+1)}{dt} & = W_{H_2,an,in} - W_{H_2,an,out} - W_{H_2,an}(L), \\ \frac{dm_{w,an}(L+1)}{dt} & = W_{v,an,in} - W_{v,an,out} - W_{w,an}(L). \end{array} \tag{2.33}$$

The dry hydrogen inlet mass flow rate, $W_{H_2,an,in} = k_{an,in}(p_{an,in} - p_{an}(L+1))$, is controlled with a pressure regulator to maintain a constant anode inlet total pressure. The process used to determine the anode orifice constants is provided in Appendix A. Because the hydrogen supplied to the anode is dry, the vapor mass flow rate is assumed to be zero ($W_{v,an,in}$= 0). In calculating the anode total channel pressure, both the partial pressures of hydrogen and water vapor must be estimated such that,

$$p_{an}(L+1) = \underbrace{\frac{RT}{M_{H_2}V_{an}} m_{H_2}(L+1)}_{p_{H_2,an}(L+1)} + \underbrace{\min\left[p^{sat}, \frac{RT\,m_{w,an}(L+1)}{M_v V_{an}}\right]}_{p_{v,an}(L+1)}. \tag{2.34}$$

The total mass flow rate leaving the anode channel, $W_{an,out}$, exists only during an anode gas purge to remove both water, and unfortunately, hydrogen. The equations quantifying the hydrogen and water vapor mass flow rates leaving the anode channel are expressed as:

$$\begin{array}{ll} W_{an,out} & = k_{an,out}(p_{an}(L+1) - p_{an,out}), \\ W_{H_2,an,out} & = \frac{1}{1+\omega_{an,out}} W_{an,out}, \\ W_{v,an,out} & = W_{an,out} - W_{H_2,an,out}. \end{array} \tag{2.35}$$

Similarly to the cathode, the gas and liquid water mass flow rates between the GDL and channel are calculated by

$$\begin{array}{ll} W_{H_2,an}(L) & = N_{H_2}(L) M_{H_2} \varepsilon A_{fc} n_{cells}, \\ W_{w,an}(L) & = \left(W_{l,an}(L) + N_{v,an}(L) M_v \varepsilon A_{fc}\right) n_{cells}, \end{array} \tag{2.36}$$

where the assumption $S_{an}(L+1) = 0$ is employed in the calculation of the reduced water saturation gradient to determine the liquid water mass flow rate between the GDL-channel interface, $W_{l,an}(L)$.

The calculation of the mass flow rates leaving the anode channel depends on the measurement of the anode outlet total pressure, $p_{an,out}$, shown in Equation 2.35. The anode outlet pressure can also be estimated using a similar approach as presented for the anode channel and documented in [52], where $W_{an,rm} = k_{an,rm}(p_{an,out} - p_{amb})$, resulting in the addition of two states (hydrogen and water mass in the return manifold).

2.8 Output Voltage Equation

In this section, the voltage equation is presented as a mapping from the apparent current density, reactant concentrations, temperature and membrane humidity conditions. All units for current den-

sity used throughout the presentation of the voltage model are given in A/cm^2 for consistency with other published models.

Once anode flooding occurs, we associate the resulting voltage degradation with the accumulation of liquid water mass in the anode channel,

$$m_{l,an}(L+1) = max\left[0, m_{w,an}(L+1) - \frac{p^{sat} M_v V_{an}}{RT}\right], \tag{2.37}$$

where the mass of water in the anode channel, $m_{w,an}(L+1)$, is taken from Equation 2.33. The accumulated liquid water mass is assumed to form a thin film of thickness, t_{wl}, blocking part of the active fuel cell area, A_{fc}, and consequently increasing the apparent current density [40],

$$i_{app}\left(\frac{A}{cm^2}\right) = \frac{I(A)}{10000 A_{app}(m^2)}, \tag{2.38}$$

where the apparent fuel cell area A_{app} is approximated as

$$A_{app} = A_{fc} - \frac{2\, m_{l,an}(L+1)}{n_{cells}\, \rho_l\, t_{wl}}. \tag{2.39}$$

The scaling factor of 2 in Equation 2.39 was used to account for the fact that one half of the surface area at the GDL-channel interface is occupied by channel ribs, which reduces the area available for the formation of a liquid water film. This methodology for relating the accumulation of the liquid water in the channel to a restricted active area was first proposed in [40] and a similar methodology was employed by [22]. Some models that deal with cathode flooding, however, propose an increased current density due to the water accumulation in the catalyst layer at the GDL-membrane interface [74]. Ongoing experimental work from many researchers has focused on quantifying this accumulation of liquid water using direct visualization [37] or neutron imaging techniques [70, 10, 32].

The thickness of this water layer, t_{wl} is a tunable parameter that impacts the rate at which the active area is reduced and in turn the rate of voltage decay as the liquid water accumulates. Note that the notion of apparent current density, influenced by t_{wl} in the gas channel, is a simplification of the flooding phenomena that nevertheless captures the experimentally observed dynamic voltage behavior of a multi-cell stack under a range of conditions including both flooding and non-flooding. As shown in Section 2.9, this tuned parameter is similar to that experimentally determined in [10].

Once the apparent current density is calculated it is used, together with the partial pressure of the reactants in the anode and cathode GDL sections next to the membrane, to determine the average cell voltage. The average cell voltage, v, is equal to the theoretical open circuit voltage, E, minus the activation, U_{act}, and ohmic, U_{ohmic}, losses such that

$$v = E - U_{act} - U_{ohmic}\ . \tag{2.40}$$

We have assumed that the concentration voltage loss due to a mass transport limitation at high current density is negligible as a result of our operation at relatively low current densities ($i < 0.4$

A/cm^2).

The theoretical open circuit voltage, if the chemical reaction was a reversible process, varies with respect to reactant partial pressures and temperature according to the change in Gibbs free energy and the Nernst Equation [48],

$$E = -\left(\frac{\Delta H}{2F} - \frac{T\Delta S}{2F}\right) + \frac{RT}{2F}\ln\left(\frac{p_{H_2,an}(1)\sqrt{p_{O_2,ca}(1)}}{(p_o)^{1.5}}\right), \tag{2.41}$$

where ΔS and ΔH are the differences in entropy and enthalpy from standard state conditions, p_o is the standard pressure, and the oxygen and hydrogen partial pressures, $p_{O_2,ca}(1)$ and $p_{H_2,an}(1)$, are located in GDL Section 1 next to the membrane.

The activation overvoltage accounts for the energy required to drive the chemical reaction (a deviation from equilibrium), as well as the loss current density resulting from the transport of molecular hydrogen from the anode to the cathode through the membrane. The total activation voltage loss was parameterized according to [3], such that

$$U_{act} = K_1\frac{RT}{F}\ln\left(\frac{i_{app}+i_{loss}}{i_o}\right), \tag{2.42}$$

where K_1 is a tunable parameter representing the reciprocal of the charge transfer coefficient, i_{loss} is the loss current density due to hydrogen crossover, i_{app} is the apparent current density that is a function of the reduced active area due to the accumulation of liquid water at the GDL-channel interface from Equation 2.38, and i_o is the exchange current density which is a function of the reactant partial pressure and temperature [3], expressed as:

$$i_0 = K_2\left(\frac{p_{O_2,ca}(1)}{p_o}\right)^{K_3}\exp\left[-\frac{E_c}{RT}\left(1-\frac{T}{T_o}\right)\right], \tag{2.43}$$

where K_2 and K_3 are tunable parameters, E_c is the activation energy for oxygen reduction on Pt, and T_o is the reference temperature.

The ohmic voltage loss is dominated by the membrane conductivity as well as the contact and bulk electrical resistance of the conductive materials. This loss was shown experimentally in [65] to have the following functional form,

$$U_{ohmic} = K_4\left[\frac{t_{mb}}{(b_{11}\lambda_{mb}-b_{12})}e^{-1268\left(\frac{1}{303}-\frac{1}{T}\right)}\right]i_{app}, \tag{2.44}$$

where K_4 is a tunable parameter, t_{mb} is the membrane thickness, b_{11} and b_{12} are experimentally identified parameters from [65], and λ_{mb} is the membrane water content from Equations 2.23-2.25.

2.9 Parameter Identification Approach

Lacking a practical experimental means to measure the spatial distribution of water mass in the anode and cathode of a large multi-cell stack for the use of online control, the lumped-parameter two-phase flow model developed here is indirectly calibrated and validated through model prediction of the effects of flooding on cell voltage. A reasonably wide variation in the experimental operating conditions have been examined, including both flooding and non-flooding conditions, to ensure that the model adequately estimates the relationship between GDL flooding and cell voltage degradation. The range of operating conditions examined is limited due to our operation with a stack, not a single cell, and our desire to minimize cell to cell voltage variations [57].

There exists two sets of model parameters which must be either calibrated or tuned. The calibrated parameters are based on the fuel cell hardware specifications, listed in Table 2.1. These parameters may require additional experiments to determine, such as the orifice constants describing the back pressure flow characteristics for each gas channel. For a detailed description of the process used to tune the orifice constants refer to Appendix A. The known parameter values taken from published literature, are listed in Table 2.2.

Table 2.1: Parameters required based on PEMFC stack specifications.

Symbol	**Definition**
A_{fc}=0.030 m^2	fuel cell nominal active area
K=2.55e-13 m^2 [44]	absolute permeability
$M_{mb,dry}$=1.0 kg/mol	membrane dry equivalent weight
n_{cells}=24	number of cells in stack
t_{gdl}=0.5 mm	total GDL thickness
t_{mb}=0.038 mm	PEMFC membrane thickness (includes catalyst layer)
V_{ca}=380 cm^3	cathode channel volume
V_{an}=430 cm^3	anode channel volume
$V_{an,rm}$=345 cm^3	anode return manifold volume
ε=0.5 [44]	GDL material porosity
$\rho_{mb,dry}$=1900 kg/m^3	membrane dry density
$k_{ca,in}$=11.3e-7 m s	cathode orifice constant
$k_{ca,out}$=11.3e-7 m s	cathode orifice constant
$k_{an,in}$=9.34e-7 m s	anode orifice constant
$k_{an,out}$=9.34e-7 m s	anode orifice constant
$k_{an,rm}$=11.3e-6 m s	return manifold orifice constant

The two water related tunable parameters that require experimental identification are the: scaled "stack-level" membrane back diffusion, α_w, of Equation 2.19, and thickness of liquid water layer accumulating at the GDL-channel interface, t_{wl}, of Equation 2.39. Additionally, there are four tunable parameters K_1-K_4 associated with the output voltage in Equations 2.40-2.44. Although the water related parameters do not appear linearly, the voltage equation can be rearranged such that

Table 2.2: PEMFC modeling parameters found from published literature.

Symbol	Definition
b_{11}=0.005139 $(\frac{molSO_3^-}{molH_2O})(\Omega cm)^{-1}$ [65]	membrane conductivity parameter
b_{12}=0.00326 $(\Omega cm)^{-1}$[65]	ohmic resistance parameter
D_{H_2}=114 mm^2/s [44]	hydrogen diffusion coefficient
D_{O_2}=30.3 mm^2/s [44]	oxygen diffusion coefficient
E_c=66 kJ/mol [3]	activation energy
F=96485 C/mol e$^-$	Faraday's constant
ΔH=-228,740 J/mol	Enthalpy difference from STP (water in vapor phase)
i_{loss}=1 mA/cm^2 [3]	loss current density
L=3	number of GDL sections
M_{H_2}=0.002 kg/mole	hydrogen molecular weight
M_{O_2}=0.032 kg/mole	oxygen molecular weight
M_{N_2}=0.028 kg/mole	nitrogen molecular weight
M_{H_2O}=0.018 kg/mole	water molecular weight
p_o=1 atm	standard state pressure
R=8.314 J/mol K	universal gas constant
s_{im}=0.1 [44]	immobile saturation
ΔS=-44.43 J/mol K	Entropy difference from STP (water in vapor phase)
T_o=298.15 K	standard state temperature
V_p=2.5 cm^3	GDL section pore volume
δy=0.167 mm	GDL discretization width
γ=900 s^{-1} [44]	volumetric condensation coeff.
θ_c=60 degrees [44]	contact angle
μ=0.405 g/m s [44]	liquid water viscosity
ρ=997 kg/m^3	liquid water density
σ=0.0644 N/m [44]	surface tension

each of the tunable K's is linear in the coefficient,

$$\begin{aligned}\hat{v} =& E - K_1\frac{R\,T}{F}\left(\ln\left(i_{app}+i_{loss}\right)+\frac{E_c}{R}\left(\frac{1}{T}-\frac{1}{T_0}\right)\right)+\ln\left(K_2\right)K_1\frac{R\,T}{F}+K_3\,K_1\frac{R\,T}{F}\,\ln\left(\frac{p_{O_2,ca}(1)}{p_0}\right)\\ &-K_4\left[\frac{t_{mb}}{\left(b_{11}\lambda_{mb}-b_{12}\right)}e^{-1268\left(\frac{1}{303}-\frac{1}{T}\right)}\right]\left(i_{app}+i_{loss}\right)\,. \end{aligned} \tag{2.45}$$

The relationship of the voltage model to the GDL model and boundary conditions is shown in the block diagram of Figure 2.7. The resulting cell voltage output is first compared to the measured value for parameter tuning and then for model validation.

Given a set of values for α_w and t_{wl}, the voltage parameters were identified using linear least squares to minimize the difference between the measured average cell voltage, $\overline{v}$, and the modeled cell voltage, $\hat{v}$, using the cost function

$$J=\int^{t_{exp}}\left[\overline{v}(\tau)-\hat{v}(\tau)\right]^T\left[\overline{v}(\tau)-\hat{v}(\tau)\right]d\tau\,, \tag{2.46}$$

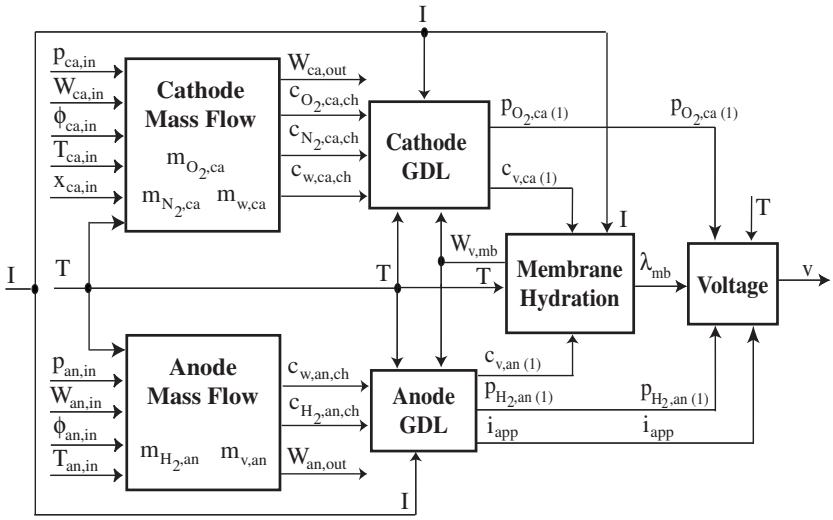

Figure 2.7: Block diagram indicating the inputs and outputs from the GDL and voltage models. The dashed rectangle encompasses the GDL model.

over the experimental testing time, t_{exp}. The statistics associated with the estimation error were examined over a range of $[\alpha_w, t_{wl}]$ pairs to find the locally optimal $[\alpha_w, t_{wl}]$ combination and the resulting K values.

In the physical stack hardware, there are 24 individual cell voltages being measured. The average and median cell voltages exhibit similar dynamics with a relatively small difference in voltage between them. However, there is a significant difference in the magnitude and deviation between the minimum and maximum cell voltages. As a result, the use of either the minimum or maximum cell voltages for parameter tuning results in an underestimation or overestimation of the degree of flooding. For these reasons, the average cell voltage is used for model tuning.

2.10 Model Calibration Results

Experimental calibration data were collected for a range of nominal stack current densities from i=0-300 mA/cm^2, air stoichiometries of 250% and 300%, and coolant outlet temperatures from 45-63^{o}C, at an anode inlet total pressure of 1.2 bar, as shown in Figure 2.8. A polarization curve (I-V) was conducted at approximately 70 minutes, at which time the purge events were temporarily disabled. The purge events were scheduled to occur every 180 seconds for a duration of 1 second. During purge events, the purge solenoid valve was momentarily opened, exposing the anode outlet manifold to ambient pressure. As a result of this decreased anode total pressure, the manual pressure regulator, which tries to maintain its downstream pressure, increased the hydrogen mass flow rate through the system. Following the closure of the purge solenoid valve, small spikes in pressure occur as the pressure regulator readjusted its delivery pressure.

As shown in Figure 2.8, the initial coolant outlet temperature setpoint was 50^{o}C and then

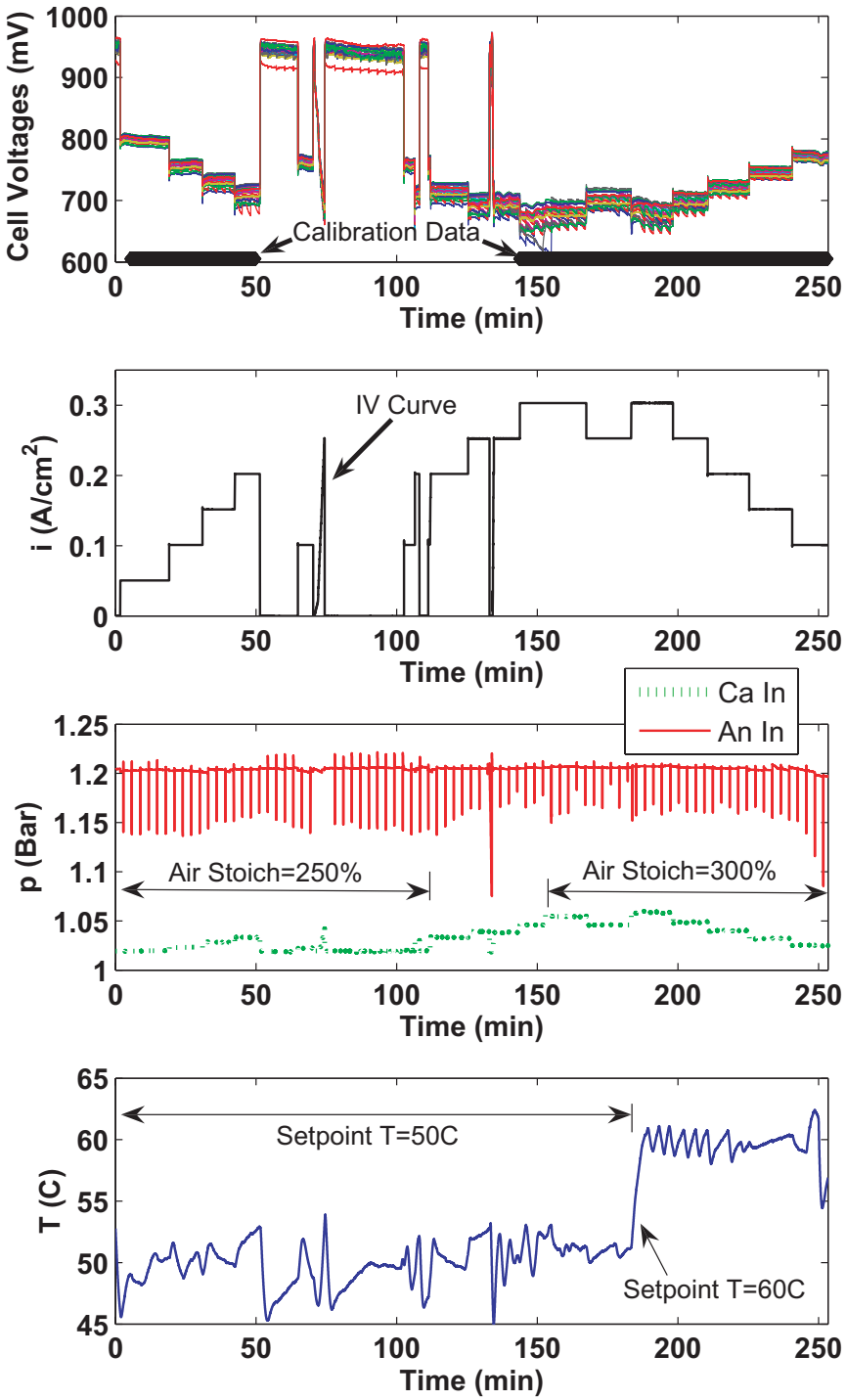

Figure 2.8: Experimental measurements used for model calibration. The first subplot shows the 24 individual cell voltages along with black dots at 600 mV which illustrate the portions of the data set used for calibration. The second subplot shows the nominal current density. The third subplot is the anode and cathode inlet total pressures. The fourth subplot is the temperature of the water coolant leaving the stack.

changed to 60^{o}C at approximately 185 minutes. Thermostatic controllers were used to control the heat exchanger fans to regulate the coolant outlet temperature. As these fans were cycled, oscillations in temperature were induced.

The standard deviation in the cell voltage measurements was greater at high current density (300 mA/cm^2) than at low current density [57]. This increased uncertainty at high current density, seen in Figure 2.8, was due to both the increased difference in the cell to cell voltage variation as well as the increased excursions in cell voltage between anode purges. Moreover, at high current density the cell with the minimum voltage exhibited greater voltage excursions between anode purges than the cell with the maximum voltage. However, the mean and median voltages had similar dynamic and steady-state responses.

For the purposes of model calibration, a portion of the calibration data set was selected to include a range of both transient and "steady-state" operating conditions. This portion of data is indicated with a black *x* in the voltage plot shown in Figure 2.8. Data at open-circuit were avoided due to the high uncertainty associated with operation at open-circuit voltage [57]. The identified parameters resulting in the smallest mean, maximum and standard deviation in the estimation error over the set of $\alpha_w \in$[7,12] and $t_{wl} \in$[0.09mm,0.16mm], while still capturing the trend in the voltage response during flooding conditions, are shown in Table 2.3.

Table 2.3: Experimentally identified parameter values

Parameter	Tuned Value
K_1	1.00
K_2	1.24 μA/cm^2
K_3	2.05
K_4	3.40
α_w	10.0
t_{wl}	0.14 mm

2.10.1 Model Predictions

Using the identified parameters, the model was simulated to produce voltage estimations for the entire calibration data set. Figure 2.9 shows the model estimation at 300 mA/cm^2 between 180-200 minutes. The second subplot compares the nominal current density, $i = I/A_{fc}$, to the apparent current density, i_{app} from Equation 2.38, based on the apparent surface area that is not blocked by the liquid water film at the GDL-channel interface.

As liquid water accumulated in the anode gas channels, the apparent area decreased, causing an increase in the apparent current density. Following a purge, the liquid water was removed and the apparent current density returned to the nominal value. Following some purges, not all of the water was removed from the gas channels, causing the apparent current density to remain greater than the nominal current density. Since the apparent current density was used to calculate the cell voltage, the estimation of cell voltage is then sensitive to the degree of flooding in the anode gas channels and GDL. The values for the identified parameters, α_w and t_{wl} influence the rate at which liquid

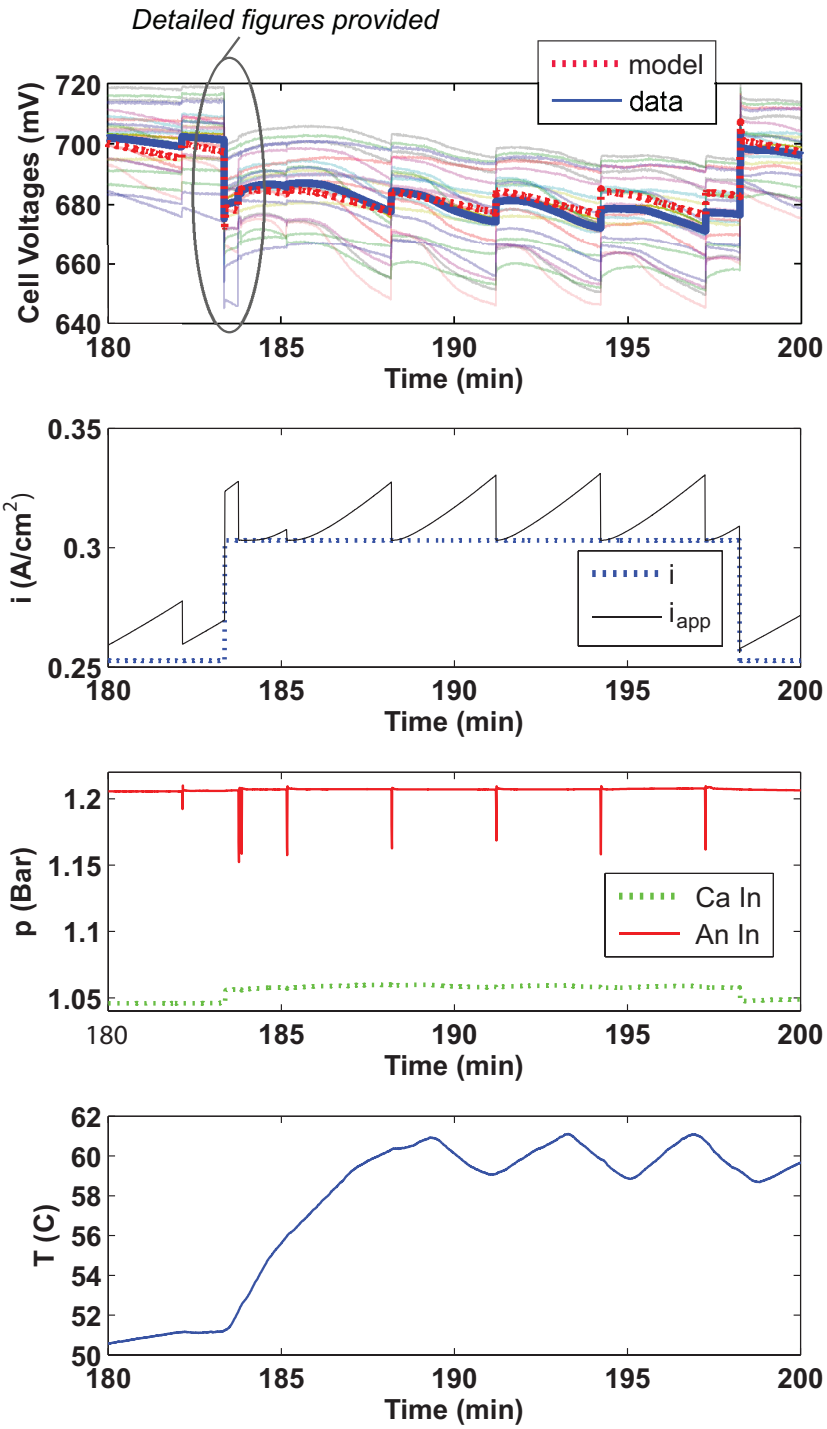

Figure 2.9: GDL model calibration results. The first subplot shows the 24 individual cell voltages with thin faint colored lines, the measurement average voltage in a thick solid blue line, and the estimated voltage in a thick dotted red line. The second subplot shows the nominal and apparent current densities. The third subplot is the anode and cathode inlet total pressures. The fourth subplot is the temperature of the water coolant leaving the stack.

water accumulates in the gas channels (impacting the rate of decay in voltage between purges) as well as how much liquid water mass accumulates in the gas channel (how much the voltage recovers following a purge). When all of the liquid water was removed from the gas channels, the cell voltage returned to approximately the same value following each purge event.

Although the voltage prediction is an indirect means for evaluating the overall predictive ability of our model, voltage is a stack variable that combines the internal states of the stack and provides an accessible, cheap, fast and accurate measurement. The model accurately captured the trend of the voltage decay and subsequent recovery after an anode purging event. Note here, for the entire calibration data set, the average estimation error was 2.9 mV, the maximum estimation error was 42 mV and the standard deviation in the estimation error was 3.6 mV.

In addition to adequately capturing the temporal evolution in voltage during flooding, the model accurately estimated the reactant dynamics during load changes. The overshoot in cell voltage during a step change up in current from 0.25 A/cm^2 to 0.3 A/cm^2 at approximately 183.4 minutes, is shown in detail in Figure 2.10, along with subsequent purging events near 183.7 minutes. A decrease in the partial pressure of oxygen at the cathode membrane surface occurs due to volume filling dynamics; however, there was very little deviation in the hydrogen partial pressure during the load change. As a result, the reactant starvation occurred predominantly on the cathode and not the anode under these operating conditions. Referring back to Figure 2.9, the overshoot in cell voltage at approximately 198 minutes for a step change down in current from 0.3 A/cm^2 to 0.25 A/cm^2 is also well approximated. Note here, for simulations of reactant dynamics during a load change reported in [53] and [73], the model predictions were not compared with experimental data.

Figure 2.11 displays the predicted water vapor partial pressures, the liquid water saturation, and the mass of liquid water accumulating in the anode channel during the same load change and subsequent purging events as described previously for Figure 2.10. The slow rise in the water vapor partial pressure was due to the increase in the cell operating temperature.

Immediately following the purge valve opening, the mass of liquid water in the anode channel was evaporated into the bulk gas stream (due to the increased hydrogen mass flow rate during the purge). The volumetric condensation coefficient, γ in Equation 2.5, influenced the non-instantaneous rate of evaporation of water vapor in the GDL section allowing the water vapor partial pressure to decrease before all of the liquid water was removed from the GDL sections.

The liquid water saturation in the GDL section closest to the channel, $s_{an}(3)$, decreased most significantly during a purge. Liquid water flowed from the GDL towards the channel until the immobile saturation limit was reached, $s_{an}(3) \leq s_{im}$, at which point only water vapor entered the channel from the GDL. Liquid water does not flow from the GDL to the anode channel, following the purge, until the liquid water saturation in the GDL exceeded the immobile saturation limit. If the purge event were to have occurred over a longer time interval, more water vapor in the anode GDL would have been removed, causing a more significant impact on the cathode liquid water saturation due to the water vapor transport through the membrane.

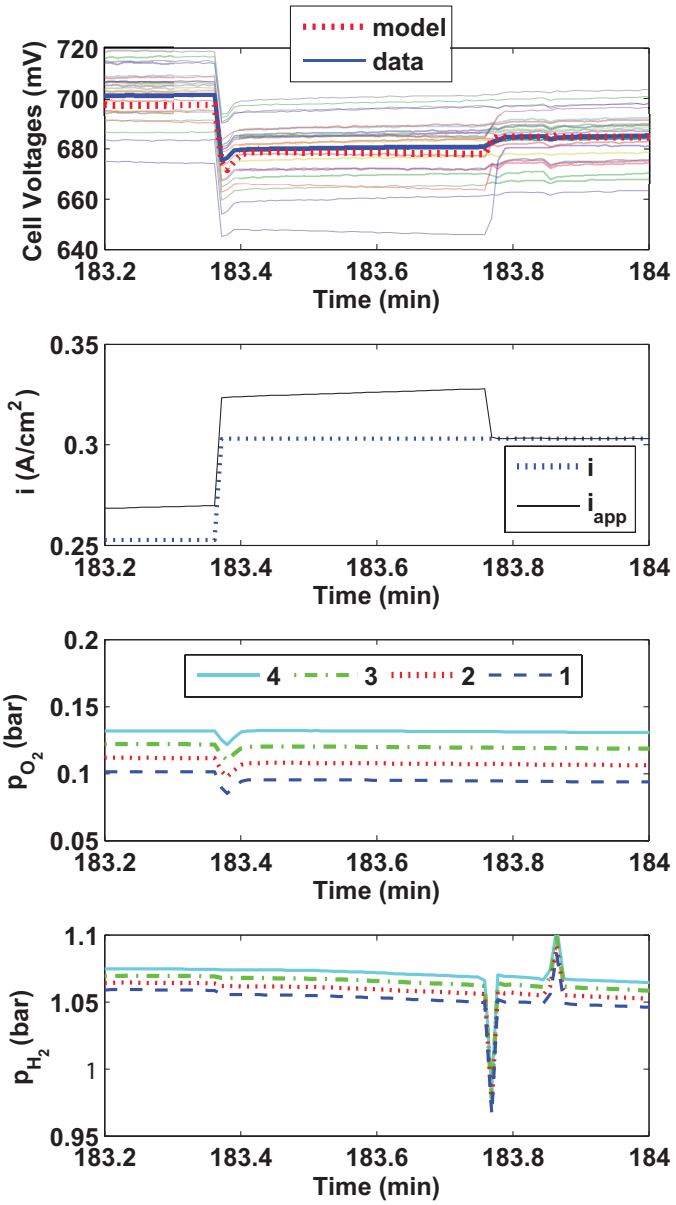

Figure 2.10: Reactant dynamics during a load change and anode purging event. The first two subplots show the cell voltages along with the nominal and apparent current densities. The 24 individual cell voltages have thin faint colored lines with the measurement average voltage in a thick solid blue line and the estimated voltage in a thick dotted red line. The third and fourth subplots show the oxygen and hydrogen partial pressures in each GDL section (1-3) as well as in the channel (4). A load change and anode purging event occurs at approximately 183.4 and 183.8 minutes, respecitvely.

2.10.2 Estimation Sensitivity to Tunable Parameters

The sensitivity of the voltage parameters, K_1-K_4, to the water related tunable parameters is shown in Figure 2.12. The first voltage parameter, K_1, which scales the total activation overvoltage and effectively shifts the polarization curve at low current density, is most sensitive to the thickness of

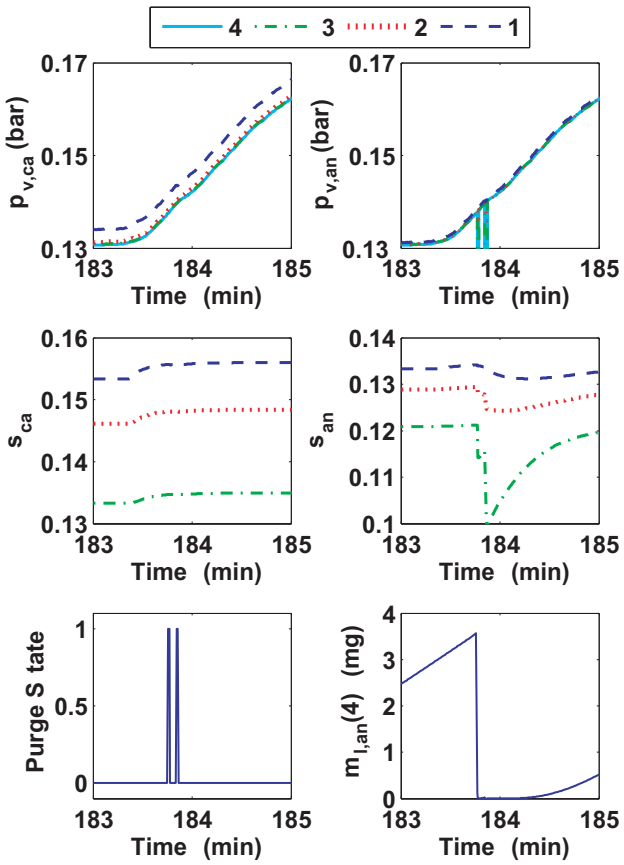

Figure 2.11: Water dynamics during a load change and anode purging event. The first row of subplots shows the water vapor partial pressures in the GDL and channels. The channel is indicated by a solid line and the three GDL sections are represented by dashed lines. The second row of subplots displays the liquid water saturation in the GDL. Finally, the third row of subplots indicates first the state of the purge solenoid valve (0 indicates the valve is closed and 1 means the valve is open), followed by the mass of liquid water accumulating in the anode channel.

the anode channel water layer as α_w increases. The second and third tunable voltage parameters, K_2 and K_3, influence the exchange current density and tend to increase as α_w increases or t_w decreases. The fourth tunable voltage parameter, K_4, which scales the ohmic overvoltage and shifts the linear portion of the polarization curve, decreases as α_w increases or t_w decreases.

As expected for all four voltage parameters, a greater change in the K value occurs as α_w increases. If less water is transported to the anode from the cathode (small α_w), then less liquid water accumulates in the anode gas channel, the apparent current density approaches the nominal current density, and a single set of K parameter values results. In addition, for a given α_w, as t_{wl} increases, the voltage parameters will approach the value seen at low α_w. Physically, a small α_w or large t_{wl} results in less voltage sensitivity to anode flooding. Interestingly, for large α_w, the K_2 voltage parameter, which scales the exchange current density and influences the activation overvoltage, is most sensitive to t_{wl}. The influence of α_w and t_{wl} on the temporal voltage evolution will be discussed

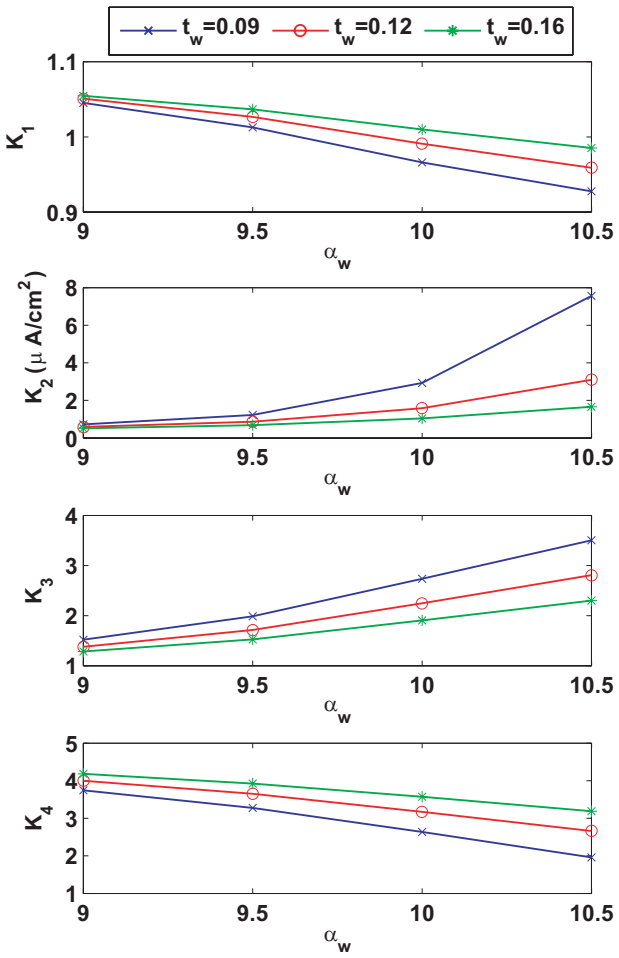

Figure 2.12: Sensitivity of the voltage parameters on the water related tunable parameters.

further.

Of course, the resultant tuned value of the voltage parameters is not of significance as compared to the resulting voltage estimation. As a result, the estimation error statistics over the calibration data set were compared at various [α_w,t_{wl}] pairs. The mean and standard deviation in the voltage estimation error, $\overline{v}(t) - \hat{v}(t)$, as a function of the tunable water-related parameters, α_w and t_{wl}, are shown in Figure 2.13. In general, over the range of parameter values considered, an increase in α_w results in an increased estimation error mean and standard deviation and an increase in the thickness of the water layer accumulating in the anode gas channel, t_{wl}, results in a decrease in the estimation error statistics.

Interestingly, a decreased estimation error does not imply that the estimation is improved. For example, for small α_w the net water vapor mass transport from the cathode to the anode is decreased, implying less liquid water accumulates in the anode gas channel, resulting in a voltage estimation which does not appreciably vary between purges. Of course, to increase the sensitivity of voltage on the accumulation of water mass in the anode channel for a given α_w, the t_{wl} parameter could be

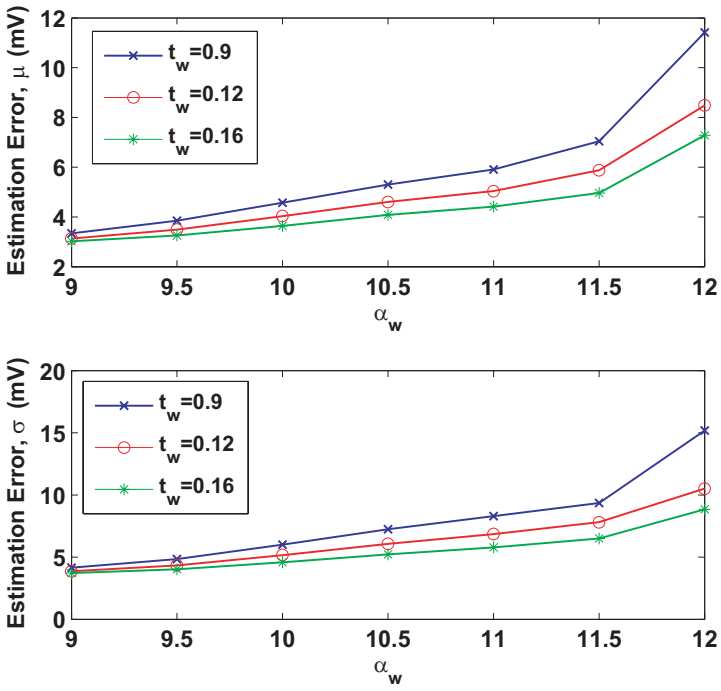

Figure 2.13: Voltage estimation error mean and standard deviation as a function of the water related tunable parameters.

decreased to increase the temporal voltage degradation between purges. As seen in Figure 2.13, as α_w increases, the change in the estimation error for varying t_{wl} also becomes more prominent.

Physically, as the net membrane water mass transport from the cathode to the anode increases, by increasing α_w, an increased mass of liquid water accumulates in the anode gas channel. At a given liquid water layer thickness, t_{wl}, this increased water mass results in a faster voltage degradation between purges. However, each new value for these tunable water related parameters results in a different set of optimal set of voltage parameters, K_1-K_4. Figure 2.14 compares the influence of the tunable water-related parameters on the voltage estimation between purges when new optimal voltage parameters, K_1-K_4, are generated for each pair of water-related parameters, [α_w,t_{wl}]. In this case, an increased α_w shifts the voltage estimation however maintains a similar voltage degradation, whereas t_{wl} has a more significant impact on the voltage decay rate.

However, if the voltage parameters are not recalculated for each new [α_w,t_{wl}] pair and instead are kept at the identified values shown in Table 2.3, the influence of these water related parameters is more obvious, as shown in Figure 2.15. The sensitivity of the voltage estimation is now much more pronounced. Additionally, the impact of the increased membrane water transport on the voltage decay rate between purges is clear. Note, the mass of liquid water accumulating in the anode channel is a function of α_w and not t_{wl} or the voltage parameters.

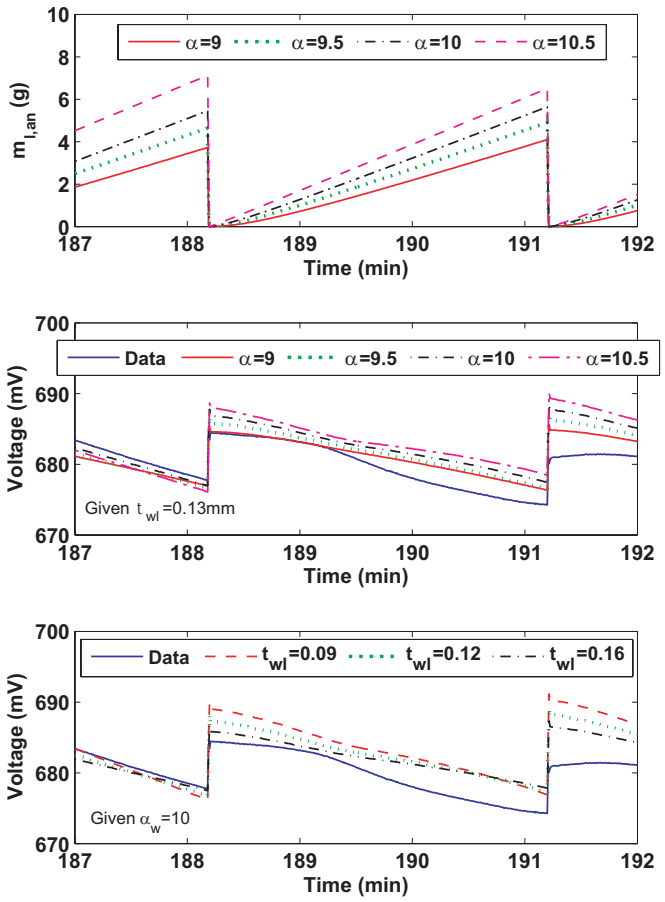

Figure 2.14: Influence of the water related tunable parameters on the accumulation of liquid water in the anode channel and the resultant voltage estimation. The first subplot shows anode channel liquid water mass. The second and third subplots show the voltage estimation as a function of α_w and t_{wl}.

2.11 Model Validation Results

For the purposes of model validation, the calibrated model was simulated with experimental inputs that were not considered in the calibration process. The resulting model predictions are shown in Figure 2.16 and compared with the actual cell voltage measurements at five different load levels. The data shown demonstrates the model predicting capability over a range of current densities and air stoichiometries. At approximately 162 minutes, the air stoichiometry was increased from 200% to 300%, causing a more significant increase in the voltage estimation (through the partial pressure of oxygen at the membrane boundary) than was experimentally observed. Despite the increased error associated with the oxygen partial pressure, the model correctly estimated the degree of anode flooding at various current densities, correctly predicting no significant flooding at low loads. As the load level was reduced, the degree of flooding decreased, which is seen from inspection of the difference between the apparent and nominal current densities at each load level. As a result, the

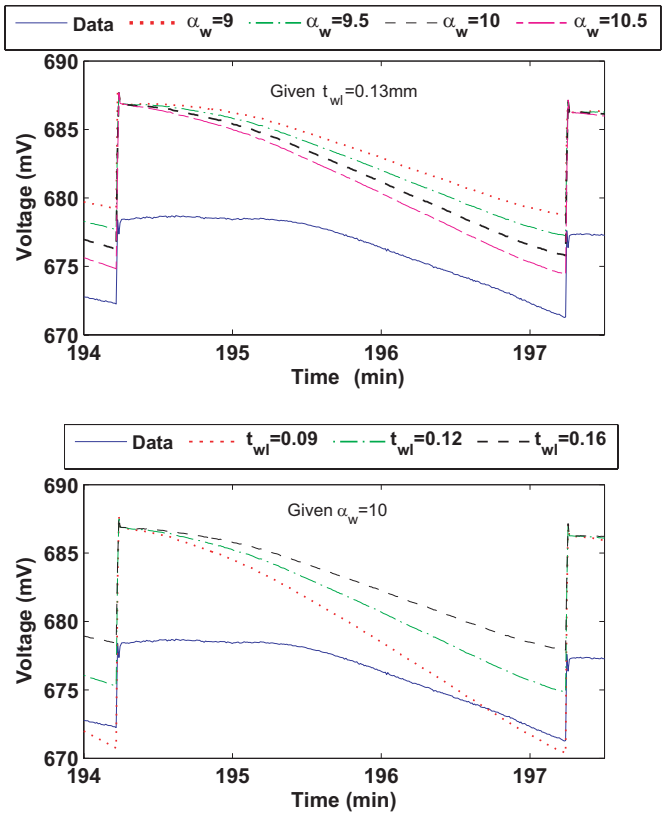

Figure 2.15: For fixed voltage parameters, the influence of the water related tunable parameters on the voltage estimation.

deviation in voltage decreased between purges, which was experimentally confirmed.

For the entire validation data set, the average estimation error was 8.7 mV, the maximum estimation error was 105 mV and the standard deviation in the estimation error was 11.5 mV. Although these validation error statistics are approximately two times greater than the error statistics associated with the calibration data, at all times throughout the experiment the estimated average cell voltage was bounded between the measured minimum and maximum cell voltages and the measured cell to cell variation was larger than the average estimation error.

Although the model of the reactant and water dynamics results in an accurate estimation of the voltage degradation between purges, we have made the assumption that this degradation was solely due to the accumulation of liquid water in the gas channels. However, it is conceivable that some of this degradation could be due to the accumulation of nitrogen on the anode as a result of operation with air, rather than pure oxygen, or catalyst flooding. Our model has tunable parameters that can compensate for these model assumptions and simplifications, but it is very important to check the tuned parameter values against other published values. As Table 2.3 shows, the tuned α_w and t_{wl}, are reasonable and within the range of published results [56, 10].

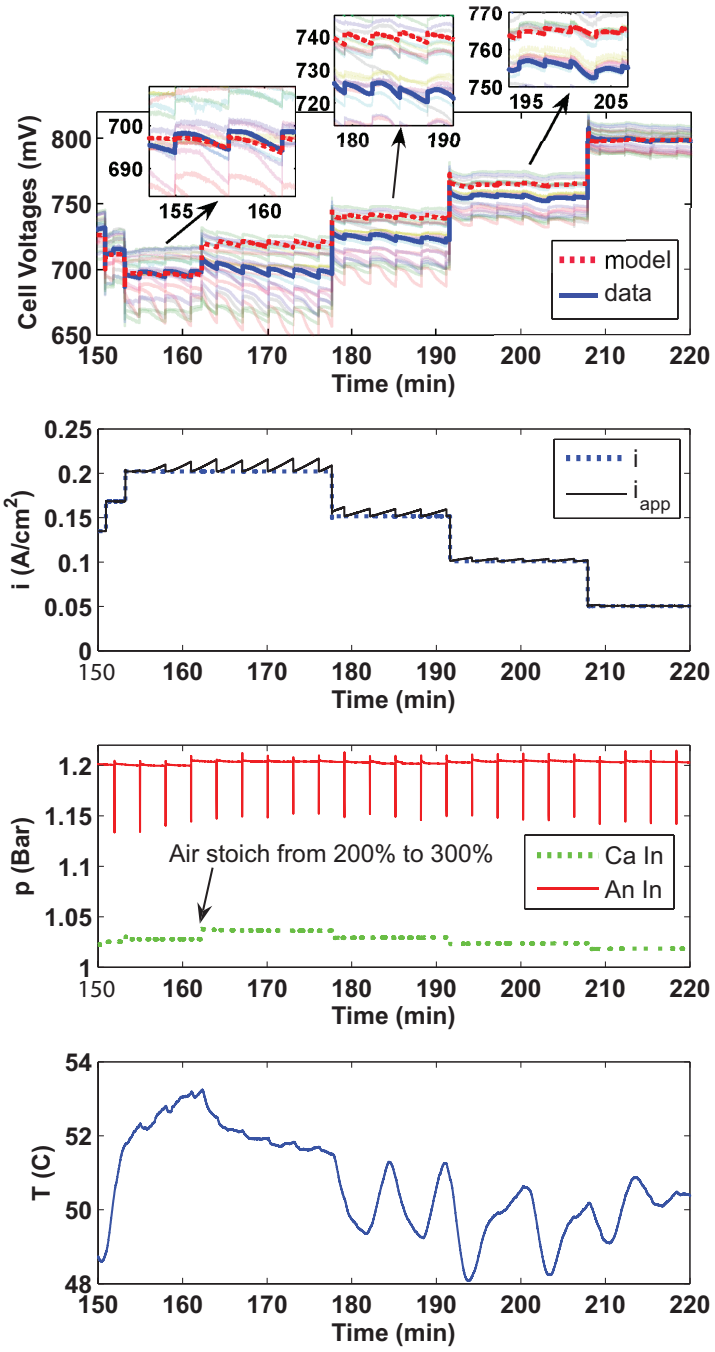

Figure 2.16: GDL model validation results. The first subplot shows the 24 individual cell voltages in thin faint colored lines with the average cell voltage based on the measurements in a thick solid blue line and the estimated cell voltage in a thick dotted red line. The second subplot shows the nominal and apparent current densities. The third subplot contains the anode and cathode inlet total pressures. The fourth subplot is the temperature of the water coolant leaving the stack.

Chapter 3

Membrane Based Humidification System Model

To actively manage the amount of water entrained in the reactant gas streams supplied to the fuel cell stack, a membrane based external humidification system is proposed. Much like the fuel cell model presented in Chapter 2, the humidification system leverages input/output measurements for cheap, accurate and fast control. To design adequate controllers for the coordination of this humidification system, a low order, control-oriented model was devised based on first principles and is calibrated and experimentally validated, as shown in this chapter. Although we have focused on humidifying the cathode reactant stream, the same techniques could be applied to the anode reactant stream as well. The subsequent control objectives, controller development, and closed loop implementation are later discussed in Chapter 4.

3.1 Humidification System Operation

This section provides an overview of the humidifier system operation and design criteria. The experimental hardware associated with the humidification system is then detailed, including sensor and actuator specifications, placement and functionality. While this humidification system is capable of regulating either the anode (hydrogen) or cathode (air) gas streams, the system was designed for pre-treatment of the reactants supplied to the fuel cell cathode.

3.1.1 System Description

The external, membrane-based, humidification system is used to control both fuel cell cathode inlet relative humidity and temperature. The purpose of the external humidifier is to deliver moist air to the cathode inlet of the PEMFC stack between 50^o-65^o C and 50%-100% relative humidity at dry air mass flow rates between 0-45 slm. These specifications are based on the expected operating temperature and current density range of an 8-cell PEMFC stack with an active area of 300cm^2.

To control the temperature and the amount of water vapor entrained with the air supplied to the fuel cell, a membrane-based humidifier, water heater, water reservoir, air bypass, and gas mixer are used. The path of the air and water are shown in Figure 3.1 along with the coupling of the humidification system and the fuel cell stack.

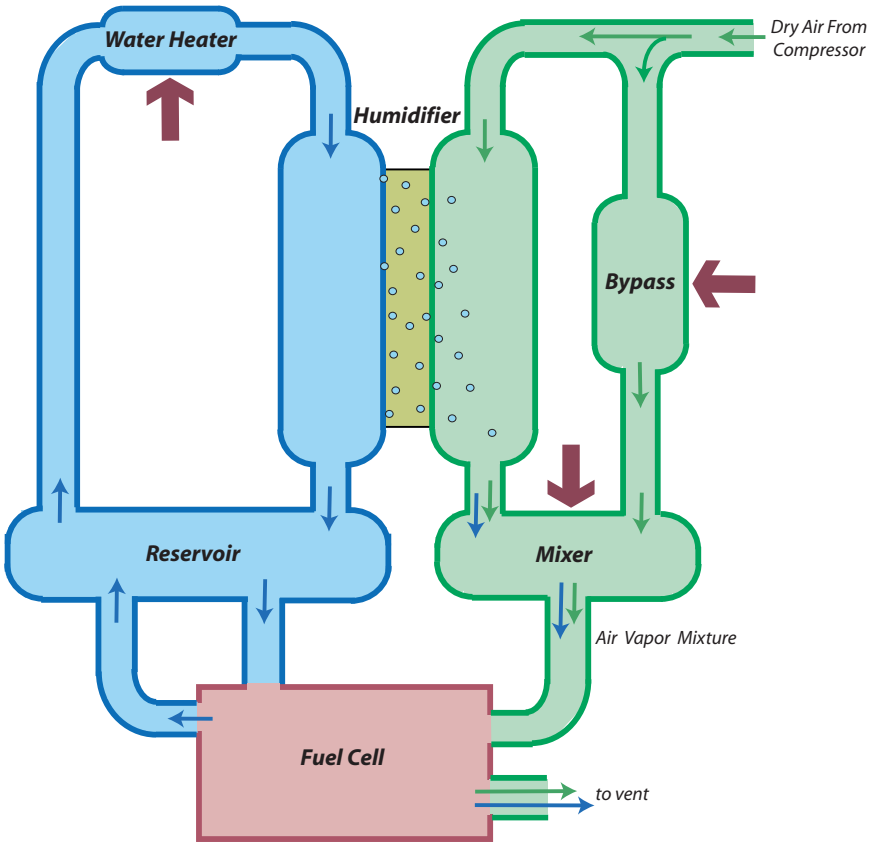

Figure 3.1: External humidifier system overview, detailing the reservoir, water heater, humidifier, bypass, and gas mixer as well as the relationship of the humidification system to the fuel cell stack. The small thin arrows indicate flow directions and the large thick arrows indicate locations where heat is added to the system.

The humidifier is designed to produce a saturated air-vapor mixture at a temperature that is controlled by the water heater. The humidifier utilizes specially design polymeric membranes to permit vapor transport through the membrane without transferring liquid water. Air is introduced to the surface of one side of the membrane, while liquid water passes across the other surface. Due to the water concentration gradient across the membrane, liquid water evaporates and is transported through the membrane to be injected into the air stream. This polymeric membrane is also thermally conductive, allowing the hot liquid water to heat the relatively cold incoming air. The membrane surface area and the number of humidification cells are designed to ensure that the air leaving the humidifier is saturated for the entire range of expected operating temperatures, mass flow rates, and membrane pressure gradients.

The total air mass flow rate (through the humidifier and bypass) is dictated by the fuel cell load demand and desired stoichiometric ratio of air delivered to the fuel cell cathode. Thus, the total dry air mass flow rate through the humidification system can be thought of as a disturbance. By controlling the amount of this total air flow demand supplied to the humidifier and that bypassed around the humidifier, to be joined in the gas mixer, the relative humidity of the mixer exhaust gas can be reg-

ulated. The dry air is supplied to the humidification system at approximately ambient temperature and is delivered to mass flow controllers (MFCs). These MFCs are used to independently control the mass flow rate of air supplied to the humidifier and the bypass.

A critical aspect of operating the air-vapor circulation system, is preventing condensate from forming. Remember, the flow of air leaving the humidifier is a saturated air-vapor mixture at some temperature dependent upon the operating conditions of the humidifier. If the air bypassing the humidifier is colder than the air leaving the humidifier, the mixture of the two gas streams will create condensation. As a result, the bypass temperature must be well regulated by the bypass heater. To further avoid condensation during gas mixing, the mixer is heated to maintain the desired temperature prior to being supplied to the cathode of the PEMFC stack.

Liquid water is delivered to the humidifier system from the water reservoir and circulated through the water heater and humidifier before returning to the reservoir, comprising the humidifier water circulation system. To minimize hardware complexity, this water reservoir is physically shared with the PEMFC stack such that two streams of the liquid water are supplied to the reservoir at different temperatures and leave the reservoir at the same temperature, implying that the reservoir is well mixed. A desired amount of heat is added to the humidifier water circulation system in the water heater. This controlled liquid water temperature is used to regulate the temperature of the air leaving the humidifier.

3.1.2 Experimental Hardware

The external humidifier system experimental hardware, shown in Figure 3.2, was installed at the Fuel Cell Control Laboratory at the University of Michigan. The design and installation of the humidifier equipment was completed in collaboration with the Schatz Energy Research Center at Humboldt State University.

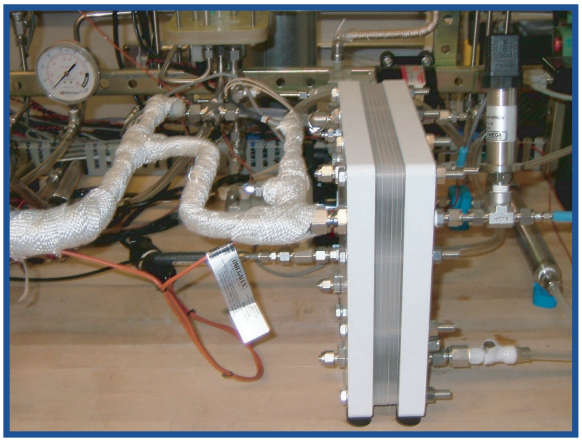

Figure 3.2: External gas humidification system installed at the Fuel Cell Control Laboratory, University of Michigan.

A detailed schematic of the humidifier system hardware is provided in Figure 3.3, illustrating the location of the sensors and actuators used to control and monitor the gas humidification system.

Note, the air, water, data acquisition, and signal conditioning test bench subsystems used to regulate the air and liquid water supply to and from the humidification system were previously shown in Figure 1.5.

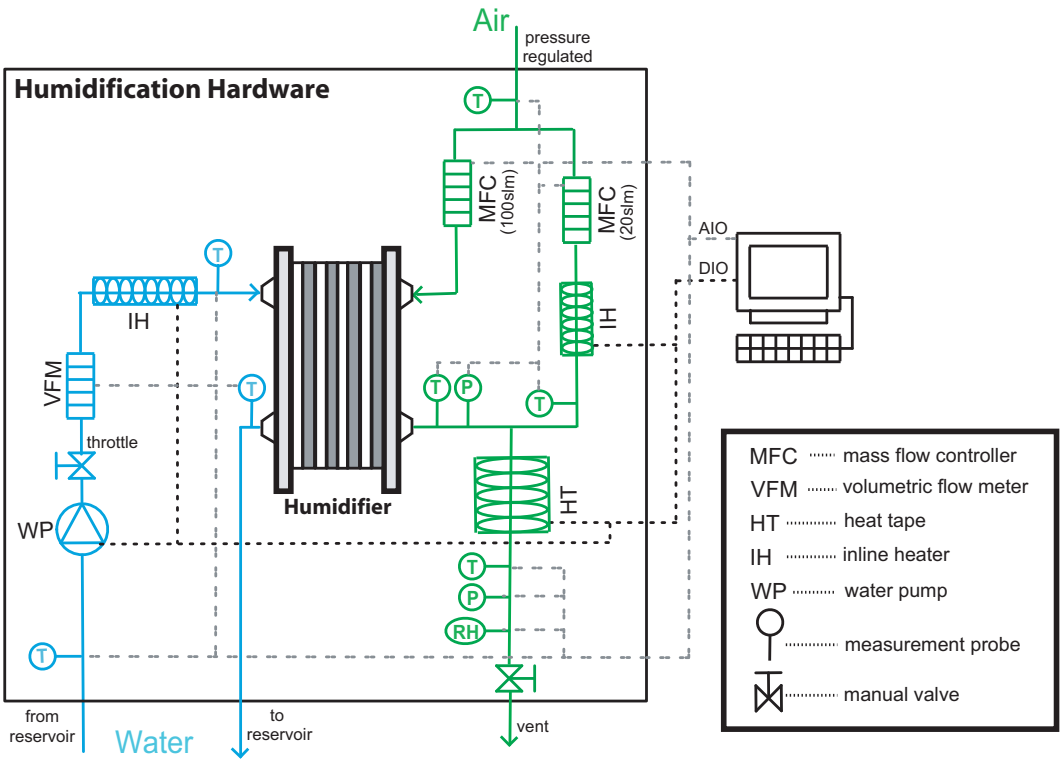

Figure 3.3: Schematic of the gas humidification system hardware, detailing sensor and actuator placement.

The humidifier water circulation system contains a water pump, manual throttle valve and water flow meter for controlling and monitoring the liquid water mass flow rate. A 1000W inline water heater is used to heat the liquid water as it enters the humidifier. A manual bleed valve, not depicted in Figure 3.3, is located between the liquid water humidifier outlet manifold and the top of the reservoir to prevent air from accumulating on the water side of the humidifier membranes[1].

The air system utilizes two separate mass flow controllers directing air through the bypass and the humidifier. The bypass air is heated with a 50W inline resistive heater. Heat tape, containing a resistive heating element embedded in silicon rubber, is wrapped around the outside surface of the gas mixer stainless steel tubing to provide 52W of heat. All air plumbing is insulated with fiberglass cloth; however, this cloth does not provide enough insulation to justify the assumption that the plumbing systems can be treated as adiabatic (this claim will be substantiated by experimental parameter identification).

The membrane based humidifier employs solid expanded teflon (ePTFE) GORE® SELECT^{TM} ionomer composite membranes for water vapor transport from the liquid water to the air. Air and

[1]Due to the air concentration gradient across the humidifier membranes, air is transported from the air to the water side of the membranes, creating an air pocket unless properly removed.

liquid water are transported to opposite sides of the humidifier membranes using channels milled into sheets of polypropylene. The humidifier membranes also contain bonded sheets of polytetrafluoroethylene (PTFE) gaskets for sealing purposes. Finally, the channels and membranes are held together with phenolic endplates used to maintain cell compression.

Temperature is measured as the air enters the humidifier system, and exits the humidifier, bypass and mixer. The liquid water temperature is measured as the water exits the reservoir, enters the humidifier and exits the humidifier. The liquid water volumetric flow rate is measured between the reservoir and the water heater, prior to entering the humidifier. Total air pressure is measured at the exit of the humidifier and the exit of the mixer. Relative humidity is measured at the exit of the mixer, prior to entering the fuel cell cathode. The dry air mass flow rates are measured upstream of the humidifier and bypass.

The instruments used to monitor relative humidity, pressure, flow and temperature are listed in Table 3.1. Included in this table are technical specifications detailing sensor range, accuracy, and response time. Additionally, the measurement bin size associated with the precision of the data acquisition system is tabulated. Note, the sensor resolution and response times are provided by the component manufacturers and have not been verified.

Table 3.1: Sensor and Controller Specifications.

Description	**Range and Accuracy**	**DAQ Precision**	**Response Time**
MKS Bypass MFC	4.1-410±4.1 mg/s	0.01 mg/s	0.5 s
MKS Humidifier MFC	0.02-2±0.02 g/s	0.07 mg/s	0.5 s
McMillan Water MFM	3-83±3 g/s	3 mg/s	not avail.
Rotronic RH sensor SP05 probe (C94 capacitive sensor) M2 series transducer, Pt RTD	$0-100\% \pm 1.5\%$ $-40-60^{\circ}$C $\pm 0.3^{\circ}$C	0.003% 0.003°C	not avail.
Omega pressure transducer PX4202-005G5V	0-34.47±0.083 kPa	1 Pa	10 ms
Omega type T thermocouple	$-100-400^{\circ}$C $\pm 1.0^{\circ}$C	0.02°C	0.3 s

To control the bypass or mixer heater, a continuous signal is commanded through software to a phase-fired solid state relay. The user/controller specifies the amount of power to be provided to the heater. This software command is then converted to a continuous signal as an input to the relay unit. The relay unit then provides a controllable fraction of a 60Hz sine wave to the heater which corresponds to the desired heater power. For example, if the heater is rated at 50W, a 2.5 VDC signal (half of the total possible analog output signal) would result in half of the 60Hz sine wave being provided to the heater, in turn supplying 25W of heat. The water heater is controlled by providing a digital pulse width modulated signal from the computer to the optically isolated digital relays on the digital backplane. This relay switches 120VAC which is provided directly to the water heater.

With these hardware control configurations, the controller update frequencies are dependent on the software scan rates.

To account for signal bias using the phase-fired solid state relays, the heater electrical control system was calibrated by relating the software command to the actual heater power out. A calibration curve was incorporated to remove this bias, assuming the bias is constant. However, noise in the commanded signal may not be constant and can never be eliminated. To reduce the number or measurements required to control and monitor the humidification system, the control signals are not directly measured. Instead, the ”measured” input signal is in fact the software command which contains no noise.

3.2 Model Development

The humidifier system was divided into five control volumes, namely the reservoir, water heater, humidifier, bypass, and mixer, physically depicted in Figure 3.4 in plan view. Applying the conservation of mass and energy, the humidifier system thermal dynamics are derived. First, the general modeling assumptions are stated and the nomenclature is detailed, then the models are presented for the individual control volumes. Finally, a summary of the derivation results is presented in Section 3.3 for quick reference.

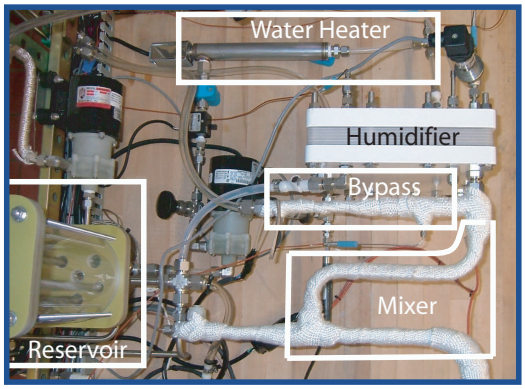

Figure 3.4: Plan view of the external humidifier with the individual control volumes labeled.

3.2.1 Modeling Assumptions Employed

Several assumptions were made in developing the humidifier model presented in Section 3.2. Assumptions that apply to all of the control volumes considered will be stated and justified here. However, additional assumptions have been applied to conditions that are specific to a particular control volume. In such a case, the assumption will be clearly stated within the applicable model development section. Note, extensions of these models to higher temperature or pressure operation should be made with caution.

A1 There is no radiative heat loss from the control volumes. The heat transfer from the control

volume surfaces to the surroundings occurs through free surface natural convection and radiation. Due to the relatively small thermal gradients (0-40^{o}C), the heat losses from the control volume to the surroundings are assumed to be a linear function of their difference in temperature. This assumption is made for model simplicity, to reduce the number of unknown parameters requiring experimental identification, and will result in an overestimation of the convective heat losses by effectively lumping both convection and radiation effects.

A2 There is no change in mass stored within the control volumes. For the gases, the relatively narrow range of operating temperatures (40-65^{o}C) and pressures (near atm) indicate that the change in the gas mass is negligible. Additionally, the physical gas restrictions due to the system design, and the relatively fast response of the air mass flow controllers compared with the thermal dynamics, also indicate that mass dynamics can be neglected. Finally, liquid water can be treated as incompressible.

A3 All constituents have constant specific heat. The specific heat of a gas or liquid is a function of temperature. However, the range of system operating temperatures (40-65^{o}C) is relatively narrow, indicating that the constituent specific heats can be treated as known constant parameters.

A4 The gases behave ideally. The range of operating temperatures and pressures of the system permits the assumption of ideal gas behavior.

A5 Each control volume is homogenous and lumped parameter with no spatial distribution. This assumption is made for simplicity since the model is intended for controller design. Caution should be used if extending this work to elucidate design implications.

3.2.2 Humidifier Nomenclature

The nomenclature used throughout this section aims to clearly describe the material constituent, the control volume considered and the location within the control volume where the variable is being estimated or measured. This information is provided in the subscripts, separated by commas. The English letter A in (m^2) is used to denote surface area, C in (J/kg K) for constant volume specific heat, C_p in (J/kg K) for constant pressure specific heat, $\bar{h}$ in (W/m^2 K) for heat transfer coefficients, m in (kg) for mass, p in (Pa) for pressure, Q in (W) for heat added to a control volume, r for the fraction of the total mass flow rate, T in (K) for temperature, and W in (kg/s) for mass flow rate. Subscripts are used to indicate first the substance of interest, where a is for air, b for bulk materials, g for gas (often indicating a mixture such as air and water vapor), l for liquid water and v for water vapor; secondly the control volume such as bp for bypass, ca for cathode, cv generically for control volume, r for reservoir, fc for fuel cell, wh for water heater, hm for humidifier, and mx for mixer; finally the location is specified by an i or o indicating the control volume inlet or outlet, or amb for ambient. For a full list of the nomenclature used, refer to the Symbols section at the front of this thesis.

3.2.3 Generic Two Volume Thermal Model

Each control volume is comprised of the material flowing through it, consisting of gases and/or liquid water, and the bulk materials that contain it, such as stainless steel or acrylic. A general description of the heat transfer mechanisms and constituent flows are shown in Figure 3.5. Note,

this same schematic is used to represent the volumes containing liquid water by simply changing the subscript from g to l. Following the presentation of the generic model, each control volume will be detailed individually as an extension of this simple case.

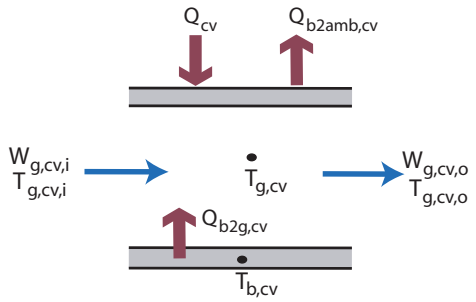

Figure 3.5: General description of the heat transfer mechanisms for control volumes containing bulk and gas states.

The temperature state, $T_{b,cv}$, represents the lumped temperature of the bulk materials which make up the control volume and the gas temperature state, $T_{g,cv}$, represents the temperature of the gases inside the control volume (between the bulk materials). Gas is supplied to the control volume at a specified mass flow rate, $W_{g,cv,i}$, and temperature $T_{g,cv,i}$. Gas leaves the control volume at $W_{g,cv,o} = W_{g,cv,i}$, at the temperature $T_{g,cv,o}$. Heat is transferred to the bulk materials through a resistive heater, denoted by Q_{cv}, which then transfers by forced convection from the bulk materials to the gases by $Q_{b2g,cv} = \bar{h}_{b2g,cv} A_{b2g,cv}(T_{b,cv} - T_{g,cv})$. Heat transfer from the bulk materials to the ambient occurs via natural convection and is represented by $Q_{b2amb,cv} = \bar{h}_{b2amb,cv} A_{b2amb,cv}(T_{b,cv} - T_{amb})$. The heat transfer coefficients associated with forced convection are a function of mass flow rate, $\bar{h}_{b2g,cv} = \beta_{b2g,cv,1} W_{g,cv,i}^{\beta_{b2g,cv,2}}$, where as the heat transfer coefficients associated with natural convection are constant, $\bar{h}_{b2amb,cv} = \beta_{b2amb,cv}$.

Applying the conservation of energy separately to the gas and the bulk materials within the control volume, the change in energy stored in these two volumes is described by

$$\begin{aligned} \Delta\dot{E}_{g,cv} &= W_{g,cv,i} h_{g,cv,i} - W_{g,cv,o} h_{g,cv,o} + Q_{b2g,cv} \ , \\ \Delta\dot{E}_{b,cv} &= Q_{cv} - Q_{b2amb,cv} - Q_{b2g,cv} \ , \end{aligned} \tag{3.1}$$

where $\Delta\dot{E}_{g,cv}$ and $\Delta\dot{E}_{b,cv}$ are the rates of change in internal energy of the gas and the bulk materials in the control volume, respectively (W), $W_{g,cv,i}$ and $W_{g,cv,o}$ are the gas mass flow rates to and from the control volume, respectively (kg/s), $h_{g,cv,i}$ and $h_{g,cv,o}$ are the specific enthalpies of the gas flows supplied to and exiting from the control volume, respectively (J/kg), $Q_{b2g,cv}$ is the convective heat transfer from the bulk to the gas materials (W), $Q_{b2amb,cv}$ is the heat transfer from the bulk materials to the ambient (W), and Q_{cv} is the heat added to the control volume by the resistive heater (W).

As the gas travels through the control volume, its internal energy changes due to heat exchange with the bulk materials. For laminar pipe flow with a uniform pipe inner surface temperature, the heat transfer between the surface and the gas at the pipe wall occurs via conduction since the ve-

locity at the liquid solid interface is zero [29]. In thermal equilibrium, the conductive heat transfer through the wall will be equal to the convective heat transfer from the wall to the gas. As a result, the heat transfer from the bulk materials to the gas will be described by surface convection in the form

$$Q_{x2y,cv} = \bar{h}_{x2y,cv} A_{x2y,cv} (T_{x,cv} - T_{y,cv}) \ , \tag{3.2}$$

where $Q_{x2y,cv}$ is the convective heat transfer from material x to material y (W), $T_{x,cv}$ and $T_{y,cv}$ are the temperatures of materials x and y, respectively (K), $\bar{h}_{x2y,cv}$ is the convective heat transfer coefficient (W/m^{2}K), and $A_{x2y,cv}$ is the surface area in contact with both materials x and y (m^2). For the general two volume case presented in Equation 3.1, constituent x represents the bulk materials and constituent y represents the gas.

From Newton's Law of Cooling, the free surface convective heat transfer from a control volume is a function of the difference in temperature between the control volume and its surroundings. This relationship can be expressed in the form:

$$Q_{b2amb,cv} = \bar{h}_{b2amb,cv} A_{b2amb,cv} (T_{b,cv} - T_{amb}) \ , \tag{3.3}$$

where $Q_{b2amb,cv}$ is the convective heat transfer from the control volume to the ambient surroundings (W), $\bar{h}_{b2amb,cv}$ is the convective heat transfer coefficient from the bulk to the ambient (W/m^{2}K), $A_{b2amb,cv}$ is the heat transfer surface area between the bulk materials and the surroundings (m^2), $T_{b,cv}$ is the lumped temperature of the bulk materials (K), and T_{amb} is the temperature of the surroundings (K).

Assuming no change in mass stored in the control volume, constant specific heat, and lumped volumes (no spatial distribution), the change in internal energy stored in a control volume can be expressed as a function of the time rate of change of temperature and the thermal capacitance of the control volume, shown by

$$\Delta \dot{E}_{x,cv} = m_{x,cv} C_{v,x,cv} \frac{dT_{x,cv}}{dt} \ , \tag{3.4}$$

where $m_{x,cv}$ is the mass of material x within the control volume (kg), and $C_{x,cv}$ is the constant volume specific heat of material x in the control volume (J/kg K). Note, for control volumes which contain multiple materials, the lumped constant volume specific heat is calculated as the mass weighted sum of the constant volume specific heats of each material in the control volume.

Applying the assumptions made in 3.2.1 and the conservation of mass, the mass flow rates of gas through the control volume are constant, implying $W_{g,cv,i} = W_{g,cv,o}$. Equations 3.2-3.4, describing the heat transfer rates and the time rate of change of the internal energy, are substituted into the conservation of energy equation (3.1). Thus, the temperature state equations for the bulk and gas

(or liquid water) can be expressed by

$$\frac{dT_{g,cv}}{dt} = \frac{1}{m_{g,cv}C_{g,cv}}\left[W_{g,cv,i}C_{p,g}(T_{g,cv,i} - T_{g,cv,o}) + \bar{h}_{b2g,cv}A_{b2g,cv}(T_{b,cv} - T_{g,cv})\right] , \tag{3.5a}$$

$$\frac{dT_{b,cv}}{dt} = -\frac{1}{m_{b,cv}C_{b,cv}}\left[-\bar{h}_{b2g,cv}A_{b2g,cv}(T_{b,cv} - T_{g,cv}) - \bar{h}_{b2amb,cv}A_{b2amb,cv}(T_{b,cv} - T_{amb}) + Q_{cv}\right] , \tag{3.5b}$$

where C_p is the constant pressure specific heat of the constituent (J/kg K).

Unfortunately, the internal gas temperature state can not be directly measured. As a result, some approximation of the control volume temperature distribution must be made in order to compare the model estimates to measured values, either for model calibration or for control. It is therefore generally assumed that the gas temperature, $T_{g,cv}$, is a linear average between the inlet and outlet temperatures, such that

$$T_{g,cv,o} = 2T_{g,cv} - T_{g,cv,i} . \tag{3.6}$$

In detailing the model for each system control volume, this assumption will be applied and discussed. It is important to keep in mind that the subsystem outlet temperatures are regulated, not the internal states, and thus a good approximation of these outlet conditions is necessary.

For the control volumes which contain bulk temperatures that can not be directly measured (reservoir, water heater, and mixer), the states within these systems must remain coupled during simulation. This coupling implies that the state estimations serve as inputs to each other. For example, the estimation of the gas temperature state, $T_{g,cv}$ is an input to the model estimate of the bulk temperature, $T_{b,cv}$ and vice versa, as shown in Figure 3.6.

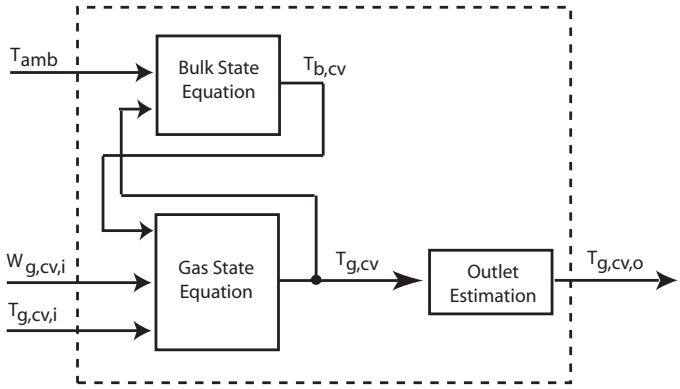

Figure 3.6: Simulation schematic of the general two volume system.

3.2.4 Water Reservoir Model

The liquid water reservoir materials are comprised of phenolic endplates and acrylic walls, along with stainless steel tubing. Although there are cartridge heaters placed within the reservoir, which

are utilized to increase the warm-up time of the PEMFC water circulation system, these cartridge heaters were turned off and thus will not be considered as an additional heat source to the reservoir system. The outside walls of the reservoir are not insulated. Water is supplied to and from the reservoir from both the humidifier and the PEMFC stack. The inputs and outputs to the reservoir are shown in Figure 3.7. Note, no heat is added to the reservoir; consequently, the heat transfer between materials occurs from the liquid to the bulk.

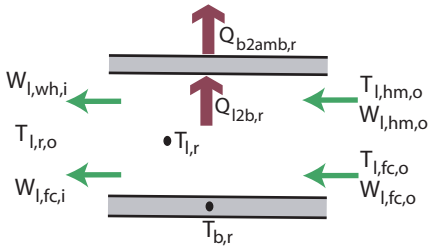

Figure 3.7: Inputs and outputs of the water reservoir.

Applying the assumptions made in 3.2.1, the mass flow rates of liquid water through the reservoir are constant ($W_{l,fc,o} = W_{l,fc,i}$ and $W_{l,hm,o} = W_{l,wh,i}$). Further, the water leaving the reservoir is assumed to be fully mixed and at a uniform temperature, $T_{l,r,o}$. Applying the conservation of energy separately to the liquid water and the bulk materials within the reservoir control volume, following the analysis provided in section 3.2.3, the reservoir thermal dynamics are described by

$$\begin{aligned}\frac{dT_{l,r}}{dt} &= \frac{1}{m_{l,r}C_{l,r}}\left[W_{l,fc,i}C_{p,l}(T_{l,fc,o}-T_{l,r,o}) + W_{l,wh,i}C_{p,l}(T_{l,hm,o}-T_{l,r,o}) - \bar{h}_{l2b,r}A_{l2b,r}(T_{l,r}-T_{b,r})\right], \\ \frac{dT_{b,r}}{dt} &= \frac{1}{m_{b,r}C_{b,r}}\left[\bar{h}_{l2b,r}A_{l2b,r}(T_{l,r}-T_{b,r}) - \bar{h}_{b2amb,r}A_r(T_{b,r}-T_{amb})\right] . \end{aligned} \tag{3.7}$$

The reservoir combines two supplied liquid water streams and therefore the assumption of a linear temperature distribution from the inlet to the outlet does not apply. Due to the relatively large mass of liquid water in the reservoir, it is therefore assumed that the reservoir is thermally well mixed. This assumption also implies that the temperature of the water leaving the reservoir (supplied to either the fuel cell or the humidification systems) is equal to that in the reservoir, such that

$$T_{l,r,o} = T_{l,r} . \tag{3.8}$$

3.2.5 Water Heater Model

The inline water heater consists of a stainless steel heater element along with stainless steel tubing. Unlike the air bypass, the outside walls of the pipe are not insulated. Water is supplied to the water heater by a pump which pumps water from a reservoir to the humidifier. The inputs and outputs to the water heater are shown in Figure 3.8.

Applying the assumptions made in 3.2.1, the mass flow rate of liquid water through the water

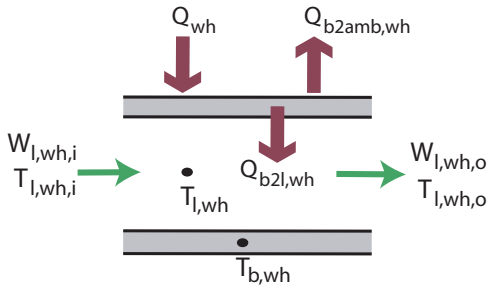

Figure 3.8: Inputs and outputs of the water heater.

heater is constant ($W_{l,wh,i} = W_{l,wh,o} = W_{l,hm,i}$). Applying the conservation of energy separately to the liquid water and the bulk materials within the water heater, following the analysis provided in section 3.2.3, the water heater thermal dynamics are described by

$$\begin{aligned}\frac{dT_{l,wh}}{dt} =& \frac{1}{m_{l,wh}C_{l,wh}}\left[W_{l,hm,i}C_{p,l}(T_{l,r,o} - T_{l,hm,i}) + \bar{h}_{b2l,wh}A_{b2l,wh}(T_{b,wh} - T_{l,wh})\right], \\ \frac{dT_{b,wh}}{dt} =& \frac{1}{m_{b,wh}C_{b,wh}}\left[Q_{wh} - \bar{h}_{b2l,wh}A_{b2l,wh}(T_{b,wh} - T_{l,wh}) - \bar{h}_{b2amb,wh}A_{b2amb,wh}(T_{b,wh} - T_{amb})\right].\end{aligned} \tag{3.9}$$

As with the general two volume model presented, it is assumed that the temperature of the liquid water in the water heater is a linear average between the inlet and outlet temperatures, such that

$$T_{l,wh,o} = 2T_{l,wh} - T_{l,r,o}\ . \tag{3.10}$$

3.2.6 Membrane Based Humidifier Model

The conservation of energy can be applied to a combination of the humidifier control volumes defined by the water, air/vapor mixture, and the bulk materials. The thin polymeric membrane, of similar composition as the membranes employed in the fuel cell stack, are assumed to have no appreciable mass compared to the other control volumes, implying they do not store a significant amount of thermal energy. As a result, the membrane thermal dynamics are neglected in this work.

The humidifier can be considered as a three volume system comprised of the liquid, air and bulk materials. Analysis on this three volume system has indicated that there is little heat transfer between the bulk materials and the air, and a relatively large heat transfer between the liquid and the bulk materials, indicating that the liquid and bulk are in thermal equilibrium. Thus, the system can be adequately characterized by a two volume system. The inputs and outputs to the humidifier volumes are physically depicted in Figure 3.9.

Employing the assumption of liquid and bulk thermal equilibrium, which will be referred to as simply the humidifier liquid water volume, the thermal dynamics of the liquid water and gas can be

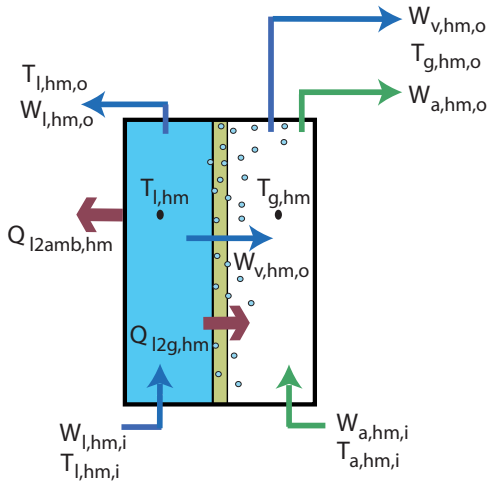

Figure 3.9: Two volume humidifier system.

modeled by applying the conservation of energy, such that

$$\begin{aligned}\Delta\dot{E}_{l,hm} &= W_{l,hm,i}h_{l,hm,i} - W_{l,hm,o}h_{l,hm,o} - W_{v,hm,o}h_{v,hm,o} - Q_{l2g,hm} - Q_{l2amb,hm}\ , \\ \Delta\dot{E}_{g,hm} &= Q_{l2g,hm} + W_{a,hm,i}h_{a,hm,i} - W_{g,hm,o}h_{g,hm,o}\ ,\end{aligned} \tag{3.11}$$

where $\Delta\dot{E}_{l,hm}$ and $\Delta\dot{E}_{g,hm}$ are the rates of change of energy stored in the liquid water and gas within the humidifier (W); $\dot{Q}_{l2g,hm}$ is the heat transfer from the liquid water to the air through the membrane (W); $\dot{Q}_{l2amb,hm}$ is the heat transfer from the liquid water to the ambient (W); $W_{l,hm,i}$ and $W_{l,hm,o}$ are the liquid water mass flow rates into and out of of the humidifier (kg/s); $W_{a,hm,i}$ and $W_{a,hm,o}$ are the humidifier air inlet and outlet air mass flow rates, respectively (kg/s); $W_{v,hm,o}$ is the water vapor mass flow leaving the humidifier entrained in the air exhaust stream (kg/s); and $h_{l,hm,i}$ and $h_{l,hm,o}$ are the liquid water specific enthalpies at the humidifier inlet and outlet (J/kg). Note, it has been assumed that the water vapor is transported to the air from the liquid water at the humidifier air outlet temperature and that the mass flow rate of water vapor entering and exiting the humidifier air volume are equal, implying that the water vapor does not appear in the conservation of energy equation for the air volume.

The mass flow rate of vapor lost to the air is negligible compared to the mass flow rate of liquid water through the humidifier. Additionally, the liquid water is treated as incompressible with constant specific heat. As a result, the mass flow rate of liquid water entering the humidifier is assumed to be equal to the mass flow rate of liquid water leaving the humidifier ($W_{l,hm,i} = W_{l,hm,o}$).

Applying the assumptions made in 3.2.1, along with Equations 3.2-3.4 to describe the convective heat transfers and the time rate of change of the internal energy, Equation 3.11 can be rewritten

as

$$\begin{aligned}\frac{dT_{l,hm}}{dt} =& \frac{1}{m_{l,hm}C_{l,hm}}\left[W_{l,hm,i}C_{p,l}(T_{l,hm,i}-T_{l,hm,o}) - W_{v,hm,o}C_{p,v}T_{g,hm,o}\right.\\ &\left. -\bar{h}_{l2g,hm}A_{l2g,hm}(T_{l,hm}-T_{g,hm}) - \bar{h}_{l2amb,hm}A_{l2amb,hm}(T_{l,hm}-T_{amb})\right] ,\\ \frac{dT_{g,hm}}{dt} =& \frac{1}{m_{g,hm}C_{g,hm}}\left[W_{a,hm,i}C_{p,a}(T_{a,hm,i}-T_{g,hm,o}) + \bar{h}_{l2g,hm}A_{l2g,hm}(T_{l,hm}-T_{g,hm})\right] ,\end{aligned} \tag{3.12}$$

where $T_{l,hm}$ and $T_{g,hm}$ are the humidifier liquid water and air-vapor mixture temperatures, respectively (K); $m_{l,hm}$ and $m_{g,hm}$ are the humidifier liquid water and air-vapor mixtures masses, respectively (kg); $C_{l,hm}$ and $C_{g,hm}$ are the constant volume specific heats of the liquid water and air-vapor mixtures, respectively (J/kg K); $T_{l,hm,i}$ and $T_{l,hm,o}$ are the liquid water temperatures entering and leaving the humidifier, respectively (K); $T_{a,hm,i}$ and $T_{g,hm,o}$ are the air temperatures entering and leaving the humidifier, respectively (K); $W_{l,hm,i}$ and $W_{a,hm,i}$ are the liquid water and air mass flow rates entering the humidifier, respectively (kg/s); $W_{v,hm,o}$ is the water vapor mass flow rate leaving the humidifier (kg/s); $\bar{h}_{l2g,hm}$ and $\bar{h}_{l2amb}$ are the convective heat transfer coefficients between the liquid water and gas and between the liquid water and the ambient, respectively (W/m^{2}K); $A_{l2g,hm}$ and $A_{l2amb,hm}$ are the surface areas between the liquid water and gas and between the liquid water and the ambient, respectively (m^2); and, finally, $A_{l2g,hm}$ and A_{l2amb} are the surface areas between the liquid water and gas and between the liquid water and the ambient, respectively (m^2).

As with the general two volume model presented, it is assumed that the temperature of the liquid water and air in the humidifier are linear averages between their respective inlet and outlet temperatures, such that,

$$\begin{aligned}T_{l,hm,o} =& 2T_{l,hm} - T_{l,hm,i},\\ T_{a,hm,o} =& 2T_{a,hm} - T_{a,hm,i} .\end{aligned} \tag{3.13}$$

Because the water vapor mass flow leaving the humidifier, $W_{v,hm,o}$, can not be directly measured, an estimation must be made. For experimental implementation, the equation quantifying this water vapor mass flow was developed as a function of variables that can be measured, namely temperature, total pressure, relative humidity and dry air mass flow rate. Neglecting humidity dynamics and applying the definition for the humidity ratio, $\omega = \frac{M_v \phi p^{sat}}{M_a(p-\phi p^{sat})}$, the mass flow rate of water vapor can be described by

$$W_{v,hm,o} = \frac{M_v \phi_{g,hm,o} p^{sat}_{g,hm,o}}{M_a(p_{g,hm,o} - \phi_{g,hm,o} p^{sat}_{g,hm,o})} W_{a,hm,i} , \tag{3.14}$$

where M_a and M_v are the molar masses of air and water vapor, respectively (kg/mol);e molar mass of vapor (kg/mol), $p^{sat}_{g,hm,o}$ is the saturation pressure at the humidifier air outlet temperature (Pa), $\phi_{g,hm,o}$ is the relative humidity of the air-vapor mixture leaving the humidifier, and $p_{g,hm,o}$ is the total pressure of the air-vapor mixture leaving the humidifier. A fourth order approximation for the water vapor saturation pressure as a function of temperature ($p^{sat} = f(T)$), is shown in Equation 2.6.

3.2.7 Air Bypass Model

The air bypass consists of a stainless steel inline resistive heater element connected to stainless steel tubing. The outside walls of the pipe are insulated with fiberglass cloth. Air is supplied to the bypass by a mass flow controller. The inputs and outputs to the air bypass are shown in Figure 3.10. Dry air enters the bypass from the ambient and leaves the bypass to the mixer.

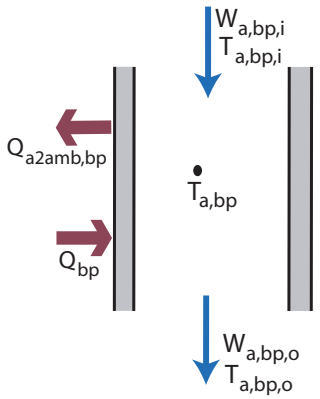

Figure 3.10: Inputs and outputs of the air bypass.

Rather than the generic two volume model presented, the bypass can be simplified as a single volume system. The bypass inline resistive heater is in intimate contact with the air mass, implying heat does not transfer through all of the intermediate bulk materials before reaching the air, as is the case for the mixer heat tape. As compared with the liquid water in the inline water heater, the mass of air inside the bypass is relatively small. As a result, the bypass air and bulk materials are assumed to be in thermal equilibrium.

Similar to the analysis provided in section 3.2.3 for describing the heat transfer coefficients and the change in internal energy, the bypass thermal dynamics can be described by

$$\frac{dT_{a,bp}}{dt} = \frac{1}{m_{bp}C_{bp}}\left[Q_{bp} + W_{a,bp,i}C_{p,a}(T_{a,bp,i} - T_{a,bp,o}) - \bar{h}_{b2amb,bp}A_{b2amb,bp}(T_{a,bp} - T_{amb})\right] . \quad (3.15)$$

As with the general two volume model presented, it is assumed that the temperature of the air in the bypass is the linear average between the inlet and outlet temperatures, such that

$$T_{a,bp,o} = 2T_{bp} - T_{a,bp,i} . \quad (3.16)$$

3.2.8 Mixer Model

The mixer consists of resistive heat tape wrapped on the outside surface of stainless steel tubing. Similar to the air bypass, the outside walls of the pipe are insulated with fiberglass cloth. An air-vapor mixture is supplied to the mixer from the humidifier and dry air is supplied from the bypass. The inputs and outputs to the mixer are shown in Figure 3.11. Unlike the bypass, the heat added to the mixer must first transfer through the stainless steel tubing before reaching the air-vapor gas

mixture. As a result, the mixer is modeled as a two volume system, comprised of the gas and bulk materials.

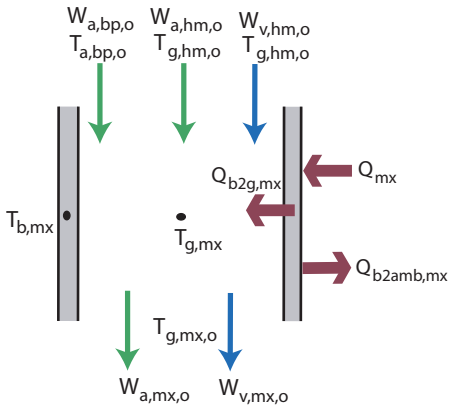

Figure 3.11: Inputs and outputs of the gas mixer.

Applying the assumptions made in 3.2.1, the mass flow rate of water vapor entering the mixer is equal to that exiting the mixer ($W_{v,hm,o} = W_{v,mx,o}$). Additionally, the dry air mass flow rate leaving the mixer is assumed to be equal to that entering the mixer from the humidifier and bypass, such that $W_{a,mx,o} = W_{a,hm,i} + W_{a,bm,i}$, where in the humidifier $W_{a,hm,i} = W_{a,hm,o}$ and in the bypass $W_{a,bp,i} = W_{a,bp,o}$.

Applying the general two volume model from Equation 3.1 to the mixer, accounting for three supplied gas streams and two exhaust gas streams, along with Equations 3.2-3.4 to describe the convective heat transfers and the time rate of change of the internal energy, the mixer thermal dynamics are expressed by

$$\begin{aligned}
\frac{dT_{g,mx}}{dt} &= \frac{1}{m_{g,mx}C_{g,mx}}\Big[(W_{a,hm,i}C_{p,a} + W_{v,hm,o}C_{p,v})(T_{g,hm,o} - T_{g,mx,o}) \\
&\quad + W_{a,bp,i}C_{p,a}(T_{a,bp,o} - T_{g,mx,o}) + \bar{h}_{b2g,mx}A_{b2g,mx}(T_{b,mx} - T_{g,mx})\Big] \ , \\
\frac{dT_{b,mx}}{dt} &= \frac{1}{m_{b,mx}C_{b,mx}}\Big[Q_{mx} - \bar{h}_{b2g,mx}A_{b2g,mx}(T_{b,mx} - T_{g,mx}) - \bar{h}_{b2amb,mx}A_{b2amb,mx}(T_{b,mx} - T_{amb})\Big] \ ,
\end{aligned} \tag{3.17}$$

where $T_{g,mx}$ and $T_{b,mx}$ are the mixer gas and bulk material temperatures (K), $T_{g,mx,o}$ is the mixer outlet gas temperature (K), $m_{g,mx}$ and $m_{b,mx}$ are the gas (air and water vapor) and humidifier bulk masses within the mixer (kg), $C_{g,mx}$ and $C_{b,mx}$ are the constant volume specific heat of the mixer gases and the bulk materials (J/kg K), $\bar{h}_{b2g,mx}$ is the convective heat transfer coefficient from the bulk materials to the gases (J/kgK), $\bar{h}_{b2amb,mx}$ is the convective heat transfer coefficient from the bulk materials to the ambient (J/kgK), $A_{b2amb,mx}$ is the outside surface area of the mixer bulk (m^2), and $A_{b2g,mx}$ is the surface area between the mixer bulk and gases (m^2).

As with the reservoir, the mixer combines two supplied streams and therefore the assumption of a linear temperature distribution from the inlet to the outlet does not apply. The mixer was designed such that the two gas streams, from the bypass and humidifier, are well mixed before leaving the

mixer. It is therefore assumed that the mixer gas temperature is equal to the outlet temperature, such that

$$T_{g,mx} = T_{g,mx,o} \ . \tag{3.18}$$

3.2.9 Relative Humidity Estimation

The relative humidity of the air supplied to the PEMFC from the mixer must be known to ensure adequate controller performance. As a result, an accurate methodology for estimating relative humidity is desired. This estimation will be compared to a relative humidity measurement that has an accuracy of 1.5%. Although the humidity sensor is responsive and accurate for laboratory measurements, it is too expensive and bulky for commercial applications.

To estimate the relative humidity in the mixer outlet, mass conservation is applied to the mixer water vapor. First, it is assumed that the mass flow of water vapor leaving the humidifier, $W_{v,hm,o}$ from Equation 3.14, is equal to the mass flow of water vapor leaving the mixer, $W_{v,mx,o}$. Applying the definition for the humidity ratio, $\omega = \frac{M_v \phi p^{sat}}{M_a (p - \phi p^{sat})}$, evaluated at the humidifier and mixer outlet temperatures results in

$$W_{a,hm,i} \frac{\phi_{g,hm,o} p^{sat}_{g,hm,o}}{p_{g,hm,o} - \phi_{g,hm,o} p^{sat}_{g,hm,o}} = W_a \frac{\phi_{g,mx,o} p^{sat}_{g,mx,o}}{p_{g,mx,o} - \phi_{g,mx,o} p^{sat}_{g,mx,o}}, \tag{3.19}$$

where $\phi_{g,hm,o}$ and $\phi_{g,mx,o}$ are the air-vapor mixture relative humidities at the humidifier and mixer outlets, respectively, $p_{g,hm,o}$ and $p_{g,mx,o}$ are the humidifier and mixer outlet total pressures (Pa), and $p^{sat}_{g,hm,o}$ and $p^{sat}_{g,mx,o}$ are the water vapor saturation pressures evaluated at the temperature of the air-vapor mixture leaving the humidifier and mixer (Pa). Note, the water vapor saturation pressure is a function of temperature, as shown in Equation 2.6. The humidifier and mixer gas outlet temperatures, $T_{g,hm,o}$ and $T_{g,mx,o}$ enter the equation through this functional relationship of the saturation pressure on temperature.

Applying the conservation of air mass to the mixer, assuming the air mass flow rate entering the mixer from the humidifier, $W_{a,hm,i}$, and the bypass, $W_{a,bp,i}$, is equal to that leaving the mixer, results in W_a=$W_{a,hm,i}$+$W_{a,bp,i}$, where W_a=$W_{a,mx,o}$. By substituting this expression for the total air mass flow rate into Equation 3.19, then defining the bypass and humidifier air mass flow ratios,

$$r_{bp} = \frac{W_{a,bp,i}}{W_a} \quad and \quad r_{hm} = \frac{W_{a,hm,i}}{W_a} \ , \tag{3.20}$$

as the fraction of the total air mass flow through the bypass and humidifier respectively, Equation 3.19 can be rearranged to solve for the relative humidity of the mixer outlet gas, resulting in

$$\phi_{g,mx,o} = \phi_{g,hm,o} \ r_{hm} \frac{p^{sat}_{g,hm,o}}{p^{sat}_{g,mx,o}} \left(\frac{p_{g,mx,o}}{p_{g,hm,o} - r_{bp} \ \phi_{g,hm,o} \ p^{sat}_{g,hm,o}} \right) \ . \tag{3.21}$$

Note, the membrane gas humidifier was designed specifically to ensure that the air-vapor mixture

leaving the humidifier is saturated, further motivating the assumption that $\phi_{g,hm,o}$=1.

This model of the mixer outlet relative humidity, in Equation 3.21, is physics based, depends only on measured variables, and does not contain parameters requiring identification. The measurement inputs to the model are the dry air mass flow rates supplied to the humidifier and bypass and the gas temperatures and total pressures at the humidifier and mixer outlets. The estimated and measured mixer outlet relative humidities were compared under a range of operating conditions, shown in Figure 3.12.

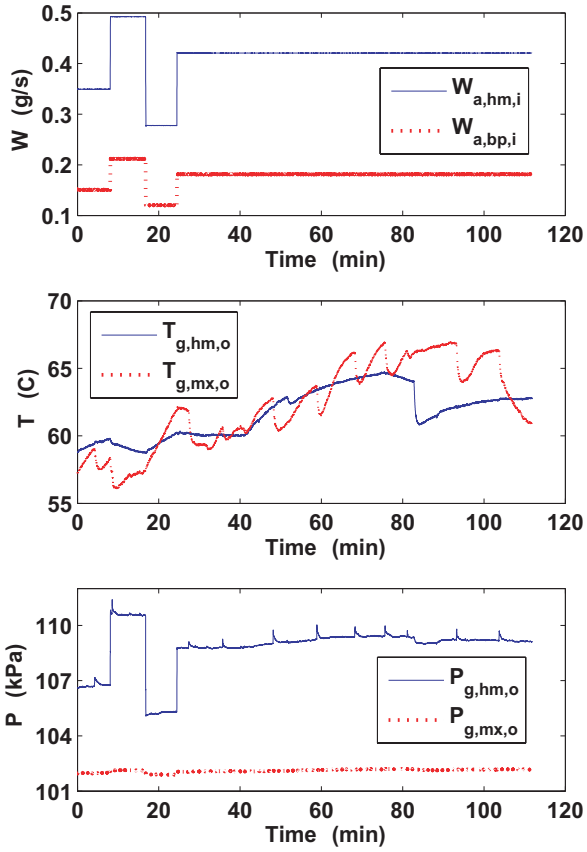

Figure 3.12: Experimental inputs to the mixer outlet relative humidity estimator. The first subplot shows the air mass flow rates supplied to the bypass and humidifier. The second subplot shows the humidifier and mixer gas outlet temperatures. Finally, the third subplot shows the humidifier and mixer gas outlet total pressures.

To examine the estimation error, the measured and estimated mixer outlet relative humidities are compared, as shown in Figure 3.13. The average estimation error was found to be 3.8% relative humidity with a standard deviation of 1.6% relative humidity, approximately two times greater than the accuracy of the relative humidity sensor. This estimation error is not symmetric about the measured value. Instead, the estimation is, on average, consistently 3.8% relative humidity less than the measurement. Although not significant, this error is predominantly due to the nearly constant bias in the measurement. This bias could result from the inaccessible temperature probe embedded in the relative humidity transducer being calibrated against a different temperature reference than that

used to calibrate the mixer and humidifier outlet temperatures. Of critical importance regardless of the bias, the relative estimator accurately captures the dynamic response throughout the experiment.

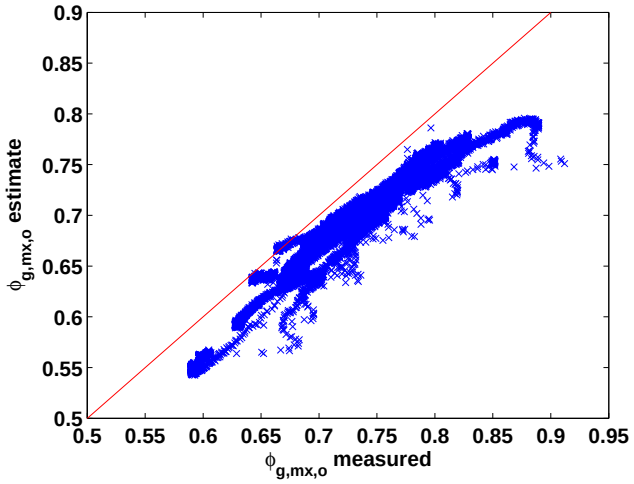

Figure 3.13: Experimental validation of the mixer outlet relative humidity estimation by comparing the measured to estimated relative humidity under the range of operating conditions shown in Figure 3.12.

Removing this bias in the measurement, by adding the 3.8% relative humidity bias to the estimation over the range of testing conditions, results in an improved estimation, as shown in Figure 3.14 for the same experiment. The average estimation error for the bias corrected relative humidity estimation was then found to be 1.2% relative humidity with a standard deviation of 1.6%, which is less than sensor accuracy.

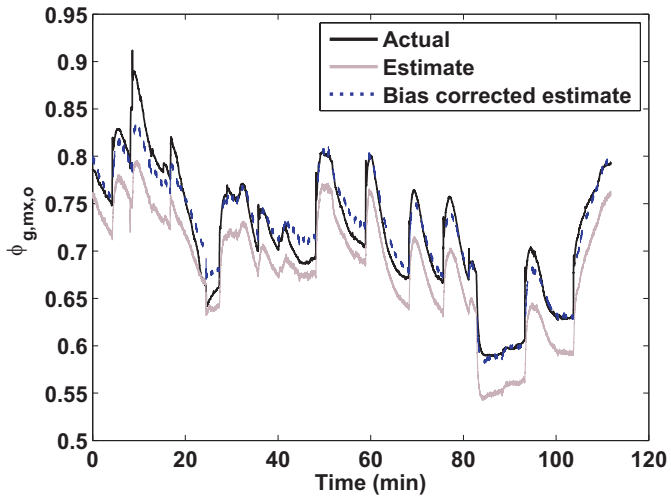

Figure 3.14: Temporal variation in the mixer outlet relative humidity estimation compared to the measurement. The solid black line indicates the measurement, the solid grey line indicates the original estimation, and the dotted blue line indicates the estimation after correcting for sensor bias.

3.3 Modeling Summary

Nine ordinary differential equations, describing the thermal dynamics of the humidifier system, have been developed and are reproduced here to summarize the modeling effort already presented.

$$
\begin{aligned}
\frac{dT_{l,r}}{dt} =& \frac{1}{m_{l,r}C_{l,r}}\left[W_{l,fc,i}C_{p,l}(T_{l,fc,o}-T_{l,r,o})+W_{l,wh,i}C_{p,l}(T_{l,hm,o}-T_{l,r,o})-\bar{h}_{l2b,r}A_{l2b,r}(T_{l,r}-T_{b,r})\right],\\
\frac{dT_{b,r}}{dt} =& \frac{1}{m_{b,r}C_{b,r}}\left[\bar{h}_{l2b,r}A_{l2b,r}(T_{l,r}-T_{b,r})-\bar{h}_{b2amb,r}A_{r}(T_{b,r}-T_{amb})\right],\\
\frac{dT_{l,wh}}{dt} =& \frac{1}{m_{l,wh}C_{l,wh}}\left[W_{l,hm,i}C_{p,l}(T_{l,r,o}-T_{l,hm,i})+\bar{h}_{b2l,wh}A_{b2l,wh}(T_{b,wh}-T_{l,wh})\right],\\
\frac{dT_{b,wh}}{dt} =& \frac{1}{m_{b,wh}C_{b,wh}}\left[Q_{wh}-\bar{h}_{b2l,wh}A_{b2l,wh}(T_{b,wh}-T_{l,wh})-\bar{h}_{b2amb,wh}A_{b2amb,wh}(T_{b,wh}-T_{amb})\right],\\
\frac{dT_{l,hm}}{dt} =& \frac{1}{m_{l,hm}C_{l,hm}}\left[W_{l,hm,i}C_{p,l}(T_{l,hm,i}-T_{l,hm,o})-W_{v,hm,o}C_{p,v}T_{g,hm,o}\right.\\
&\left.-\bar{h}_{l2g,hm}A_{l2g,hm}(T_{l,hm}-T_{g,hm})-\bar{h}_{l2amb,hm}A_{l2amb,hm}(T_{l,hm}-T_{amb})\right],\\
\frac{dT_{g,hm}}{dt} =& \frac{1}{m_{g,hm}C_{g,hm}}\left[W_{a,hm,i}C_{p,a}\left(T_{a,hm,i}-T_{g,hm,o}\right)+\bar{h}_{l2g,hm}A_{l2g,hm}(T_{l,hm}-T_{g,hm})\right],\\
\frac{dT_{a,bp}}{dt} =& \frac{1}{m_{bp}C_{bp}}\left[Q_{bp}+W_{a,bp,i}C_{p,a}(T_{a,bp,i}-T_{a,bp,o})-\bar{h}_{b2amb,bp}A_{b2amb,bp}(T_{a,bp}-T_{amb})\right],\\
\frac{dT_{g,mx}}{dt} =& \frac{1}{m_{g,mx}C_{g,mx}}\left[(W_{a,hm,i}C_{p,a}+W_{v,hm,o}C_{p,v})(T_{g,hm,o}-T_{g,mx,o})\right.\\
&\left.+W_{a,bp,i}C_{p,a}(T_{a,bp,o}-T_{g,mx,o})+\bar{h}_{b2g,mx}A_{b2g,mx}(T_{b,mx}-T_{g,mx})\right],\\
\frac{dT_{b,mx}}{dt} =& \frac{1}{m_{b,mx}C_{b,mx}}\left[Q_{mx}-\bar{h}_{b2g,mx}A_{b2g,mx}(T_{b,mx}-T_{g,mx})-\bar{h}_{b2amb,mx}A_{b2amb,mx}(T_{b,mx}-T_{amb})\right].
\end{aligned}
\tag{3.22}
$$

Again, due to the inability to measure the internal temperature states, approximations are used to relate the internal states to the measurable outlet temperatures. After applying these approximations, the measured control volume outlet conditions can be compared to the modeled estimates. These approximations are summarized by

$$
\begin{aligned}
T_{a,bp,o} =& 2T_{bp}-T_{a,bp,i},\\
T_{l,wh,o} =& 2T_{l,wh}-T_{l,r,o},\\
T_{l,hm,o} =& 2T_{l,hm}-T_{l,hm,i},\\
T_{l,r,o} =& T_{l,r},\\
T_{a,hm,o} =& 2T_{a,hm}-T_{a,hm,i},\\
T_{g,mx} =& T_{g,mx,o}.
\end{aligned}
\tag{3.23}
$$

The relative humidity of the mixer outlet gas is estimated by

$$\phi_{g,mx,o} = \phi_{g,hm,o}\, r_{hm} \frac{p^{sat}_{g,hm,o}}{p^{sat}_{g,mx,o}} \left(\frac{p_{g,mx,o}}{p_{g,hm,o} - r_{bp}\, \phi_{g,hm,o}\, p^{sat}_{g,hm,o}} \right) . \tag{3.24}$$

The locations of the measurements and disturbances are shown in Figure 3.15. The inputs to the system are heater power (Q) and the mass fraction of air diverted through the bypass (r_{bp}); the states are the respective temperatures (T); the disturbances are the total dry air mass flow rate (W_a), the air temperature supplied to the system ($T_{a,hm,i}$ and $T_{a,bp,i}$), and the ambient temperature (T_{amb}); and the system output is the air relative humidity leaving the mixer ($\phi_{g,mx,o}$).

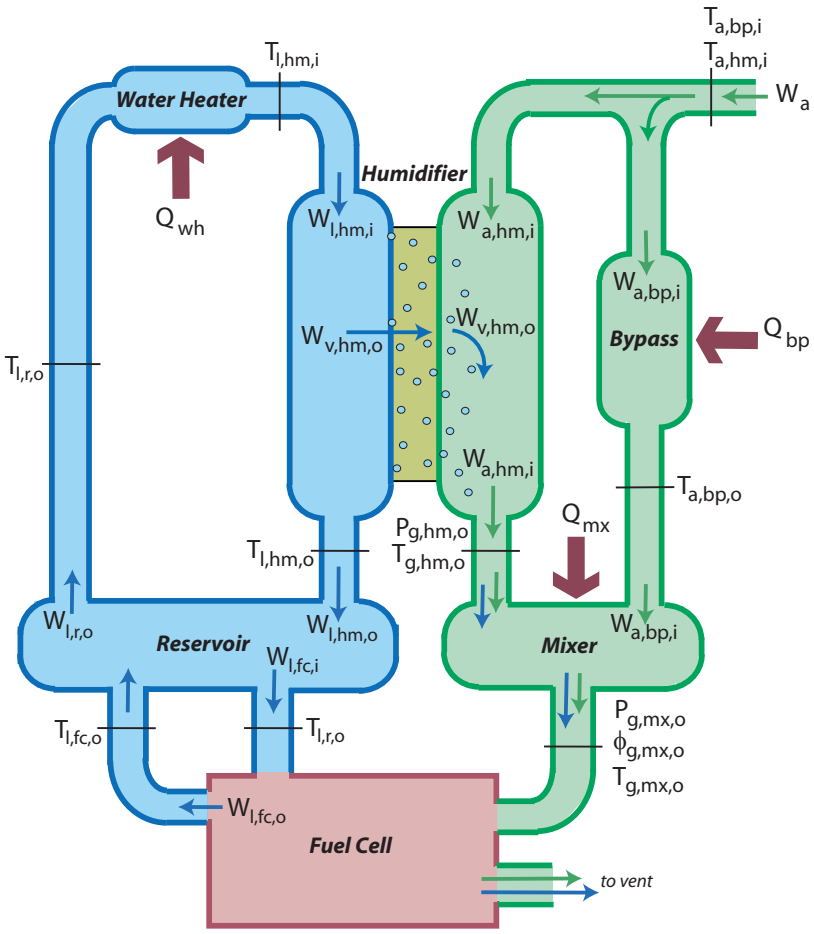

Figure 3.15: Humidifier system indicating states, disturbances and measurements

A list of the known physical model parameter values is shown in Table 3.2. These parameters were determined either from established published literature [64] or from measurements taken on the physical hardware. The constant volume specific heats were calculated as mass weighted sums of the material components within the respective control volumes. All of the parameters in the system of equations found in (3.22) are known except the heat transfer coefficients, which must be identified experimentally. Section 3.4 will present the methodology used to experimentally

determine these unknown parameter values.

Table 3.2: Calibrated model parameters based on material properties.

Mass (g)	**Specific Heat** (J/kg K)	**Area** (m^2)
m_{bp}=80	C_{bp}=460	A_{bp}=0.012
$m_{l,wh}$=50	$C_{l,wh}$=4180	$A_{b2l,wh}$=0.020
$m_{b,wh}$=780	$C_{b,wh}$=460	A_{wh}=0.028
$m_{l,hm}$=240	$C_{l,hm}$=4180	$A_{l2amb,hm}$=0.202
$m_{a,hm}$=18	$C_{a,hm}$=983	$A_{l2a,hm}$=0.03
$m_{g,mx}$=10	$C_{g,mx}$=863	$A_{b2g,mx}$=0.009
$m_{b,mx}$=745	$C_{b,mx}$=460	A_{mx}=0.012
$m_{l,r}$=2800	$C_{l,r}$=4180	$A_{l2b,r}$=0.075
$m_{b,r}$=1540	$C_{b,r}$=957	$A_{b2amb,r}$=0.087
	$C_{p,a}$=1004	
	$C_{p,v}$=1872	
	$C_{p,l}$=4180	

3.4 Parameter Identification

Prior to analyzing the system dynamics and designing controllers, the unknown heat transfer coefficients must be experimentally determined. This section details the parameter identification process and results.

3.4.1 Identification Methodology

There are two distinct methodologies which can be employed to identify the unknown heat transfer coefficients. First, the system could be held at steady-state (no temporal derivatives) and the heat transfer coefficients could be solved directly. However, the heat transfer coefficients, in some cases, are functions of mass flow rates. As a result, numerous steady-state data would be required to identify the coefficients under a wide range of operating conditions. Alternatively, a single dynamic experiment could be completed to provide a rich data set for identification, requiring model simulation.

Because the control volumes are cascaded, the control volume outlet temperature measurement is used for parameter identification of that control volume, and then can be used as a measured input for the subsequent control volume. To illustrate this more clearly, the mixer and bypass thermal

dynamics from Equation 3.22 are re-written to estimate the lumped control volume temperatures as

$$\begin{aligned}
\frac{d\hat{T}_{a,bp}}{dt} &= \frac{1}{m_{bp}C_{bp}}\left[\overline{Q}_{bp} + \overline{W}_{a,bp,i}C_{p,a}(\overline{T}_{a,bp,i} - \hat{T}_{a,bp,o}) - \overline{h}_{b2amb,bp}A_{b2amb,bp}(\hat{T}_{a,bp} - \overline{T}_{amb})\right], \\
\frac{d\hat{T}_{g,mx}}{dt} &= \frac{1}{m_{g,mx}C_{g,mx}}\left[(\overline{W}_{a,hm,i}C_{p,a} + \overline{W}_{v,hm,o}C_{p,v})(\overline{T}_{g,hm,o} - \hat{T}_{g,mx,o})\right. \\
&\quad \left. + \overline{W}_{a,bp,i}C_{p,a}(\overline{T}_{a,bp,o} - \hat{T}_{g,mx,o}) + \overline{h}_{b2g,mx}A_{b2g,mx}(\hat{T}_{b,mx} - \hat{T}_{g,mx})\right], \\
\frac{d\hat{T}_{b,mx}}{dt} &= \frac{1}{m_{b,mx}C_{b,mx}}\left[\overline{Q}_{mx} - \overline{h}_{b2g,mx}A_{b2g,mx}(\hat{T}_{b,mx} - \hat{T}_{g,mx}) - \overline{h}_{b2amb,mx}A_{b2amb,mx}(\hat{T}_{b,mx} - \overline{T}_{amb})\right],
\end{aligned} \tag{3.25}$$

where an overbar ($\bar{x}$) is used to denote measured values, and a hat ($\hat{x}$) is used for estimated quantities. For example, the mixer utilizes measured temperatures of the air supplied from the bypass, rather than model estimates. However, in tuning the bypass model, the bypass air outlet temperature is an estimate that can be compared to the measured value for parameter tuning.

The reservoir, water heater, and humidifier, make up a closed water circulation system. As a result, if the estimation of temperature anywhere in this loop is inaccurate, the error will propagate through the subsequent control volumes. For control purposes, a measurement of the water temperature in this circulation system is not necessary. As a result, it is imperative that the models of these three control volumes approximate the response to inputs and disturbances very well, otherwise a measurement of temperature somewhere in this loop would be required for compensation. To ensure that estimation errors do not propagate, first, the water circulation system was tuned by identifying the parameters associated with the humidifier and water heater independent of the other control volumes. Then, the parameters associated with the reservoir control volume were determined by including the identified humidifier and water heater model estimates. This process is detailed by indicating the measurements and estimates in the following state equations:

$$\begin{aligned}
\frac{d\hat{T}_{l,wh}}{dt} &= \frac{1}{m_{l,wh}C_{l,wh}}\left[\overline{W}_{l,hm,i}C_{p,l}(\overline{T}_{l,r,o} - \hat{T}_{l,hm,i}) + \overline{h}_{b2l,wh}A_{b2l,wh}(\hat{T}_{b,wh} - \hat{T}_{l,wh})\right], \\
\frac{d\hat{T}_{b,wh}}{dt} &= \frac{1}{m_{b,wh}C_{b,wh}}\left[\overline{Q}_{wh} - \overline{h}_{b2l,wh}A_{b2l,wh}(\hat{T}_{b,wh} - \hat{T}_{l,wh}) - \overline{h}_{b2amb,wh}A_{b2amb,wh}(\hat{T}_{b,wh} - \overline{T}_{amb})\right], \\
\frac{d\hat{T}_{l,hm}}{dt} &= \frac{1}{m_{l,hm}C_{l,hm}}\left[\overline{W}_{l,hm,i}C_{p,l}(\overline{T}_{l,hm,i} - \hat{T}_{l,hm,o}) - \hat{W}_{v,hm,o}C_{p,v}\hat{T}_{g,hm,o}\right. \\
&\quad \left. - \overline{h}_{l2g,hm}A_{l2g,hm}(\hat{T}_{l,hm} - \hat{T}_{g,hm}) - \overline{h}_{l2amb,hm}A_{l2amb,hm}(\hat{T}_{l,hm} - \overline{T}_{amb})\right], \\
\frac{d\hat{T}_{g,hm}}{dt} &= \frac{1}{m_{g,hm}C_{g,hm}}\left[\overline{W}_{a,hm,i}C_{p,a}\left(\overline{T}_{a,hm,i} - \hat{T}_{g,hm,o}\right) + \overline{h}_{l2g,hm}A_{l2g,hm}(\hat{T}_{l,hm} - \hat{T}_{g,hm})\right], \\
\frac{d\hat{T}_{l,r}}{dt} &= \frac{1}{m_{l,r}C_{l,r}}\left[\overline{W}_{l,fc,i}C_{p,l}(\overline{T}_{l,fc,o} - \hat{T}_{l,r,o}) + \overline{W}_{l,wh,i}C_{p,l}(\hat{T}_{l,hm,o} - \hat{T}_{l,r,o}) - \overline{h}_{l2b,r}A_{l2b,r}(\hat{T}_{l,r} - \hat{T}_{b,r})\right], \\
\frac{d\hat{T}_{b,r}}{dt} &= \frac{1}{m_{b,r}C_{b,r}}\left[\overline{h}_{l2b,r}A_{l2b,r}(\hat{T}_{l,r} - \hat{T}_{b,r}) - \overline{h}_{b2amb,r}A_{r}(\hat{T}_{b,r} - \overline{T}_{amb})\right].
\end{aligned} \tag{3.26}$$

The unknown parameters are tuned by comparing the measured and estimated outlet temperatures. For the bypass, mixer, water heater, and reservoir, the cost function, $J = \frac{1}{n}\sum_{i=1}^{n}|\overline{T} - \hat{T}|^2$, where n is the number of data points in the experiment, is minimized by adjusting the unknown parameter values using unconstrained nonlinear minimization. Note, the unknown heat transfer coefficients are either constant or a function of the gas or liquid mass flow rates. If all parameters were constant, linear minimization could be employed.

In tuning the humidifier as a combined two volume system, the cost function,

$$J = \frac{1}{n}\sum_{i=1}^{n}|\overline{T}_{g,hm,o} - \hat{T}_{g,hm,o}|^2 + |\overline{T}_{l,hm,o} - \hat{T}_{l,hm,o}|^2 \ ,$$

was employed, modified from the single volume cost functions described above, to simultaneously penalize the error of both the air and the water temperature estimations. Weights could be used to place more importance on the air or water temperature estimations if desired. Note, although the mixer, water heater and reservoir control volumes are also two volume systems, measurements of the bulk stainless steel temperatures are not available. As a result, these volumes are tuned using only the air/liquid water temperature estimation errors.

3.4.2 Experimental Identification Results

Two sets of experiments were conducted to identify the unknown heat transfer coefficients in the humidification system model. All experiments include multiple steps in the resistive heater power, along with steps in the total dry air mass flow supplied to the humidification system to mimic the air mass flow demand due to changes in the PEMFC electrical load. Throughout these experiments, the fuel cell system is not connected to the humidification system. Instead, a manual valve was placed downstream of the mixer to simulate the effect of the fuel cell back pressure. A summary of the identified heat transfer coefficients is presented in Table 3.3 along with the expected parameter ranges. All of the identified parameters fall within these expected ranges.

Table 3.3: Tuned humidification system model parameters based on experimental identification.

Expected Range*	**Identified Value** (W/m^2K)
$50-20000$	$\overline{h}_{b2l,wh}$=139.8 and $\overline{h}_{l2b,r}$=167.5
$50-1000$	$\overline{h}_{b2amb,wh}$=0 and $\overline{h}_{l2amb,hm}$=22.5 $\overline{h}_{b2amb,r}$=80.0
$5-250$	$\overline{h}_{bp}$=10.8-21822$W_{a,bp,i}$
$5-25$	$\overline{h}_{b2amb,mx}$=25.8
$25-250$	$\overline{h}_{b2g,mx}$=2819$W_a^{0.54}$
$25-20000$	$\overline{h}_{l2a,hm}$=41029$W_{a,hm,i}^{0.95}$

*Expected ranges taken from [64] for natural and forced convection of liquids and gases.

The linear model for the bypass heat transfer coefficient was identified and found to be $\overline{h}_{bp}$=10.8-21822$\overline{W}_{a,bp,i}$ W/m^{2}K. The experimental inputs to the bypass, along with the comparison of the

modeled and measured bypass air outlet temperatures, are shown in Figure 3.16. Over this experiment, the maximum and average estimation errors were 1.2^{o}C and 0.5^{o}C, respectively, with a standard deviation of 0.3^{o}C. Throughout the experiment, both the dynamic and steady-state responses are well captured. Interestingly, the dynamic response time to changes in the air mass flow rate or the bypass heater exhibit similar time constants. These time constants will be further examined in Chapter 4.

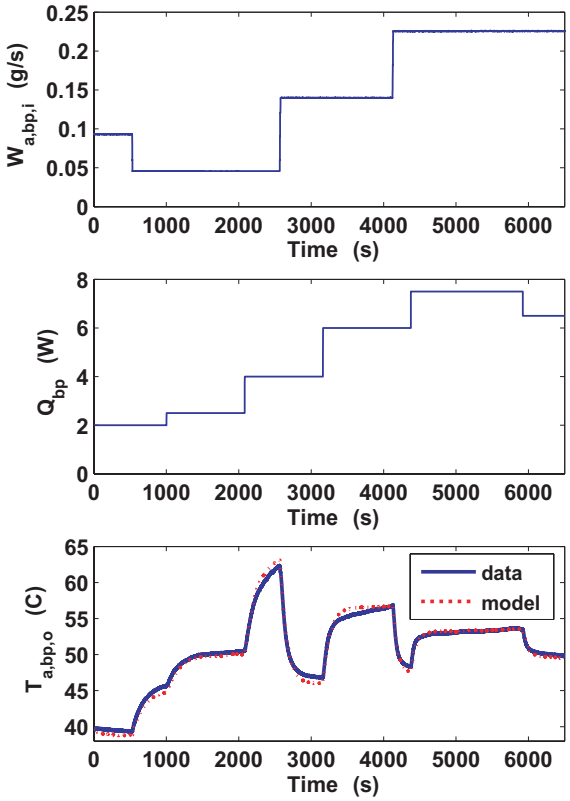

Figure 3.16: Bypass experimental parameter identification results. The subplots detail the air mass flow rate through the bypass, the bypass resistive heater power, and compare the modeled and measured air outlet temperatures.

The identified natural convection heat transfer coefficient from the mixer bulk to the ambient was $\bar{h}_{b2amb,mx}$=25.8 W/m^{2}K and the forced convection heat transfer coefficient from the mixer bulk to the air-vapor mixture was $\bar{h}_{b2g,mx}$=2819$\bar{\dot{m}}_a^{0.54}$ W/m^{2}K. The experimental inputs to the mixer are shown, along with the modeled and measured mixer air outlet temperatures, in Figure 3.17. Over this experiment, the maximum and average estimation errors were found to be 3.5^{o}C and 0.5^{o}C with a standard deviation of 0.6^{o}C. It is important to note that the dynamics that occur between 3000 to 4000 seconds are not due to changes in the inputs or disturbances to the mixer and are not reproducible. These dynamics are thought to be due to localized condensation/evaporation dynamics. However, the model provides an accurate average estimation during this period.

For the reservoir, water heater and humidifier control volumes, a separate experiment was conducted without operating the mixer or the bypass. Upon identifying the heat transfer coefficients for

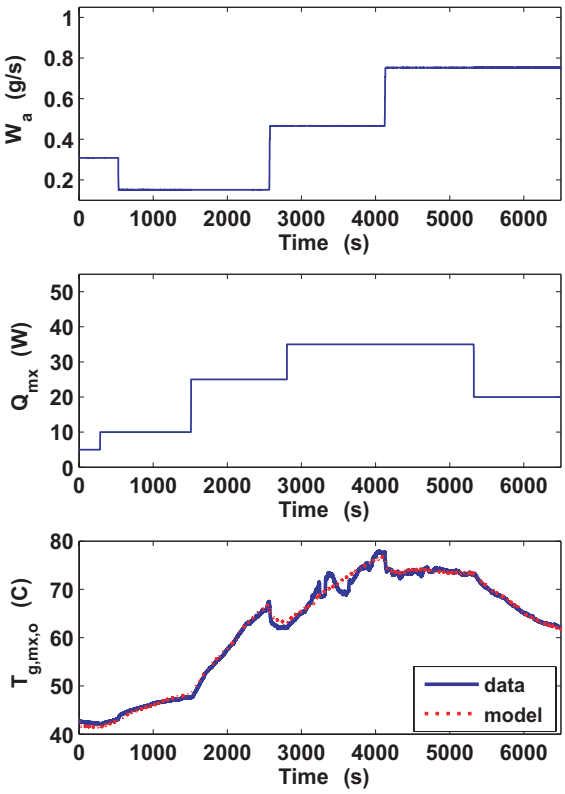

Figure 3.17: Mixer experimental parameter identification results. The subplots detail the total air mass flow rate through the mixer, the mixer resistive heater power, and compare the measured and estimated gas outlet temperatures.

the individual water heater and the humidifier control volumes using measured temperature inputs, the entire closed water circulation system model was simulated to tune the reservoir parameters, as described in Section 3.4.1. As expected, the estimations for each control volume degrade when the estimation errors are allowed to propagate through the closed water circulation system. As a result, these closed circulation system estimations will be presented here, rather than the better estimations found for the individual control volumes.

The identified natural convection heat transfer coefficient from the reservoir bulk to the ambient was $\bar{h}_{b2amb,r}$=80 W/m^{2}K and the forced convection heat transfer coefficient from the reservoir bulk to the liquid water was $\bar{h}_{b2l,r}$=167 W/m^{2}K. The maximum and average estimation errors were found to be 1.7^{o}C and 0.6^{o}C, with a standard deviation of 0.4^{o}C. Throughout the experiment, the dynamic response of the liquid water temperature leaving the reservoir is well captured as shown in Figure 3.18. Although the steady-state temperature is reasonably predicted, typically the temperature estimate is too high when the system is warming up and too low when the system is cooling down.

For the water heater, the identified heat transfer coefficients for natural convection between the control volume bulk and the ambient was found to be $\bar{h}_{b2amb,wh}$=0 W/m^{2}K and for forced convection between the bulk and the liquid water was found to be $\bar{h}_{b2l,wh}$=139.8 W/m^{2}K. It is important to note

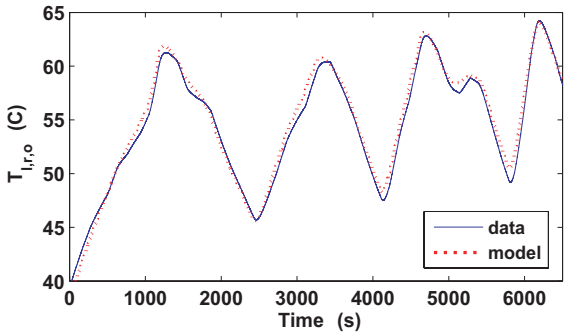

Figure 3.18: Reservoir experimental parameter identification results comparing the measured and estimated liquid water outlet temperatures.

that the identified heat transfer to the ambient indicates that the water heater system could be treated as adiabatic. Figure 3.19 compares the estimated and measured liquid water temperatures leaving the water heater for the closed water circulation system model, implying estimates of the reservoir influence the water heater estimations and then subsequently the humidifier estimation. The maximum and average estimation errors were 2.0^{o}C and 0.6^{o}C, with a standard deviation of 0.4^{o}C. Both steady-state and dynamic response of the liquid water in the water heater are well approximated throughout the experiment.

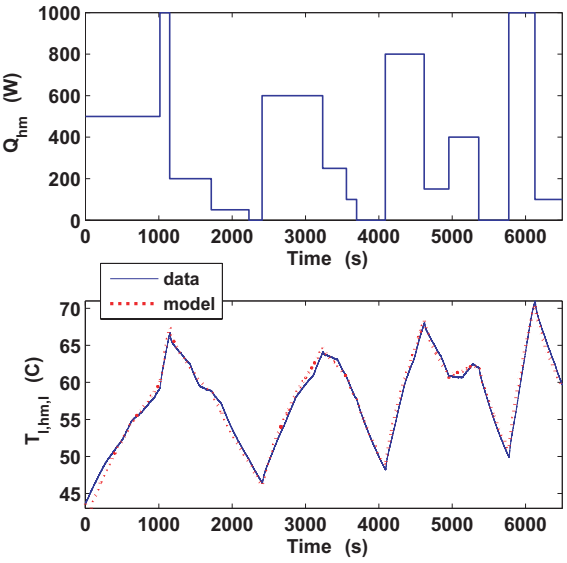

Figure 3.19: Experimental parameter identification results for the water heater control volume. The first subplot shows the amount of heat supplied by the water heat. The second subplot compares the modeled and measured liquid water temperature leaving the water heater and entering the humidifier.

The identified constant heat transfer coefficient from the humidifier liquid water to the ambient was found to be $\bar{h}_{l2amb,hm}$=22.5 W/m^{2}K. The variable convective heat transfer coefficient from the liquid water to the air through the membrane was found to be $\bar{h}_{l2a,hm}$=41029$W_{a,hm,i}^{0.95}$ W/m^{2}K. Fig-

ure 3.20 compares the estimated and actual air and liquid water outlet temperatures for this closed water circulation system model. The maximum and average humidifier estimation errors for this experiment were 2.1^{o}C and 0.6^{o}C for the liquid water and 2.6^{o}C and 1.1^{o}C for the air. The standard deviation in the estimation error for the liquid and air were both 0.5^{o}C.

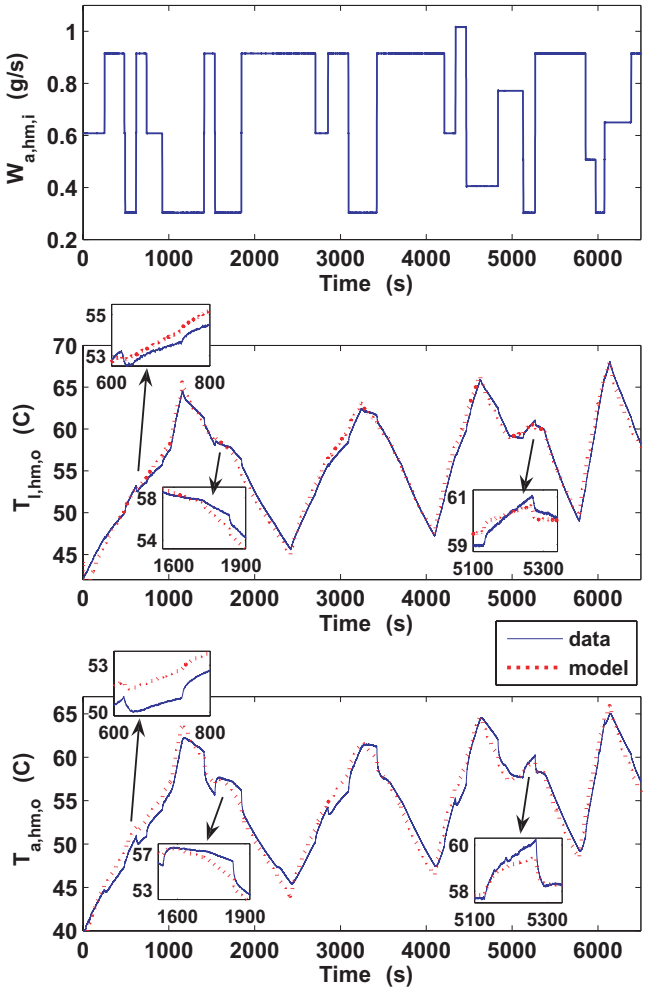

Figure 3.20: Experimental parameter identification results for the humidifier control volume including both the air and liquid water states. The first subplot indicates the air mass flow rate through the humidifier. The second and third subplots compare the modeled and measured humidifier liquid water and air outlet temperatures, respectively.

Of greatest concern for controller development, the dynamic responses of both the humidifier air and liquid water are well captured throughout the experiment. However, there is an increased offset in the humidifier air outlet temperature estimation when the system is cooling as compared to when the system is warming up. What is interesting to note, an increase in the air mass flow rate typically causes a decrease in the air outlet temperature, requiring more energy to heat the added air demand, in turn lowering the liquid water temperature. These relationships are seen in the model and confirmed by the experiment.

3.5 Model Validation Results

For validating the model, all of the control volumes were combined such that the estimation of the temperature leaving one control volume is treated as an input to subsequent control volumes, as shown in Figure 3.21. An experiment, different than that used for parameter identification, was conducted for validating the model. This experiment included steps in the air mass flow rate as well as the heaters.

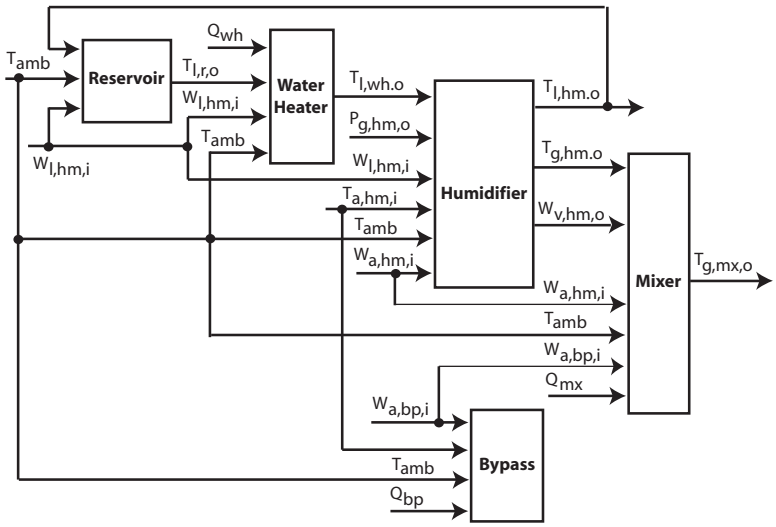

Figure 3.21: Model structure for open loop simulation of the gas humidification system.

The estimated bypass air outlet temperature is compared with the measurement in Figure 3.22. For changes in the air mass flow rate and the bypass heater, the model captures the response time. However, there is an offset in the steady-state temperature estimation throughout most of the experiment, due to an overestimation of the heat loss from the control volume to the ambient. Although the estimation error appears to be increasing throughout the experiment, it is very sensitive to the selection of heat transfer coefficients. Linearization of the bypass state equation, which will be discussed in more detailed in Chapter 4, has shown that the bypass pole location is most sensitive to air flow, and not the heat transfer coefficient. As a result, this steady-state error will have little impact on the resulting controller design. Additionally, this estimation offset has little impact on the gas mixer temperature estimation due to the relatively small fraction of air flowing through the bypass as compared to the humidifier. The average estimation error was 2.8^oC with a standard deviation of 1.4^oC.

The estimated water reservoir outlet temperature is compared with the measurement in Figure 3.23. The reservoir system is driven by the estimate of the liquid water temperature leaving the humidifier and represents a significant thermal lag in the water circulation system due to the relatively large stored water mass. The reservoir model captures both the slow response following the humidifier dynamics as well as the steady-state temperature. The average estimation error was 0.3^oC with a standard deviation of 0.3^oC.

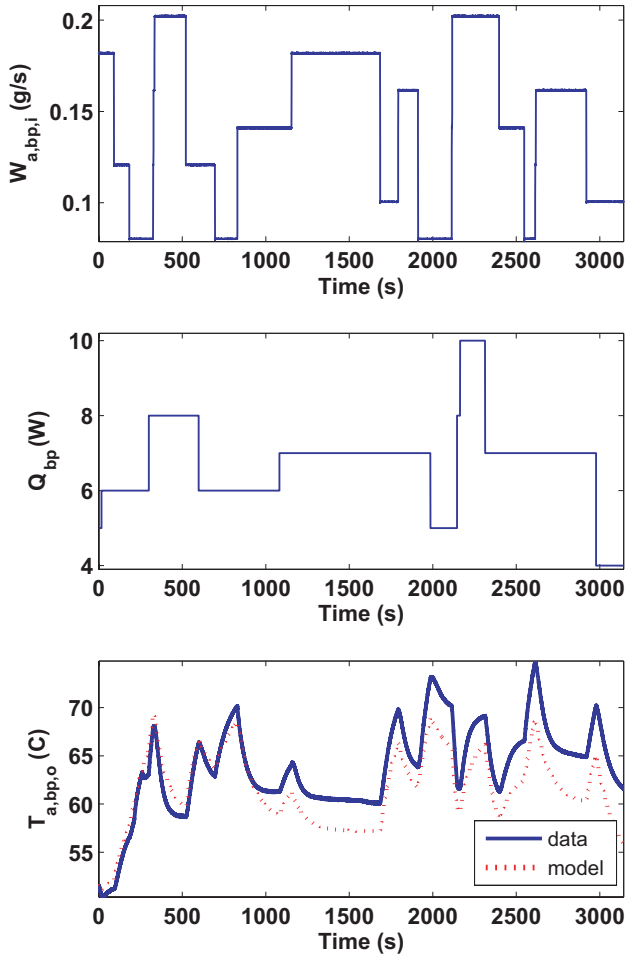

Figure 3.22: Bypass experimental validation results. Given the measured air mass flow rate and temperature of the air supplied to the bypass, the air outlet temperature is estimated and compared with measurements.

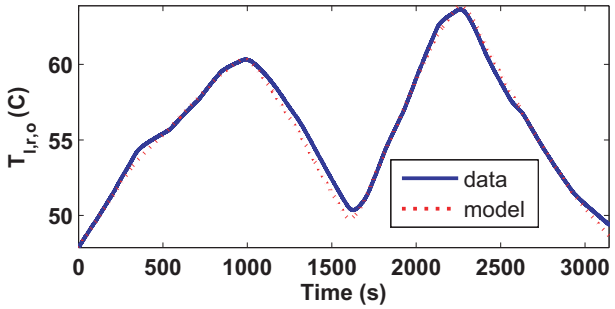

Figure 3.23: Reservoir experimental validation results. Given the measured liquid water mass flow rate and the estimated liquid water temperature supplied to the reservoir, the liquid water outlet temperature is estimated.

The estimated water heater outlet temperature is compared with the measurement in Figure 3.24. The water heater model captures the slow response due to changes in the heater as well as the steady-state temperature. The average estimation error was 0.5^{o}C with a standard deviation of 0.4^{o}C.

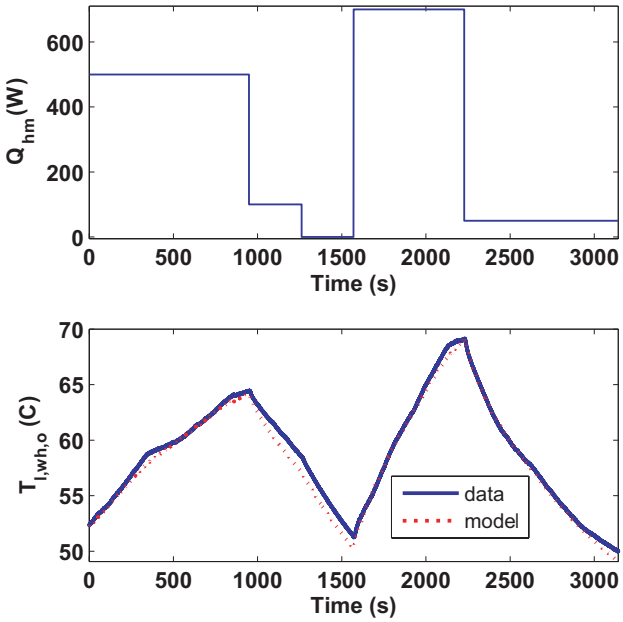

Figure 3.24: Water heater experimental validation results. Given the measured liquid water mass flow rate supplied and the estimated inlet temperature, the liquid water outlet temperature is estimated.

The estimated air and liquid water temperatures leaving the humidifier are compared with the measurements in Figure 3.25. The humidifier air outlet temperature estimation has a steady-state offset when the system is cooling down (from approximately 1000-1500 seconds and 2300-3000 seconds). This offset is thought to be the result of neglecting the condensation or evaporation of water on the air side of the humidifier. A more complex model of the humidifier may correct this. However, the steady-state air temperature is well approximated during warm-up and captures the correct dynamics response through the experiment. Both the steady-state and dynamic response of the liquid water is well approximated. Considering the complexity of the physical humidifier system, and the modeling assumptions made, this model adequately captures the humidifier thermal response. The average estimation errors were 1.3^{o}C and 0.7^{o}C with standard deviations of 1.1^{o}C and 0.5^{o}C, for the air and liquid water respectively.

The estimated mixer air outlet temperature is compared with the measurement in Figure 3.26. Although the model does not predict the exact steady-state temperature, the response to changes in air mass flow rate or mixer heat are well captured. An improvement on the humidifier estimation during the cool down portion of the experiment may improve these results. Note, at approximately 1000 seconds, the measured mixer outlet temperature momentarily decreases dramatically. The cause of this rapid decrease and then increase in temperature is unknown, but is thought to be re-

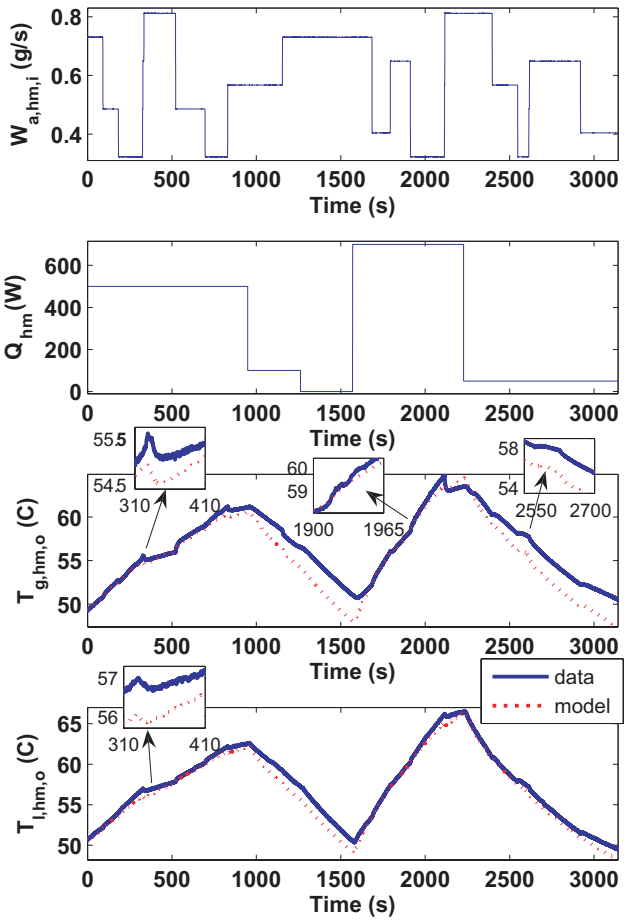

Figure 3.25: Humidifier experimental validation results. Given the measured air and liquid water mass flow rates supplied, the estimated liquid water inlet temperature and the measured air inlet temperature, the air and liquid water outlet temperatures are estimated.

lated to unmodeled condensation and evaporation dynamics on the walls of the stainless steel tubing. The average estimation error was 0.8^{o}C with a standard deviation of 0.5^{o}C.

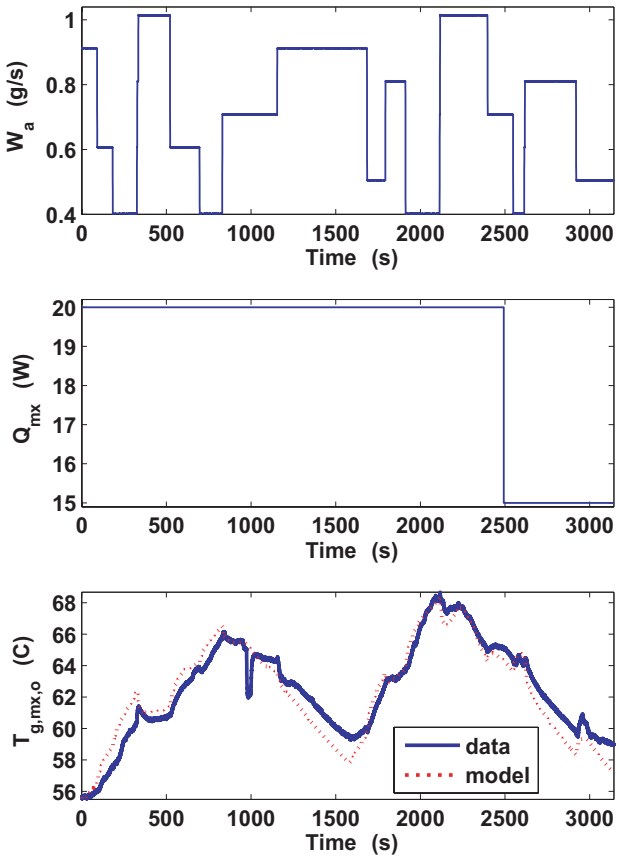

Figure 3.26: Mixer experimental validation results. Given the measured air mass flow rate and estimated bypass and humidifier air outlet temperatures supplied to the mixer, the mixer air outlet temperature is estimated.

Chapter 4

Humidification System Control

With the model of the external humidifier system thermal dynamics, summarized in Equation 3.22 and experimentally validated in Section 3.5, controllers were designed and tuned to coordinate the three resistive heaters as well as the mass fractional split of air flow between the humidifier and the air bypass. These controllers must regulate the temperature of the dry air leaving the bypass and joining the saturated air leaving the humidifier. Should the temperatures of these two gas streams not be well regulated, condensation or dehydration will occur. As a result, the three heaters must be well coordinated to regulate the system temperatures and mitigate the effect of disturbances.

Figure 4.1 provides an overview of the control architecture employed. An error signal is calculated (difference between the reference and actual temperatures) as an input to the heater controllers. The heaters are then controlled by determining a desired heater power for the respective control volumes given the error signal. The fractional split of dry air mass flow between the humidifier and the bypass is commanded using a static nonlinear feedforward map given a desired relative humidity and temperature at the cathode inlet (mixer outlet).

This chapter introduces the feedforward mapping for controlling air flow; the reference temperatures used to regulate the system; the system linearization in preparation for controller development; the controller selection and tuning; the hardware implementation of the closed loop humidification system; and finally, the closed loop performance of the humidifier system under a variety of operating conditions.

4.1 Nonlinear Feedforward for Air Mass Flow Control

A nonlinear, physics based, feedforward mapping is used to control the amount of air supplied to the bypass and the humidifier to achieve the desired relatively humidity of the gases leaving the mixer and supplied to the cathode inlet of the PEMFC stack. Direct feedback control of the mixer outlet relative humidity would require either a water vapor mass flow rate or relative humidity measurement at the mixer outlet. In practice, both such measurements are prohibitively expensive, motivating the rationale for selecting only feedforward and neglecting feedback for relative humidity control. The nonlinear feedforward mapping used for air mass flow control is a function of

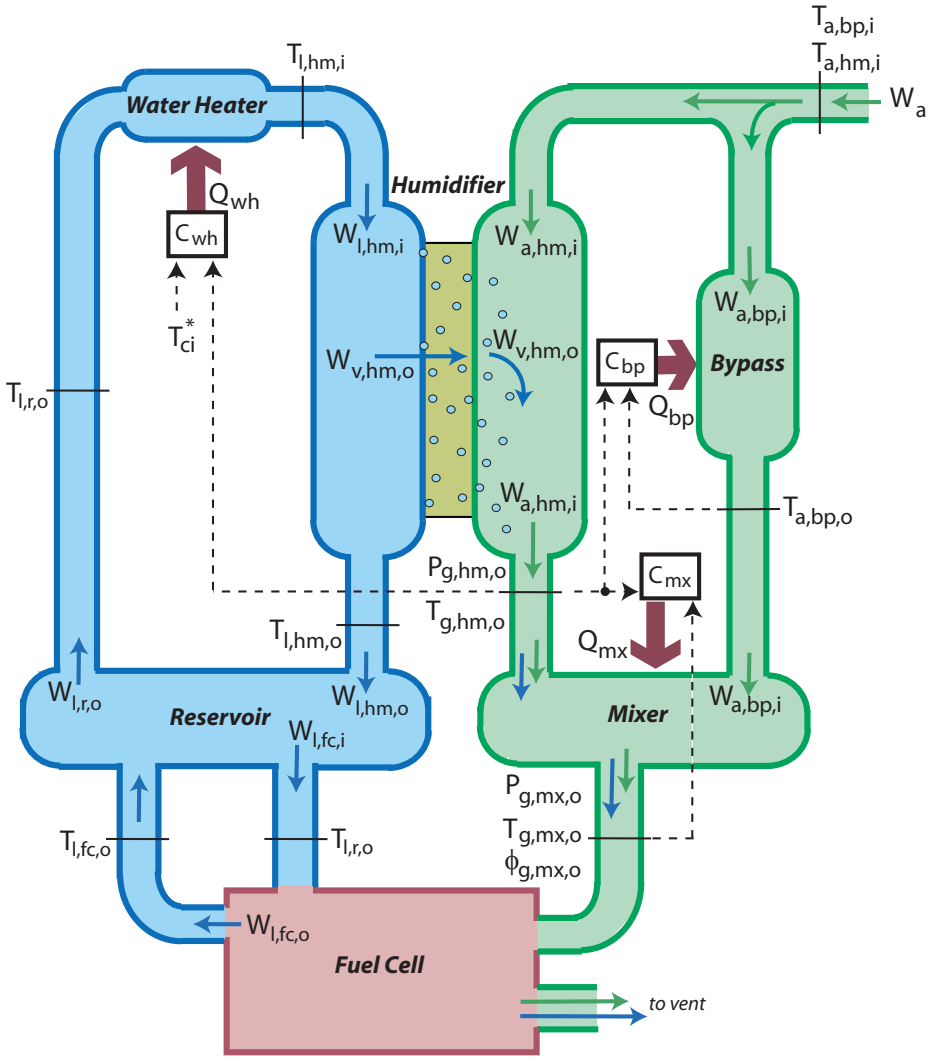

Figure 4.1: Schematic of the humidification system control architecture indicating the locations of the temperature references with respect to the states. The dashed lines indicate the reference and feedback temperatures that are treated as controller inputs. The controllers are denoted here with a C and a subscript indicating the applicable control volume.

both the measured and desired temperature states, relative humidity estimations, as well as total gas pressure measurements.

To calculate the desired split of dry air mass flow between the humidifier and the bypass, mass conservation is applied. Assuming that in steady-state the mass flow rate of water vapor leaving the humidifier, $W_{v,hm,o}$, is equal to the mass flow rate of vapor leaving the mixer, $W_{v,mx,o}$, and applying the definition for the humidity ratio, $\omega = \frac{M_v \phi p^{sat}}{M_a(p-\phi p^{sat})}$, the required mass flow fraction of air through the humidifier, $r_h = W_{a,hm,i}/W_a$, can be rewritten as

$$r_{hm} = \frac{\phi^*_{g,mx,o} p^{sat*}_{g,mx,o}(p_{g,hm,o} - \phi_{g,hm,o} p^{sat}_{g,hm,o})}{\phi_{g,hm,o} p^{sat}_{g,hm,o}(p_{g,mx,o} - \phi^*_{g,mx,o} p^{sat*}_{g,mx,o})}, \tag{4.1}$$

where a superscript $*$ has been used to denote desired reference values. Note, this analysis employs the same assumptions and a similar methodology as that used to estimate the mixer outlet relative humidity in Section 3.2.8.

As stated previously, it is assumed that there is no change in air mass stored in the control volumes and that the air mass flow rate is controlled instantaneously. Therefore, the commanded air mass flow rates through the humidifier and the bypass are:

$$\begin{aligned} W_{a,hm,i} &= r_{hm} W_a, \\ W_{a,bp,i} &= W_a - W_{a,hm,i}. \end{aligned} \tag{4.2}$$

4.2 Reference Temperatures

To properly coordinate the heaters using feedback control, reference (desired) temperatures must be established for the mixer, bypass and humidifier air outlets. The error, or difference between the reference and actual temperatures,

$$\delta e = \delta T^* - \delta T \ , \tag{4.3}$$

where δ indicates a deviation from nominal conditions and the asterisk $*$ is used to denote a reference value, can then be formulated into control objectives for each of the heaters. It is important to note that these actual temperatures must be measured, or accurately estimated using an observer and other measurements, in order to implement feedback control.

A number of possible reference temperature choices exist for thermal regulation of the humidification system, depending upon the response time of each closed loop system. Should the air supplied to the mixer through the air bypass be colder than the air leaving the humidifier, condensation will result. On the other hand, if the air leaving the bypass is hotter than the air leaving the humidifier, the desired relative humidity can not be achieved. Additionally, if the desired cathode inlet temperature can be achieved by the mixer relatively quickly compared to the water circulation system, the feedforward control of air flow supplied to the humidifier will further impact temperature regulation.

These reference temperature selections have drastically different implications with respect to controller performance. For example, if the water circulation system, bypass and mixer had similar response times, they could be independently coordinated which would motivate the selection of the desired cathode inlet temperature as the reference temperature for all three. However, to regulate the humidifier air outlet temperature, the inline water heater supplies heat to the liquid water prior to entering the humidifier. It will be shown later, in Section 4.3, that this intermediate step of heating liquid water to raise the humidifier gas temperature results in the slowest thermal response of the three closed loop control systems. If the mixer and bypass are capable of achieving this reference temperature much sooner than the water circulation system, undesirable condensation or evaporation dynamics will result depending upon whether temperature is stepped up or down.

Based on this difference in closed loop time constants, different reference temperatures were selected to control each heater based on an understanding of the system dynamics (further motivating the need for the accurate model presented in Chapter 3). Because both the mixer and bypass systems are faster than the water circulation system, condensation or evaporation can be avoided if both the mixer and the bypass track the temperature dynamics of the water circulation system. Choosing the reference values such that the water circulation system tracks the desired cathode inlet temperature and the mixer and bypass track the water circulation system,

$$T^*_{g,mx,o} = T_{g,hm,o} \ , \tag{4.4a}$$

$$T^*_{g,hm,o} = T^*_{ca,i} \ , \tag{4.4b}$$

$$T^*_{a,bp,o} = T_{g,hm,o} \ , \tag{4.4c}$$

results in a decreased system thermal time constant but will maintain the desired relative humidity. Figure 4.1 shows the location of these reference temperatures with the measured states and respective control volumes clearly indicated. An important distinction is made here, the reference temperature for the water circulation system will be either constant or variable depending upon the water management demands of the PEMFC stack. Both the mixer and bypass reference temperatures are also variable, but depend on the dynamics in the water circulation system.

If the desired cathode inlet temperature were deemed to be more critical to maintain than relative humidity, the mixer reference temperature could be selected as the desired cathode inlet temperature, implying that the mixer heater is controlled irrespective of the bypass and water circulation system conditions. This control strategy relies on the significant bandwidth separation observed between the slow closed loop water circulation system and the fast bypass and mixer systems and should be reconsidered if the volumes were designed to be significantly different than those presented in this work.

4.3 Plant Linearization

Due to the cascaded nature of the humidification system, the mixer and bypass control volumes can be analyzed separately from the water circulation system, allowing for independent controller design. The system of ordinary differential equations, shown in Equations 3.22-3.23, was expressed analytically in state space where the control volume outlet temperatures represented the states, the heater actuators represented the system inputs, the air mass flow rate represented the system disturbance, and the liquid water mass flow rate and ambient temperature were assumed to be constant.

Using this state space representation, the system was linearized about a set of nominal conditions, listed in Table 4.1. It is important to note that for the mixer control volume, the bypass and humidifier air outlet temperatures are assumed to be perfectly controlled (constant). For the selection of the total air mass flow rate, the PEMFC stack operating conditions must be considered. As previously discussed, the humidification system was designed to regulate the cathode gas

stream supplied to an 8-cell PEMFC stack with an active area of 300cm^2. Applying a 0.3A/cm^2 electric load to this PEMFC stack, slightly more than half the expected maximum current density, requires 0.6 g/s of air at an air stoichiometry of 250%. These nominal conditions were selected to approximate the midpoint of the expected operation range.

Table 4.1: Nominal conditions used for system linearization.

Variable	**Nominal Value**
W_a^o	0.6 g/s
r_h^o	0.7
$T_{a,hm,i}^o$=$T_{a,bp,i}^o$	20^{o}C
$W_{l,hm,i}^o$	30 g/s
T_{amb}^o	27^{o}C
$p_{g,hm,o}^o$	102.57 kPa abs
$T_{a,bp,o}^o$=$T_{g,hm,o}^o$	55^{o}C

Transfer functions from the resistive heater inputs to the system outlet temperatures were then derived and the sensitivity of the pole locations to disturbances in the total air mass flow rate was examined. Table 4.2 provides a summary of the open loop time constants and DC-gains at different total air mass flow rates for each of the three systems. The total air mass flow rate range considered, W_a=0.3-0.9 g/s, represents the disturbance to the humidification system for PEMFC stack electrical loads varying from 0.15-0.45A/cm^2. The linear and nonlinear systems were then compared, both to steps in heater inputs and air mass flow rates, indicating that the linear system response well approximates the nonlinear system for small deviations from these nominal conditions.

Table 4.2: Open loop response time and DC-gain for the bypass, mixer and water circulation systems as total air mass flow rate is varied from 0.3-0.9 g/s.

System	**DC-gain** (^{o}C/W) $\frac{\delta T_{g,cv,o}}{\delta Q_{cv}}\big\vert_{s=0}$	**Time Constant (sec)**
Water Circulation	0.10-0.08	123-59
Bypass	6.93-3.32	1490-1195
Mixer	1.01-0.52	714-498

Transfer functions can also be expressed from the air flow disturbance to the outlet temperatures. However, the DC gains of these transfer functions indicate that there is a very small change in the steady-state heat required for a change in air mass flow rate. As a result, the use of static feedforward to reject air flow disturbances does not significantly improve temperature regulation. Therefore, only transfer functions from the heater inputs to the temperature outputs will be presented here.

4.3.1 Bypass Linearization

The first order analytical transfer function from the bypass heater input to the bypass air outlet temperature, assuming the dry air mass flow rate is constant, is expressed as

$$\frac{\delta T_{a,bp,o}}{\delta Q_{bp}} = \frac{b_{o,bp}}{s + p_{bp}} \,, \tag{4.5}$$

where the numerator coefficient and bypass pole location are defined by

$$b_{o,bp} = \frac{2}{m_{bp} C_{bp}} \,,$$
$$p_{bp} = \frac{2W^{o}_{a,bp,i} C_{p,a} + \bar{h}^{o}_{b2amb,bp} A_{b2amb,bp}}{m_{bp} C_{bp}} \,.$$

Note, the experimentally identified bypass heat transfer coefficient, $\bar{h}^{o}_{b2amb,bp}$ from Table 3.3, is evaluated at the nominal bypass air mass flow rate.

The bypass pole location (denoted by p_{bp}) is a function of the air mass flow rate through the bypass which will influence the system response time. For the nominal bypass air mass flow rate of $W_{a,bp,i}$=0.18 g/s (equivalent to the conditions of r_{hm}=0.7 at W_a=0.6 g/s), the bypass pole location was found to be $p_{bp} \approx$0.013, which results in an open loop time constant of approximately 80 seconds. By varying the nominal air mass flow rate through the bypass from $W_{a,bp,i}$=0.09-0.27 g/s, the bypass pole location varies from $p_{bp} \approx$0.008-0.017 which corresponds to a range of open loop time constants between 123-59 seconds, respectively. In summary, as the air mass flow rate increases, the bypass system response time increases.

The DC-gain, found by evaluating $\frac{\delta T_{a,bp,o}}{\delta Q_{bp}}|_{s=0}$, is also influenced by the air mass flow rate through the bypass. As air flow increases, the bypass pole location increases, causing the DC gain to decrease. Qualitatively, a step in heat added to the bypass will increase the system temperature by a smaller amount at high air flow as compared to low air flow; or alternatively, more energy is required to maintain the system temperature as air flow increases.

4.3.2 Water Circulation System Linearization

With the state space representation of the humidifier water circulation system thermal dynamics, a transfer function can be expressed from the water heater actuator input to the humidifier air outlet temperature. This transfer function is expressed as

$$\frac{\delta T_{g,hm,o}}{\delta Q_{hm}} = \frac{b_o (s + z_1)(s + z_2)}{(s + p_{l,wh})(s + p_{l,hm})(s + p_{a,hm})(s + p_{l,r})(s + p_{b,r})(s + p_{b,wh})} \,, \tag{4.6}$$

where the coefficient in the numerator, b_o, and the pole and zero locations can be analytically represented as functions of the heat transfer coefficients and the control volume masses and specific heats. At the nominal conditions, b_o=3.38x10^{-6} and the poles and zero are located at $p_{a,hm}$=1.23, $p_{l,hm}$=0.292, $p_{l,r}$=0.090, $p_{b,r}$=8.2x10^{-4}, $p_{l,wh}$=0.014, $p_{b,wh}$=0.016, z_1=0.016, and z_2=0.0094. With

the assumption that the constituent temperature distribution from the inlet to the outlet is linear and the inlet temperature is not constant (as is the case for the humidifier and water heater but not the air bypass), a zero results that is associated with that control volume constituent. For these nominal conditions there is a pole-zero cancelation between z_1=$p_{b,wh}$=0.016, resulting in a fifth order closed loop transfer function with a relative degree of four. The fastest control volume response time (pole location furthest from the origin on the complex s-plane) is the humidifier air, followed by the liquid water volumes, with the bulk volumes having the slowest response time.

By varying the nominal air mass flow rate through the humidifier from $W_{a,hm,i}$=0.21-0.63 g/s, the open loop time constant decreases from 1490-1195 seconds, respectively. Thus, as with the bypass, the water circulation system response time increases for increasing air mass flow rates. This change in the time constants is most influenced by the slowest pole, which varies from a location on the real axis of the complex s-plane at s=-0.0007 to s=-0.0009 across this range of humidifier air mass flow rates. Note, although the pole locations are significantly influenced by the liquid water mass flow rate, this variable is not a disturbance to the system and can be regulated at a fixed value throughout the experiments. As a result, the sensitivity of the pole locations to liquid water flow is not considered here.

4.3.3 Mixer Linearization

The mixer thermal dynamics are described by a two state system including the air-vapor mixture and the bulk materials. With the state space representation of the mixer thermal dynamics, the time constants of these two states were compared. At the nominal conditions, the pole location associated with the gas state is located at s=-0.132 while the pole associated with the bulk materials is located at s=-0.0017, indicating a significant bandwidth separation between these two states. As a result, assuming that $\frac{\delta T_{g,mx,o}}{dt}$=0, a first order analytical transfer function from the mixer heater input to the gas outlet temperature, is expressed by

$$\frac{\delta T_{g,mx,o}}{\delta Q_{mx}} = \frac{b_{o,mx}}{s + p_{mx}} \ , \tag{4.7}$$

where,

$$b_{o,mx} = \frac{\bar{h}^{o}_{b2g,mx} A_{b2g,mx}}{m_{b,mx} C_{b,mx} \left(\alpha_{o,mx} + \bar{h}^{o}_{b2g,mx} A_{b2g,mx}\right)} \ ,$$

$$p_{mx} = \frac{(\bar{h}_{b2amb,mx} A_{b2amb,mx} + \bar{h}^{o}_{b2g,mx} A_{b2g,mx})\alpha_{o,mx} + \bar{h}_{b2amb,mx} A_{b2amb,mx} \bar{h}^{o}_{b2g,mx} A_{b2g,mx}}{m_{b,mx} C_{b,mx} \left(\alpha_{o,mx} + \bar{h}^{o}_{b2g,mx} A_{b2g,mx}\right)} \ ,$$

$$\alpha_{o,mx} = \left(W^{o}_{a} C_{p,a} + W^{o}_{v,hm,o} C_{p,v}\right) \ .$$

Comparing the nonlinear full order model to this linear reduced order model of the mixer thermal dynamics during step changes in mixer heat shows an insignificant difference between the two dynamic models.

Clearly, the mixer pole location is a function of the air mass flow rate, either directly, or indirectly through the heat transfer coefficient (between the bulk materials and the gases) or the water vapor mass flow rate. By varying the air mass flow rate from W_a=0.3-0.9 g/s, the pole location moves from s=-0.0014 to s=-0.0020, the time constant to a step in heat decreases from 714 to 498 seconds, and the DC gain decreases from 1.01 to 0.52 ^oC/W. These results indicate that increasing the air mass flow rate results in a faster response but smaller relative increase in temperature for a given step in the mixer heater.

4.4 Thermostatic Control

A simple and cheap control strategy for temperature regulation of a thermal system involves cycling a heater on or off at specified thresholds, as commonly implemented with thermostats. Thermostatic (two position or on-off) control is widely used for industrial automatic feedback systems due to its simplicity and cost effectiveness. A commonly recognized disadvantage to thermostatic control is the cycling of the actuator due to the repeated on-off action resulting from sensor noise. To reduce this cycling, hysteresis is often incorporated to construct a region about the desired value for which no control action takes place. This region is known as the differential gap [47]. Figure 4.2 relates the error signal, e, to the control input, Q, for this thermostatic controller with hysteresis. Refer back to Figure 4.1 for an illustration of the signal paths detailing the controllers and plants for the humidification feedback control system.

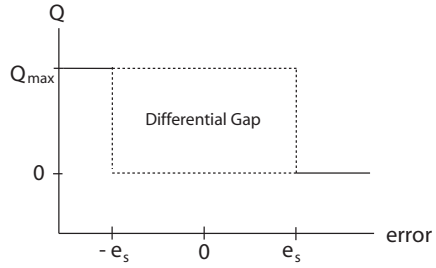

Figure 4.2: Thermostatic differential gap indicating the relationship between the temperature error and the control signal.

Temperature error dead bands establish the boundaries of the differential gap. When the temperature error, $e = T^* - T$, is less than the lower error bound, $e < e_s$, the heater is on, $Q = Q_{max}$. When the temperature error is greater than the higher error bound $e > e_s$, the heater is off ($Q = 0$). For errors within the error bounds, there is hysteresis such that the heater is either on or off depending upon the previous state of the heater. In this application, the resistive heater has been modeled as a non-ideal relay where the actuator "off" position is $Q = 0$. For an ideal relay, the actuator "off" position would be $-Q_{max}$. This is an important distinction which will be discussed in more detail

later. In summary, the discrete time thermostatic control law is represented by

$$u(k) = \begin{cases} Q_{max}, & \text{for } e(k) \leq -e_s \\ 0, & \text{for } e_s \leq e(k) \\ u(k-1), & \text{for } -e_s < e(k) < e_s \end{cases} . \tag{4.8}$$

The specific temperatures selected for the error bounds, e_s, will influence the amplitude of the oscillations in the system thermal response. After the heater turns off, $e > e_s$, some degree of temperature overshoot beyond the reference temperature, T^*, is expected. Conversely, when the heater turns on and the actual temperature has been decreasing, $e < -e_s$, the temperature will continue decreasing for some period of time before responding to the heater. Thus, the steady-state temperature response is oscillatory. The frequency and magnitude of these induced limit cycle oscillations will depend on the system thermal dynamics and the error bounds at which the heater is switched on or off. The error bound, e_s, will be selected to keep the error, e within a specified limit cycle amplitude (or output error range) a.

Selecting this error bound, e_s, is not trivial. Both a describing function methodology as well as a simulation based strategy were employed to tune the thermostatic controllers for the resistive heaters in the humidification system. Table 4.3 summarizes the calculated amplitude and, where applicable, the temperature limit cycle period for each of the three regulated systems evaluated at the nominal conditions. The specific methodologies employed for each thermostatic controller to produce these results are detailed in the following subsections.

Table 4.3: Necessary error bounds to achieve desired amplitude for thermostatic regulation.

System	**Error Bound,** e_s	**Amplitude,** a^*	**Period**
Bypass	0.38^oC	0.5^oC	2 sec
Mixer	0.38^oC	1.0^oC	n/a
Water Circulation	0.21^oC	0.5^oC	58 sec

4.4.1 Water Circulation System Tuning with Describing Function Method

The behavior of a system nonlinearity, such as a relay, can be analytically evaluated by constructing a describing function that approximates the nonlinear response of the relay. Describing functions have been used to quantify the amplitude and frequency of limit cycles induced in relay feedback systems [30, 63], and subsequently used in the tuning of process controllers [21].

The describing function that approximates the behavior of a hysteretic relay nonlinearity was derived for a relay which produces either a positive or negative output, such as $u = \pm Q_{max}$, depending upon the state of the relay [69]. The on-off thermostatic control law specified in Equation 4.8, however, does not allow negative heat to be added to the control volume. As a result, the describing function in [69] was shifted and scaled (as shown in Figure 4.3) to derive the describing function

for a shifted relay with hysteresis,

$$N(a^*, e_s) = \frac{Q_{max}}{2}\left[\frac{4}{\pi a^*}\left(\sqrt{1-\left(\frac{e_s}{a^*}\right)^2} - j\frac{e_s}{a^*}\right)+1\right], \tag{4.9}$$

where a^* is the desired temperature limit cycle amplitude.

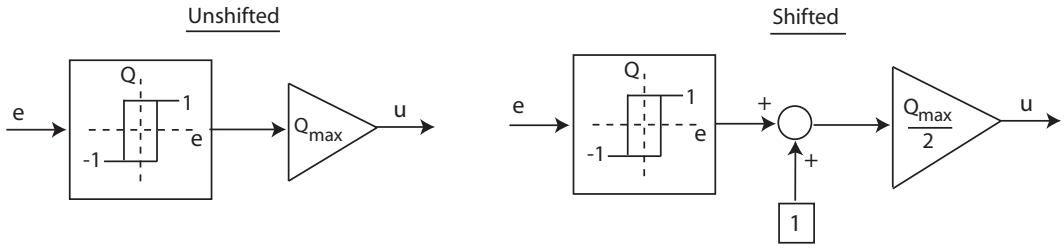

Figure 4.3: Schematic comparing an unshifted versus a shifted relay with hysteresis.

In a relay feedback system, the output temperature of the thermal process, $\delta T(s) = G(s)\delta Q(s)$ where $G(s)$ denotes the plant transfer function (shown in Section 4.3), oscillates with a temperature amplitude of a and frequency ω. Assuming there is no change in the reference temperature and no disturbances to the system, the error bound, e_s, and the resulting frequency of oscillation, ω, can be determined for a given desired amplitude, a^*, by satisfying both the real and imaginary parts of $G(j\omega)N(a^*, e_s) = -1 + 0j$. Alternatively, a range of e_s values could be selected and the intersection of $G(j\omega)N(a^*, e_s)$ with the point -1+0j could be found graphically. In general, as the differential gap expands, implying e_s increases, the resulting limit cycle oscillation amplitude increases and the frequency decreases. If it is desired to specify the limit cycle oscillation frequency and amplitude, not just the amplitude, then an iterative process must be used since there is no guarantee that the selected amplitude and frequency pair will result in a feasible error bound.

This methodology depends on the specification of the desired limit cycle oscillation. If this value is not known, the desired amplitude can be calculated by a combination of the smallest achievable output amplitude, a_{ideal}, which occurs for an ideal relay with no hysteresis, and the standard deviation in the temperature signal at steady-state (temperature measurement noise), σ_n. The process used to select a desired amplitude involved the following steps.

1) A describing function for a shifted ideal relay is formulated by setting e_s=0 in Equation 4.9.
1) The resulting output amplitude which corresponds to the smallest achievable amplitude, a_{ideal}, is calculated by solving $G(j\omega)N(a^* = a_{ideal}, e_s = 0) = -1 + 0j$.
2) The standard deviation in the measurement output noise, σ_n, is quantified.
3) A combination of the smallest achievable output amplitude and the measurement noise is constructed, such as $a^* = a_{ideal} + 3\sigma_n$.

For the Type T thermocouples used to measure the system temperature, the standard deviation in the measurement noise is approximately $\sigma_n \approx 0.08^o$C. Using the ideal relay with no hysteresis, and the plant transfer function given in Equation 4.6 for the water circulation system, the smallest achievable humidifier air outlet temperature oscillations are $a_{ideal,wh} \approx 0.2^o$C. As a result, the smallest output amplitude for the water circulation system, that makes the thermostatic controller

least sensitive to noise, is $a^*_{wc} \approx 0.5^o$C. From evaluation of $\frac{\delta T_{g,hm,o}}{\delta Q_{wh}}(j\omega)N(a^*_{wc}, e_{s,wc}) = -1 + 0j$, the resulting error bound for the water heater is $e_{s,wc} \approx 0.2^o$C which induces a limit cycle of frequency $\omega_{wc} \approx 0.11$ rad/s (corresponding to an oscillation period of 58 seconds) to maintain the desired output amplitude.

The ability of the describing function methodology to accurately estimate the temperature limit cycles was then evaluated by simulating the relay feedback system applied to the nonlinear water circulation system model, as shown in Figure 4.4. The nonlinear model was evaluated at the nominal conditions, from Table 4.1, with no changes in the reference temperature. Generally, the describing function methodology resulted in the selection of error bounds which induce a reasonably expected humidifier air outlet temperature limit cycle period at the desired amplitude.

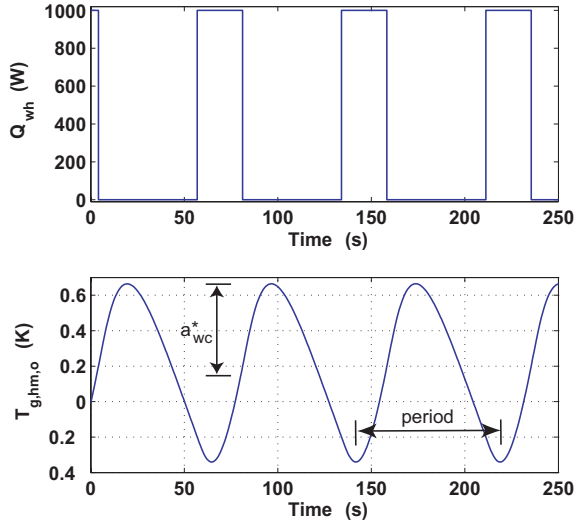

Figure 4.4: Simulation of the temperature oscillations induced in the water circulation system with relay feedback along with the heater control input. The water circulation system plant was simulated using the nonlinear model evaluated at the nominal conditions.

The induced humidifier air outlet temperature limit cycle oscillates with a period of 77 seconds, which is larger than the 58 seconds expected. However, the nonlinear system response oscillates between the forced, $u = \delta Q_{max}$, and the free response, u=0, when the actuator is turned on and off, resulting in different dynamic response times. Starting at the minimum humidifier air outlet temperature, it takes approximately 31 seconds to reach the maximum temperature, indicating an oscillation period of 62 seconds if the free response time were equal to the forced response time. Due to system nonlinearities and the difference between the free and forced dynamic plant responses, the temperature limit cycles are not symmetric about the reference value of δT^*=0; however, the desired limit cycle amplitude is achieved.

Varying the air mass flow rate supplied to the humidifier between $W_{a,hm,i}$=0.21-0.63 g/s (a total air mass flow rate range of 0.3-0.9 g/s at r_{hm}=0.7), the required error bounds range from $e_s \approx$0.14-0.26^{o}C to maintain the desired output amplitude of a^*=0.5^{o}C. This change in air mass flow rate also changes the period of oscillation ranging between 52-74 seconds. In summary, the air mass flow

rate does not significantly impact the necessary error bounds and resulting frequency of oscillation, to motivate the use of variable error bounds for the water circulation system.

4.4.2 Bypass and Mixer Tuning by Simulation

For first order plants, the describing function methodology can not be employed to analytically calculate the thermostatic error bounds. The Nyquist plot of a first order plant remains in the right hand plane. Thus, no intersection exists between the describing function, which accounts for the fundamental component of the nonlinear relay element, and the plant Nyquist. Instead, simulations of the non-ideal relay feedback system are used to examine the resulting temperature limit cycles for the bypass and mixer systems.

To tune the thermostatic error bounds using a simulation based approach, first the error bound, e_s, is set equal to the desired amplitude of the output temperature oscillations, a^*. Of course, the system response will experience overshoot outside of this desired amplitude. Thus, the error bound is incrementally reduced until the simulated temperature error is less than the desired amplitude. This process is summarized as follows.

1) The desired output amplitude, a^*, is selected.
2) The initial temperature error bounds, e_s, are chosen to be equal to the desired temperature output amplitude, such that e_s=a^*.
3) The closed loop non-ideal relay feedback system response is simulated using the nonlinear plant model evaluated at the nominal operating conditions.
4) The simulated temperature error signal is compared to the desired amplitude.
5) If the simulated temperature error remains smaller than the desired amplitude throughout the simulation, then the search is terminated. Otherwise, the temperature error bounds are reduced and steps 3-5 are repeated.

To illustrate the iterative error bound tuning process and the relationship between the temperature limit cycle amplitude and period as a function of the error bound, consider the mixer system assuming constant gas temperatures supplied from the humidifier and bypass (implies constant reference temperature), as shown in Figure 4.5. As expected, as the error bound is decreased, both the period and amplitude of the temperature limit cycle decrease. When the error bound is reduced sufficiently that the induced temperature limit cycle amplitude, a_{mx}, is less than or equal to the desired amplitude, a^*_{mx}, the iteration process is terminated and the necessary error bound has been identified.

Of course, in the physical system, the thermostatically controlled water heater will induce humidifier gas outlet temperature oscillations that impact both the bypass and the mixer, as inputs and/or dynamic reference temperatures. Because the mixer receives air from both the humidifier and the bypass, the temperature oscillations in these systems induce temperature fluctuations in the mixer in practice causing the mixer oscillation frequency to be smaller (period to be larger) than the water circulation system. For low desired cathode inlet relative humidities which result in more air supplied to the bypass than the humidifier, the bypass oscillations would impact the mixer more than the humidifier, resulting in a faster mixer outlet temperature oscillation frequency.

Due to the coupled nature of the humidification system volumes, it is therefore recommended that the bypass and mixer thermostatic controllers be tuned in a manner that accounts for the wa-

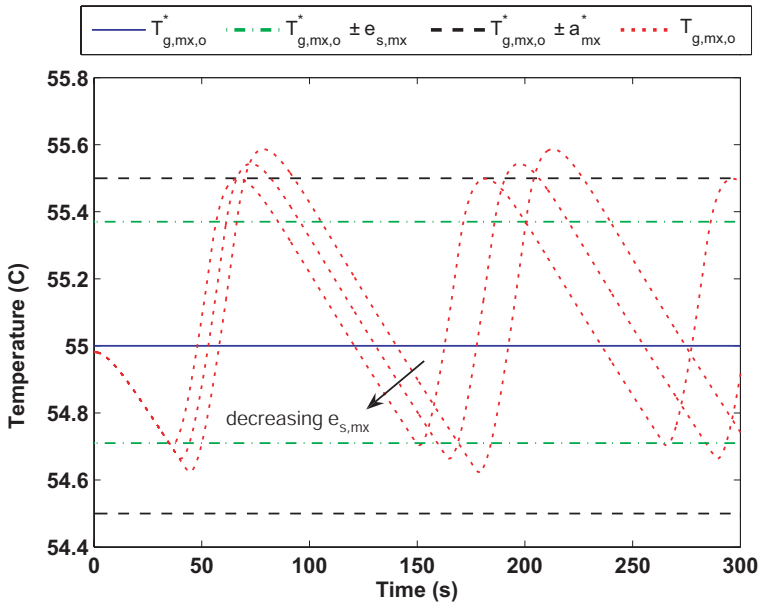

Figure 4.5: Influence of the mixer error bound on the simulated mixer outlet temperature limit cycle for a relay feedback system.

ter circulation system performance. By first selecting the water heater error bounds, as discussed in Section 4.4.1, the error bounds for the bypass relay feedback system can be determined using the simulation based iterative approach described above. Then given the error bounds for the bypass and water heater, the error bounds for the mixer relay feedback system can be determined via simulation. This process of sequential controller tuning is described schematically in Figure 4.6.

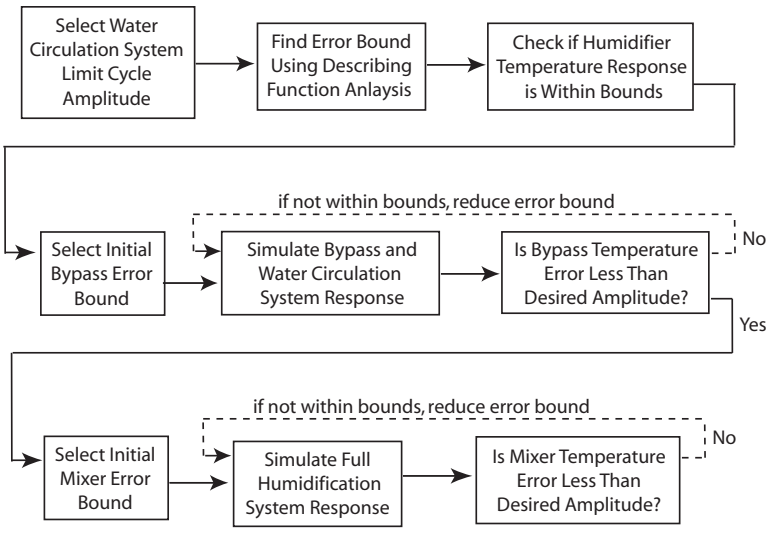

Figure 4.6: Sequential process used to tune the bypass and mixer thermostatic error bounds.

In selecting the desired amplitudes for the bypass and mixer, consideration of the system dynamics must be made. The water circulation system (humidifier) response influences both the mixer

and bypass by establishing an oscillating reference temperature. As with the water heater, to reduce heater relay cycling due to measurement noise the desired bypass temperature limit cycle amplitude was selected to be a^*_{bp}=0.5^{o}C. However, the water circulation system, does not only influence the mixer through the reference temperature. The mixer also receives air and water vapor from the humidifier. As a result, oscillations in the humidifier will cause oscillations in the mixer even when the mixer heater is off. As a result, the mixer amplitude was selected to be a^*_{mx}=1.0^{o}C to account for the 0.5^{o}C amplitude fluctuations due to the water circulation system.

Applying this iterative and sequential simulation based tuning approach, at the nominal operating conditions shown in Table 4.1, the bypass error bound was found to be $e_{s,bp}$=0.38^{o}C to achieve a temperature limit cycle amplitude of a^*_{bp}=0.5^{o}C and the mixer error bound was $e_{s,mx}$=0.38^{o}C to achieve a temperature limit cycle amplitude of a^*_{bp}=1.0^{o}C. Although the error bounds for the bypass and mixer are the same, the two systems achieve very different temperature limit cycle amplitudes due to the relatively slow thermal response of the mixer, as compared to the bypass.

The simulated humidification system thermal response, employing these thermostatic dead bands at nominal conditions, is shown in Figure 4.7. The difference in the closed loop thermal response time of the bypass, mixer and water circulation systems are evident. Note, at approximately 340 seconds, the increase in the temperature of the air leaving the humidifier causes the mixer temperature to increase although the mixer heater had been turned off. Additionally, there is a relatively small amount of noise in the mixer temperature due to the fast oscillations in the bypass temperature, but has less impact on the mixer temperature due to the large mass fractional split of air flow directed to the humidifier ($r_{hm} = 0.7$). When the fraction of the air mass flow rate directed to the bypass is increased, these oscillations are more pronounced.

The influence of the total air mass flow rate on the mixer and bypass error bounds was considered by identifying the respective error bounds at different flow rates. As with the water circulation system, a range of total air mass flow rates between 0.3-0.9 g/s was considered assuming 70% of the air is delivered to the humidifier (r_{hm}=0.7). The bypass error bounds show little sensitivity to the air mass flow rate, ranging from $e_{s,bp}$=0.36-0.41^{o}C. Of course, if low relative humidity operation is desired, more air would be supplied to the bypass resulting in a greater sensitivity in the bypass error bounds. The mixer error bounds, however, exhibit a greater degree of sensitivity to the total air mass flow rate, ranging from $e_{s,mx}$=0.14-0.65^{o}C to achieve the desired temperature limit cycle amplitude of a^*_{mx}. As the total air mass flow rate increases, the necessary mixer error bounds increase. Such sensitivity to the total air mass flow rate could motivate the use of variable mixer error bounds. However, constant error bounds could still be used with the understanding that the desired amplitude will only be achieved at the total air mass flow rate that the controller was tuned for.

The thermostatic controllers, designed and shown in simulation here in Section 4.4, are cheap to implement, have a relatively easy tuning methodology, and are capable of regulating the humidifier temperature to within 1^{o}C of the desired cathode inlet temperature. However, if zero steady-state temperature error ir required or the limit cycle temperature oscillations are undesirable, a more sophisticated controller can be used. In the following section, a proportional-integral controller will

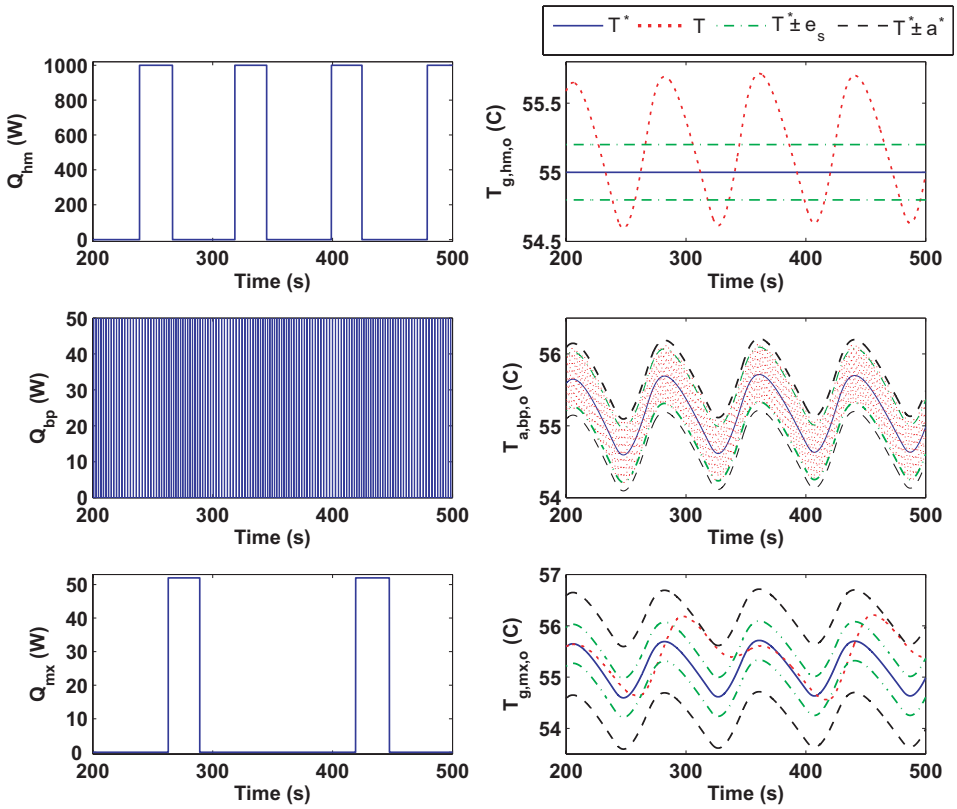

Figure 4.7: Thermostatic controller simulation with tuned deadbands under nominal conditions. The left column of plots shows the actuator control signals and the right column of plots displays the thermal response of the control volume temperature being regulated.

be developed to further improve the system response.

4.5 PI Controller Tuning with Integral Anti-windup

By adding integrator states to the controllers, zero steady-state error to a step command in the reference temperature can be achieved. As a result, proportional integral (PI) control was considered due to the simplicity of tuning with time domain constraints and guarantee of zero steady state error. The PI controller can be expressed in the frequency domain as

$$\delta Q_{cv} = \left(k_{P,cv} + \frac{k_{I,cv}}{s} \right) e \, , \tag{4.10}$$

where the proportional and integral controller gains are denoted by $k_{P,cv}$ and $k_{I,cv}$, respectively, for each control volume. By substitution into Equations 4.5-4.7, the closed loop transfer functions from the reference to the actual temperature can be found. In contrast to on-off thermostatic control, PI control requires the heater actuators to produce a variable heat transfer rate. Thus, there is a fundamental tradeoff between regulation capability and hardware and software complexity.

A summary of the final controller gains and resulting settling times assuming a step change in the reference temperature, δT^*=1^{o}C, is shown in Table 4.4 along with the gain and phase margins. The following subsections will detail the methodology used in designing these controllers and the inclusion of integrator anti-windup to address actuator saturation.

Table 4.4: Proportional Integral Controller Gains

Heater	$k_{P,cv}$	$k_{I,cv}$	t_{settle} (s)	GM (dB)	PM (deg)
Bypass	15	3.25	9.4	∞	142
Mixer	25	0.22	256	∞	145
Water Heater	263	1.60	176	20	138

For the mixer, bypass and water circulations systems, the input disturbances are the same, namely the ambient temperature and the total air mass flow rate. It can be assumed that the ambient temperature remains relatively constant throughout an experiment. However, the total air mass flow rate varies significantly. To reduce the impact of this disturbance on the system temperature responses, precompensation could be used [17]. Note, this precompensation would increase or decrease the amount of heat that is added to the system as a result of the change in total air mass flow rate, which is distinctly different than the static nonlinear feedforward mapping from Section 4.1 used to control the mass fractional split of air supplied to the bypass and the humidifier to regulate relative humidity. Interestingly, the steady-state incremental heat required by the system due to a change in air mass flow rate is relatively small, rendering constant precompensation relatively ineffective.

4.5.1 Mixer and Bypass PI Gain Tuning

The open loop transfer function from the heater input to either the bypass or mixer gas outlet temperature, shown in Equations 4.5 and 4.7, are first order. The application of PI control then results in a second order closed loop transfer function, from the temperature reference to the gas outlet temperatures, described generally by

$$\frac{\delta T_{g,cv,o}}{\delta T^*_{g,cv,o}} = \frac{b_{o,cv}k_{P,cv}(s+k_{I,cv}/k_{P,cv})}{s^2+(b_{o,cv}k_{P,cv}+p_{cv})s+b_{o,cv}k_{I,cv}}\,, \tag{4.11}$$

where p_{cv} is the open loop pole location for the bypass or mixer system previously shown in Equation 4.5 and 4.7.

Upon inspection of the characteristic polynomial of this closed loop transfer function, the PI controller gains can be tuned to achieve specific time domain constraints. For tuning the controller gains, two of the following three constraints must be selected, from the 1) proportional controller gain, 2) response time, or 3) damping coefficient which influences the degree of overshoot experienced to a step in the temperature reference. The proportional controller gains can be easily selected based on the desired heater response for a specific temperature error. A decision must then be made

as to the specification of the desired response time or the overshoot. Because the avoidance of condensation and dehydration is of critical importance in controlling the humidification system, the damping coefficient is chosen as the second time domain design constraint to be specified. By minimizing overshoot, at the expense of a slower closed loop response time, the effects of condensation and dehydration can be directly addressed.

The proportional gains are selected based on the expected maximal actuator heater power at steady-state over the range of operating conditions, $Q_{design,cv}$, supplied for a specified temperature error, $e_{design,cv}$, such that

$$k_{P,cv} = \frac{Q_{design,cv}}{e_{design,cv}} \; . \tag{4.12}$$

This selection of the proportional controller gains implies that energy will be supplied to the heater at the rate, $Q_{design,cv}$, when the temperature error changes from 0^oC to $e_{design,cv}$. Using simulations, the maximum amount of heat required, across the range of operating conditions, can be determined to motivate the selection of $\delta Q_{design,cv}$. Given an expected error of $e_{design,cv}$=1.0^{o}C and the maximum steady-state heater power of $Q_{design,bp}$=15W and $Q_{design,mx}$=25W, the proportional gains were found to be $k_{P,bp}$=15W/K and $k_{P,mx}$=25W/K.

Theoretically, to achieve no overshoot in the response to a step change in the reference temperature, the desired damping coefficient for a critically damped response is chosen to be ζ=1. Examining the characteristic equation of the closed loop transfer function in Equation 4.11, with the specified proportional gain given in Equation 4.12, the integral gain can be expressed as

$$k_{I,cv} = \frac{b_{o,cv}k_{P,cv} + p_{cv}}{4b_{o,cv}} \; . \tag{4.13}$$

Given the mixer and bypass open loop transfer function coefficients ($b_{o,bp}$, $b_{o,mx}$, p_{bp}, and p_{mx} from Equations 4.5 and 4.7, the resulting controller integral gains are $k_{I,bp}$=3.25 and $k_{I,mx}$=0.22. With the selection of these PI controller gains for the mixer and bypass, the closed loop settling times to a 1^{o}C step in the reference temperature are 9 and 256 seconds, respectively. As expected, the response time of the bypass is considerably faster than the response time of the mixer system.

To examine the relative stability of the closed loop systems, the most frequently used metrics are the gain and phase margins which for a stable system indicate the amount of gain and pure delay that can be added to the loop before the closed-loop system becomes unstable [34]. Figure 4.8 provides a Bode plot of the magnitude and phase of the closed loop bypass and mixer systems. The resulting gain and phase margins are presented in Table 4.4. The high frequency phase angle asymptote for both systems is -90 degrees, rather than the -180 degrees expected of a second order system due to the addition of the zero from the controller. Clearly, the mixer and bypass closed loop transfer functions have a relative degree of 1 which results in an infinite gain margin, implying the closed loop system will be stable for all loop gains. Additionally, the large phase margins indicate adequate robustness to system delays due to parameter variation. Note, the peak in magnitude near the corner

frequency indicates there will be an overshoot in the step response. Although the controllers were designed for a critically damped response, implying no overshoot, in actuality overshoot will result due to the zero added by the controller.

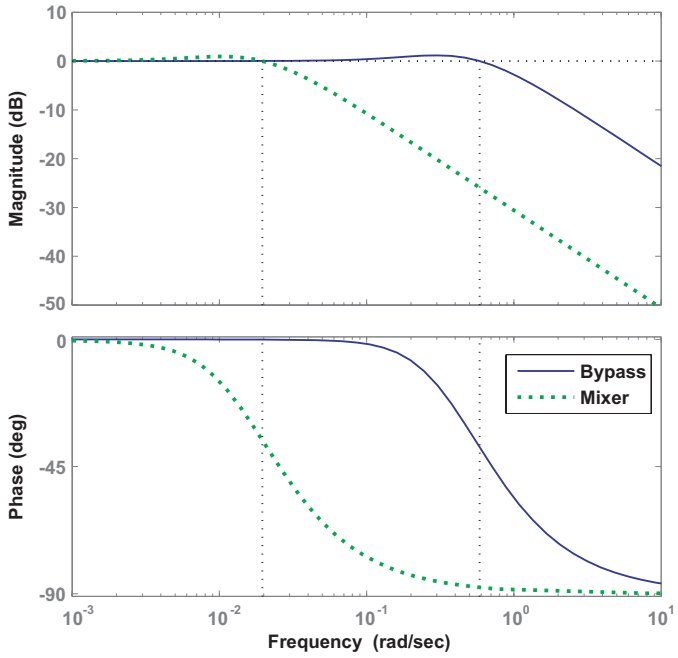

Figure 4.8: Bode plots of the mixer and bypass closed loop systems indicating gain and phase margins.

4.5.2 Water Heater PI Gain Tuning

The closed loop transfer function from the reference humidifier air outlet temperature to the actual temperature is of high order and therefore, time domain design constraints (overshoot, settling time, etc.) can not be used analytically to specify the PI controller gains as was done for the bypass and mixer. Instead, pole placement was used iteratively to achieve a desired closed loop response. From inspection of the open loop water circulation system poles and zero, from Equation 4.6, it is seen that a stable slow pole is located on the real axis of the complex s-plane at approximately s=-0.00082. This pole could be either shifted or canceled by a carefully tuned PI controller. In the work by [41], it was shown that a tradeoff exists between input disturbance rejection and robustness to modeling errors when considering whether to cancel or shift a slow stable pole which lies on the real axis. The humidifier water circulation system has an air mass flow rate input disturbance and the model parameters were considered to be well identified. As a result, a pole shifting controller was employed for improved input disturbance rejection.

Using the full order linearized model of the water circulation system, shown in Equation 4.6, a pole shifting PI controller of the form given in Equation 4.10, was tuned to achieve a fast response with less than 20% overshoot. The resulting closed loop system, with the controller gains listed in

Table 4.4, is stable with all poles located in the open left half complex s-plane.

To examine the relative stability of the closed loop water circulation closed system, a Bode plot of the magnitude and phase, shown in Figure 4.9 was used to calculate the gain and phase margins, found in Table 4.4. A sufficient gain and phase margin are achieved for robustness to parameter variation. The high frequency phase angle asymptote for this systems is -360 degrees due to the transfer function having a relative degree of 4. As with the bypass and mixer, the peak in magnitude near the corner frequency indicates there will be an overshoot in the step response.

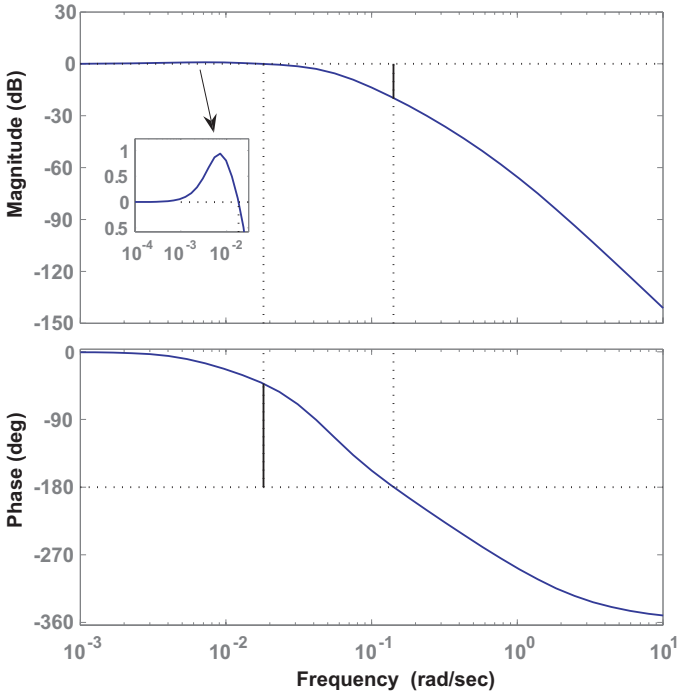

Figure 4.9: Bode plots of the water circulation system closed loop systems indicating gain and phase margins.

4.5.3 Integral Anti-windup Strategies

If an actuator has saturation limits, as is the case for the resistive heaters, the integrator will continue to integrate the error signal while the actuator is saturated, causing an increasing discrepancy between the desired control signal and the saturated control signal. When the error begins to decrease in magnitude, a time lag will occur before the actuator will no longer be saturated due to the previously growing integrator state. This delay can result in an undesired overshoot (or undershoot), referred to as integrator windup. Two strategies for employing integrator anti-windup will be considered, and their relative merits addressed.

The difference between the actual, δQ_{cv}, and saturated, δQ_{sat}, control signals can be scaled and removed from the error signal prior to integration [2], as shown in Figure 4.10. In this manner, the scaling factor, α, controls the rate of convergence of the integrator anti-windup. Unfortunately,

the rate of convergence parameter has a significant influence on the system response time and degree of overshoot following a step change in the reference signal. The PI Controller with integrator anti-windup can then be clearly expressed in the time domain as

$$\delta Q_{cv}(t) = k_{P,cv}e(t) + \int_0^t \left[k_{I,cv}e(\tau) + \alpha(\delta Q_{cv}(\tau) - \delta Q_{cv}^{sat}(\tau))\right] d\tau \,, \tag{4.14}$$

where the deviation in the control signal from nominal conditions upstream and downstream of the actuator model are denoted by δQ_{cv} and δQ_{cv}^{sat}, respectively. This anti-windup strategy will be referred to as "convergence based".

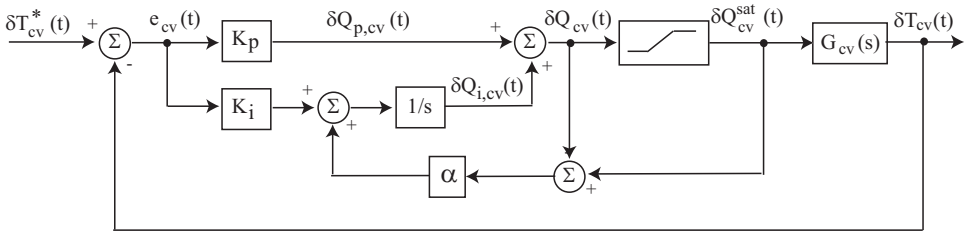

Figure 4.10: Proportional integral control schematic with convergence based integral anti-windup.

Alternatively, the integral anti-windup can be replaced by a logic based case structure which enables or disables the integrator while the actuator is saturated. If the control signal upstream of the actuator saturation model is not equal to the control signal downstream of the actuator saturation model, implying the actuator is saturated, then the integrator is turned off. This logic can be implemented as shown in Figure 4.11, and will be referred to as "logic based".

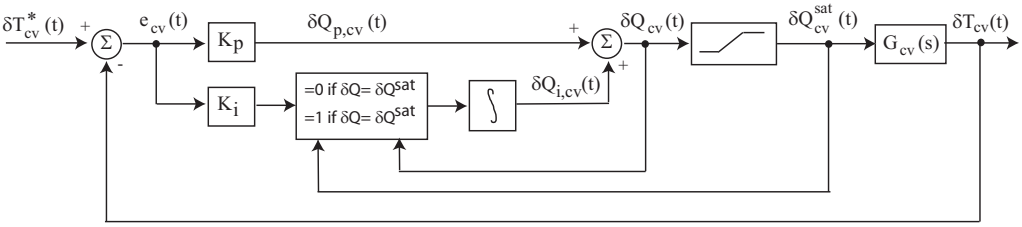

Figure 4.11: Proportional integral control schematic using logic to stop integrating the error signal when the actuator saturates.

With the logic based formulation for employing integrator anti-windup, there is no convergence rate, α, which requires tuning as was the case for the convergence based anti-windup strategy. The control law with logic based anti-windup is then described by the following equation:

$$\delta Q_{cv}(t) = \begin{cases} k_{P,cv}e(t) + \int_0^t k_{I,cv}e(\tau)d\tau & \text{if } \delta Q_{cv}(t) = \delta Q_{cv}^{sat}(t) \\ k_{P,cv}e_{cv}(t), & \text{if } \delta Q_{cv}(t) \neq \delta Q_{cv}^{sat}(t) \end{cases} .$$

The rate of convergence parameter, α, has a significant influence on the system response time and the degree of overshoot experienced following a step change in the reference signal. Figure 4.12 compares the logic and convergence based anti-windup strategies applied to the PI controller for the

mixer system response to a step in the reference temperature. For the convergence rate based anti-windup, the range of responses are shown for varying α. Each row of subplots shows the response to a different reference step size, with the temperature response in the right plot and the actuator signal in the left plot. Each reference step change is taken from the nominal conditions.

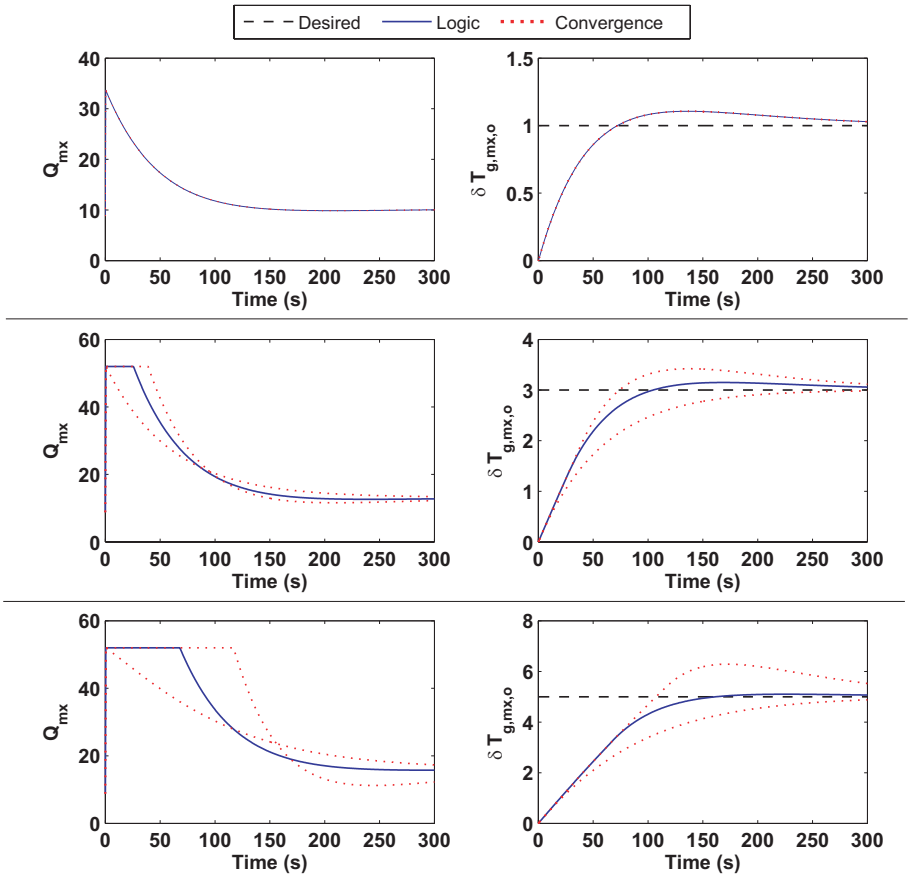

Figure 4.12: Comparison of the reduced order mixer closed loop step response employing the PI controller using different anti-windup strategies. The dotted line indicates the performance of the logic based anti-windup strategy. The dashed lines indicate the bounds on the response time using the convergence rate based anti-windup where the response for varying α lies within these bounds.

For a step size of $\delta T^*_{g,mx,o} = 1^oC$, the actuator does not saturate, resulting in the same temperature response for the two anti-windup strategies. However, for larger step sizes, the actuator does saturate and the performance of the anti-windup strategies can be compared. The rise time of the logic based anti-windup strategies is approximately equal to the rise time of the response if no anti-windup is used (upper bound of convergence based anti-windup), however there is significantly less overshoot.

A rate of convergence, α, does exist such that the control signal response following actuator saturation is the same for both the logic and convergence based strategies for a step size of a particular magnitude. Although, for a given rate of convergence, the control signal will not be the same for these two anti-windup strategies for all magnitudes of reference step sizes, for a value of α=0.032

the response of the two anti-windup strategies is similar for the range of reference steps considered here. For simplification due to the need to tune the convergence rate to achieve the desired temperature response across a range of reference step changes, the logic based anti-windup strategy will be used.

4.6 Hardware Implementation of Controllers

This section describes the process used to implement the controllers in hardware and then compares the performance of the controllers. First, the modeling required to emulate the hardware implementation of the controllers, for example accounting for the effects of sampling and measurement noise, are discussed. Then, the closed loop humidification system performance is simulated to examine the influence of the physical hardware constraints. Finally, the experimental performance of the thermostatic and PI controllers are compared.

4.6.1 Models for Emulation of Hardware Constraints

The data acquisition system forces implementation of the control and monitoring system in discrete time, as previously discussed in Section 1.2. As a result, the continuous time domain controllers must be expressed in discrete time for the control signals to be executed using digital electronics. For implementation of the on-off thermostatic controllers, no conversion must be made since a relay can be simply opened or closed. The PI controllers, however, are expressed as a difference equation by

$$\delta Q_{cv}[kT_s] = k_{P,cv}e[kT_s] + k_{I,cv}T_s \sum_{j=T_s}^{kT_s} e(j) \ , \tag{4.15}$$

where the symbol kT_s is used to denote a discrete instant of time where k is a time index and $T_s \approx 0.05$ is the data acquisition system sample time (s).

The details of the humidification system hardware were provided in Section 3.1. For all analog inputs (sensor measurements) and outputs (actuator signals), zero-order holds were used to model the effect of sensor sampling in hardware. Both the bypass and the mixer controllers utilize analog output signals. However, the water heater actuator is controlled with a digital signal that is pulse width modulated (in software) using a pulse period of 0.5 seconds. As a result, a 0.5 second zero order hold is used to model the updating of the water heater control signal.

The analog input temperature measurements do in fact contain measurement noise. Type T thermocouples were employed for sensing temperature throughout the system. Theoretically, these thermocouples should all exhibit similar noise characteristics. They were calibrated, using a continuously stirred hot water bath, against a thermometer with a precision of 0.01^oC. Although there could be a bias in the temperature measurement if this reference temperature was not accurate, the thermocouples will all contain the same bias as they were calibrated under the same conditions.

To characterize the output temperature measurement noise, a set of temperature data were de-trended. The de-trending technique performed a local linear least squares regression by fitting a straight line through a moving window of 19 data points. The results did not change significantly as the number of data points included in the moving window changed. Figure 4.13 shows the temperature measurement and the de-trended result as a function of time under similar conditions as those used in the humidifier experimental data presented throughout this document. The noise was then quantified as the difference between the actual and the de-trended temperature, shown in the second subplot. The noise range remains constant throughout the entire experiment despite the fact that the measured temperature is changing.

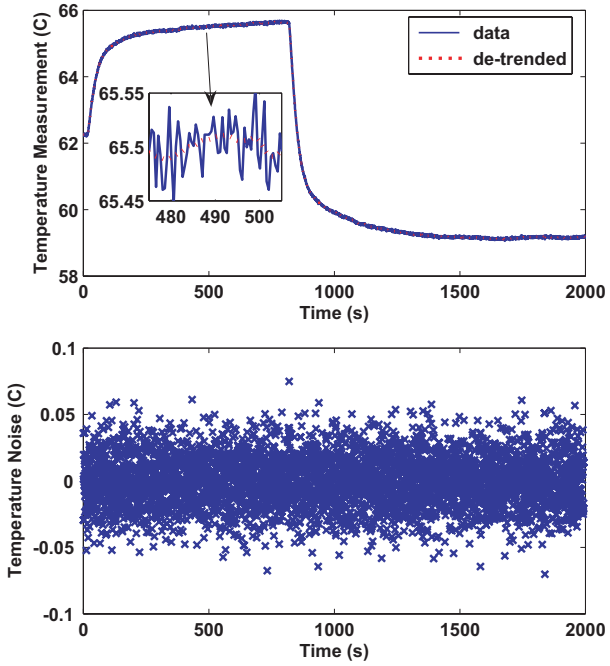

Figure 4.13: Thermocouple temperature measurement and noise.

Based on the noise statistics, the temperature measurement noise was modeled from a normal distribution with a mean of 0^oC and standard deviation of 0.02^oC. Note, the data acquisition system has an expected precision of 0.015^oC with a 16 bit analog input data acquisition board. This measurement noise is added to the modeled temperature outputs and influences the temperature error and control signals.

4.6.2 Simulated Closed Loop Performance

The closed loop humidification system, employing thermostatic and PI controllers, was simulated to compare the controller performances following steps in the reference temperature, total air mass flow rate, and desired mixer outlet relative humidity. The implementation of digital controllers and the model of temperature measurement noise, previously discussed in Section 4.6.1, were accounted for in the model simulations.

Figures 4.14-4.17 provide a comparison of the humidification system responses employing the PI and thermostatic controllers initialized at the nominal conditions. As expected, the thermostatic controllers produce temperature limit cycle oscillations at the designed amplitudes and frequencies. For all three temperature responses, the thermostatic controllers result in a faster response time to a step in the reference temperature, due to the initial saturation of the controller. The PI controllers regulate temperature with zero steady-state error and result in a 2-5% reduction in total heater energy consumption. Finally, the temperature measurement noise has little impact on the control signals or, ultimately, the ability to regulate temperature for either control architecture.

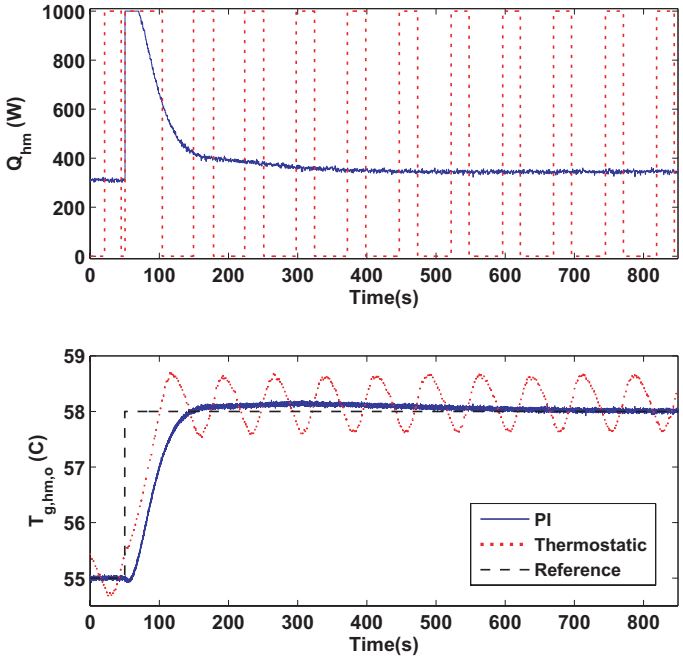

Figure 4.14: Simulated humidifier air outlet closed loop temperature response to a reference step, comparing the use of PI versus thermostatic control. The first subplot shows the power supplied to the water heater and the second subplot shows the temperature response.

The humidifier air outlet temperature response for both the thermostatic and PI controllers, following the step in the reference temperature shown in Figure 4.14, performed as designed. Immediately following the change in the reference temperature, the air mass flow rate supplied to the humidifier, shown in Figure 4.17, is increased. This increase causes the humidifier air outlet temperature to initially decrease. It is important to note that this is not a non-minimum phase response, rather it is due to the feedforward air flow regulation and the influence of the air mass flow rate on the humidifier temperature.

As expected, due to the relatively fast closed loop response time of the bypass, as compared to the water circulation system, the bypass air outlet temperature is well regulated using PI control, with little difference between the actual and reference temperature shown in Figure 4.15. In contrast, using thermostatic control the temperature limit cycle is amplified as a result of the oscillating reference temperature. Note, the humidifier air outlet temperature is the reference for the bypass,

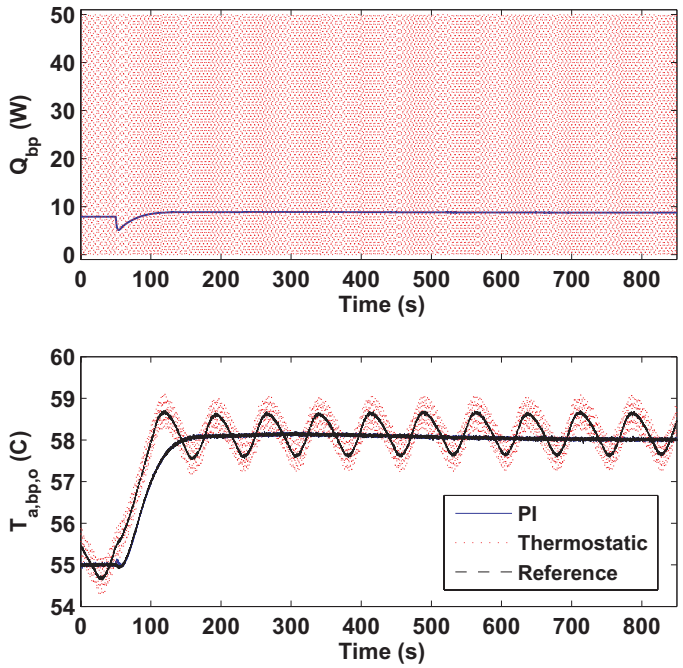

Figure 4.15: Simulated bypass air outlet closed loop temperature response to a reference step, comparing the use of PI versus thermostatic control. The first subplot shows the power supplied to the bypass and the second subplot shows the temperature response.

resulting in two different temperature references using either PI or thermostatic control.

As with the bypass, the mixer reference temperatures for the simulations with thermostatic and PI control, shown in Figure 4.16, are different due to the humidifier air outlet temperature responses. Using thermostatic control, the mixer gas outlet temperature experiences a repeatable but non sinusoidal temperature limit cycle due to the influence of the air supplied to the mixer from the humidifier. The PI controller, however, well regulates the mixer outlet temperature with little overshoot and a fast response.

The resulting mixer outlet relative humidity, using both PI and thermostatic control of the heaters, during this step in the temperature reference is shown in Figure 4.17. Clearly, the non-sinusoidal mixer outlet temperature limit cycle induces a relative humidity limit cycle due to the coupling of relative humidity and temperature. The air mass flow rates supplied to the bypass and humidifier are influenced by the difference in the actual and reference temperatures, implying the air mass flow rate changes during transients. With thermostatic control, the air mass flow rates do not achieve a constant final value due to the temperature limit cycle oscillations. In contrast, the desired relative humidity can be maintained with PI control. It is anticipated that the relative humidity excursions will be more pronounced in hardware due to un-modeled delays in the air mass flow control response.

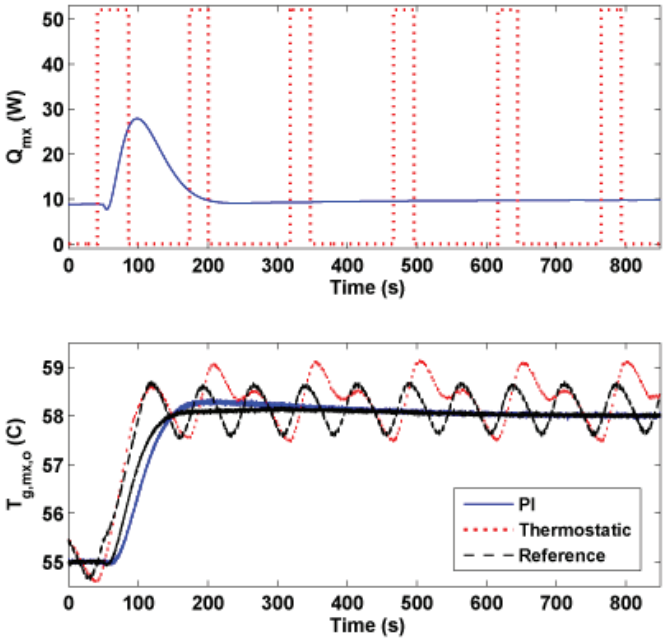

Figure 4.16: Simulated mixer air outlet closed loop temperature response to a reference step, comparing the use of PI versus thermostatic control. The first subplot shows the power supplied to the mixer heater and the second subplot shows the temperature response. Note, there are two different temperature references for the two controllers.

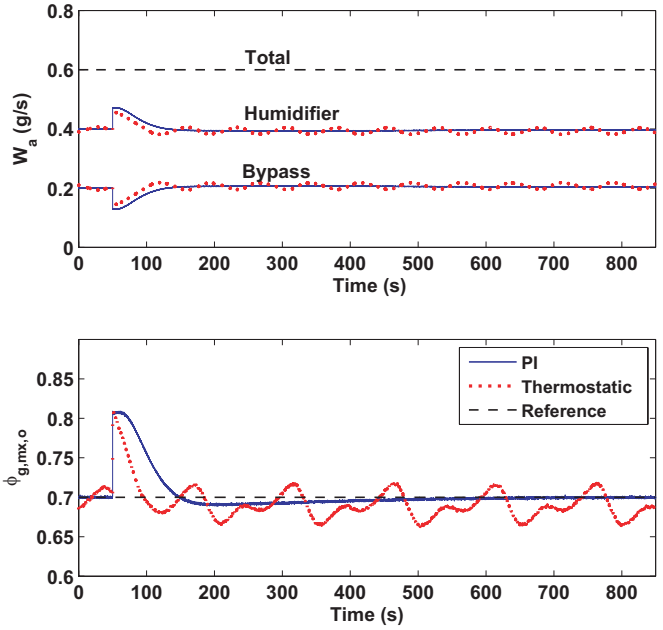

Figure 4.17: Simulated mixer gas outlet relative humidity response during a step in the reference temperature, comparing the use of PI versus thermostatic control. The first subplot shows the total, humidifier and bypass air mass flow rates and the second subplot shows the mixer gas outlet relative humidity.

4.6.3 Closed Loop Experimental Results

Using feedforward control of the fraction of the total air mass flow rate supplied to the humidifier, according to Equation 4.1, four closed loop experiments were conducted to compare the thermostatic and PI controller responses. First, the two controllers are compared for a step in the reference temperature from nominal conditions, shown in Figures 4.18-4.21, similar to the simulation results shown previously in Figures 4.14-4.17. Generally, the PI and thermostatic controllers perform as designed. Then, the two controller performances are examined during steps in the total air mass flow rate, desired relative humidity, and during a water reservoir fill event (where cold water is injected into the reservoir).

Closed loop experimental results for a step in reference temperature

The experimental response of the water circulation system to a step in the reference temperature is shown in Figure 4.18 for both thermostatic and PI control. The desired temperature limit cycle amplitude of 0.5^oC using thermostatic control is achieved. However, a larger oscillation period of 120 seconds occurred, mostly due to the free response of the water circulation system when the heater is turned off. The time required to reach the maximum limit cycle temperature from the minimum limit cycle temperature is approximately 34 seconds, corresponding to a 68 second temperature limit cycle period if the free and forced response times were the same, agreeing with the simulation results. Should the temperature limit cycle oscillation period need to be exactly replicated, a better approximation of the heat transfer loss would be required.

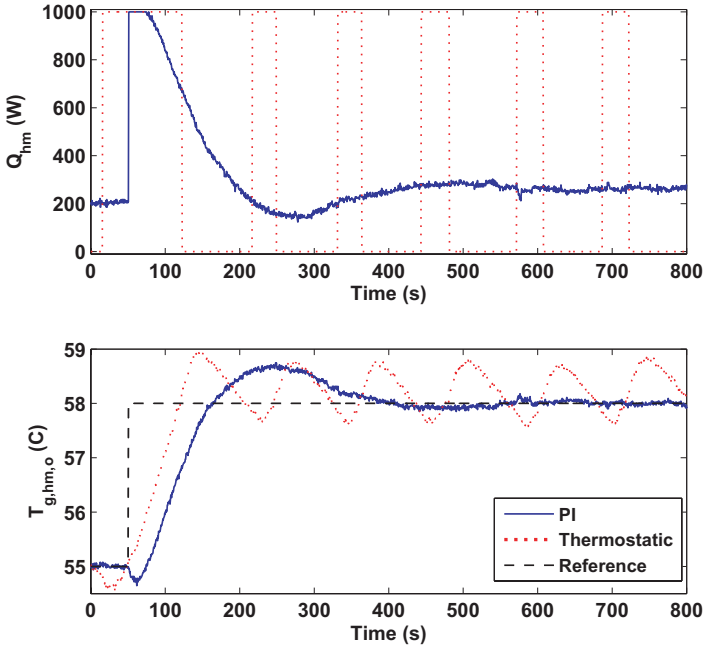

Figure 4.18: Experimental humidifier air outlet closed loop temperature response to a reference step, comparing the use of PI versus thermostatic control. The first subplot shows the power supplied to the water heater and the second subplot shows the temperature response.

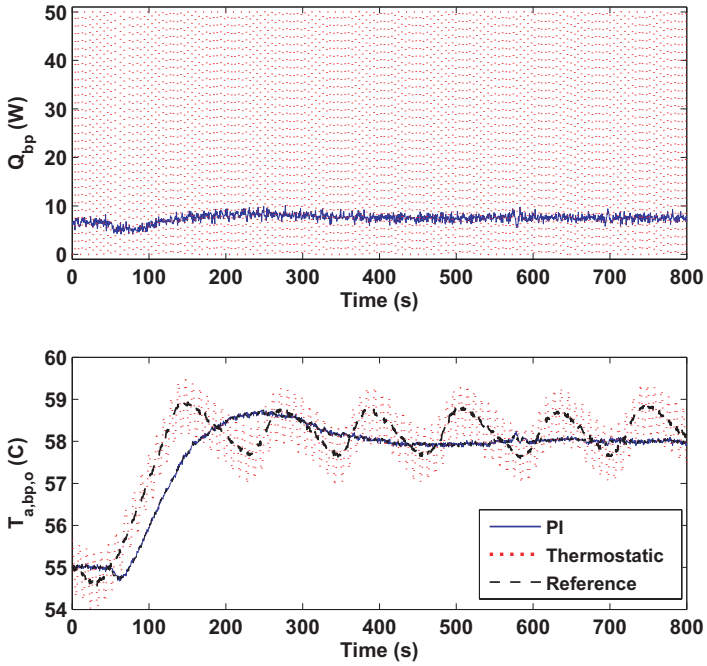

Figure 4.19: Experimental bypass air outlet closed loop temperature response to a reference step, comparing the use of PI versus thermostatic control. The first subplot shows the power supplied to the bypass and the second subplot shows the temperature response.

For the water circulation system PI controller, the resulting overshoot following the step in the reference temperature is larger than predicted in simulation but still within the designed 20%. The response time was similar to that predicted in simulation. However, the initial decrease in the humidifier air outlet temperature following the reference step is more pronounced than was predicted in simulation. This air mass flow rate sensitivity may have occurred as a result of the un-modeled condensation or evaporation dynamics due to the increased humidifier air flow mass rate. Finally, the water heater PI controller is capable of tracking the reference temperature with zero steady-state error.

The experimental response of the bypass to a step in the humidifier reference air temperature is shown in Figure 4.19 comparing thermostatic and PI control. The closed loop experimental results are quite similar to the simulation results presented in Figure 4.15. The resulting temperature limit cycle amplitude is approximately 0.5^{o}C, as designed. Throughout the experiment, the PI controller is capable of tracking the dynamic reference humidifier air outlet temperature with approximately zero steady-state error.

The experimental response of the mixer system to a step in the humidifier reference air temperature is shown in Figure 4.20 comparing thermostatic and PI control. Of interest, the mixer outlet temperature limit cycle, using thermostatic control, is approximately sinusoidal, as compared to the non sinusoidal limit cycle shown in simulation. The limit cycle amplitude was found to be slightly less than the designed 1^{o}C. The mixer PI controller performed as expected throughout the experiment.

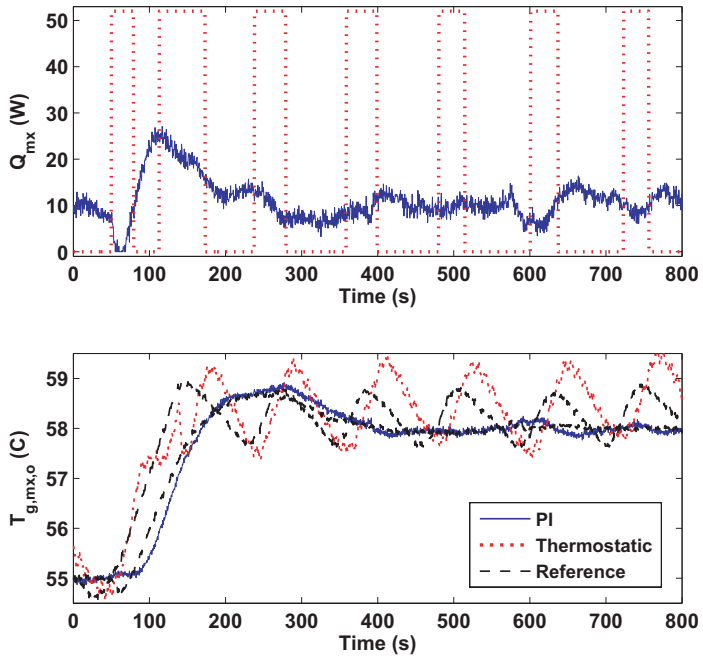

Figure 4.20: Experimental mixer air outlet closed loop temperature response to a reference step, comparing the use of PI versus thermostatic control. The first subplot shows the power supplied to the mixer heater and the second subplot shows the temperature response.

The experimental mixer air outlet relative humidity response during the step in the humidifier reference air temperature is shown in Figure 4.21 comparing thermostatic and PI controller implementation. The actual mixer relative humidity response is quite similar to the simulated results previously shown in Figure 4.17. Because the actual mixer outlet temperature experiences an approximately sinusoidal temperature limit cycle using thermostatic control, the resulting relative humidity also exhibits an approximately sinusoidal response. Both in simulation and in the experiment, the maximum excursion in the mixer air outlet relative humidity is approximately 10% for both controllers. Note, the mixer gas outlet relative humidity presented here is an estimation based on physical measurements applying Equation 3.21.

Thermostatic closed loop experimental results during disturbances

Using feedforward control of the air mass flow rate and thermostatic control of the resistive heaters, a closed loop experiment was conducted by changing the desired cathode inlet temperature and relative humidity. Figure 4.22 shows the humidifier air outlet temperature response first during a step change in the reference temperature. As expected, the heater initially turns on following the increase in the reference temperature which allows a fast initial response time. The temperature oscillations induced by this relay feedback system then begin after the temperature error reaches the differential gap. Note, the temperature response time when the heater is turned on, forced response, is different than when the heater is turned on, free response, also seen by the difference between the time the

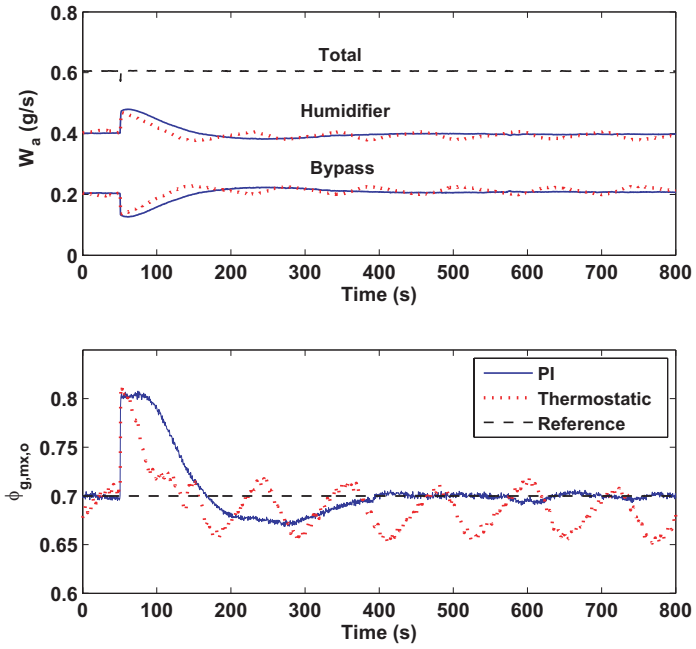

Figure 4.21: Estimated experimental mixer gas outlet relative humidity response during a step in the reference temperature, comparing the use of PI versus thermostatic control. The first subplot shows the total, humidifier and bypass air mass flow rates and the second subplot shows the mixer gas outlet relative humidity.

heater is in the on versus the off state. A reservoir fill disturbance occurring at approximately 3900 seconds, requiring an injection of cold water into the water reservoir, follows the step change in the reference temperature and causes a 2^oC excursion in the humidifier air outlet temperature and increases the length of time that the water heater is on. At approximately 4600 seconds, the desired mixer outlet relative humidity is increased from $\phi^*_{ca,i}$=0.7 to 0.8, causing an increase in the fraction of air supplied to the humidifier. The use of feedforward control of the air mass flow rate supplied to the humidifier results in a variable flow that oscillates at the same frequency as the air temperature, through the water vapor saturation pressure.

Remember, the intent of the bypass controller is to track the humidifier air outlet temperature, which is oscillating due to the thermostatic regulation. As a result, it is expected that the bypass air outlet temperature will oscillate about the humidifier air outlet temperature at a faster frequency. Figure 4.23 displays the regulation capability of the bypass controller during the step change in the cathode inlet temperature. As expected, the bypass tracks the humidifier resulting in an amplified temperature oscillation about the humidifier temperature. Due to the significant difference in the closed loop response time of the bypass and the humidifier, the bypass tracks the humidifier well throughout the range of changes in reference and disturbance values.

The oscillations in the humidifier and bypass temperatures being supplied to the mixer impact the resulting oscillations in the mixer outlet temperature. Although the closed loop mixer relay feedback system is capable of responding faster than the humidifier, it is designed to track the hu-

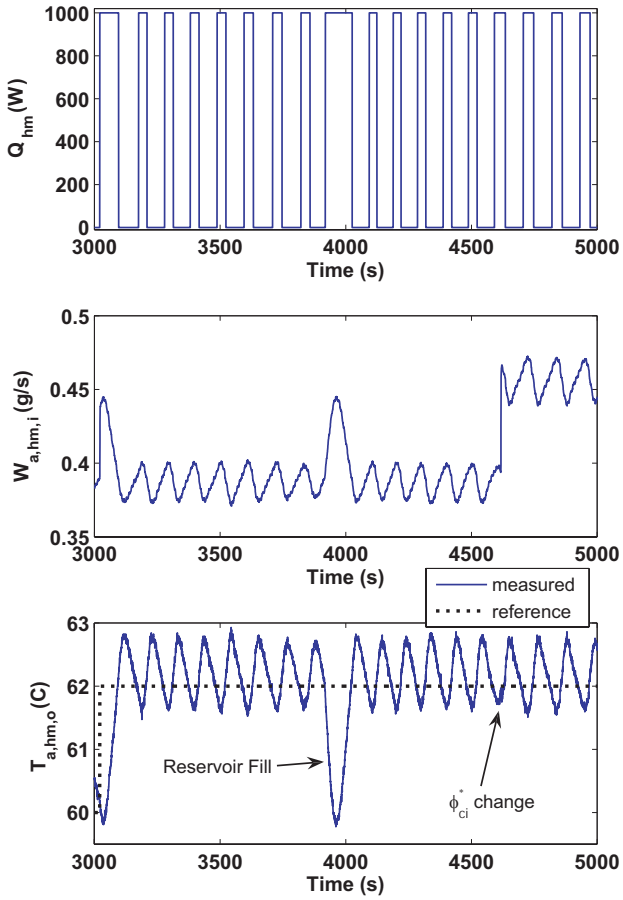

Figure 4.22: Humidifier air outlet temperature thermostatic regulation during step changes in the reference temperature and the desired cathode inlet humidity. The first subplot shows the water heater power, the second subplot shows the air mass flow rate supplied to the humidifier using reference feedforward, and the third subplot shows the thermostatically regulated humidifier air outlet temperature.

midifier, and thus exhibits a similar frequency and amplitude in the limit cycle oscillations. Figure 4.24 shows the mixer response using thermostatic regulation for the same references and disturbances as that shown for the humidifier in Figure 4.22. The total air mass flow rate supplied to the humidifier and bypass is shown, with short transients during changes in the desired cathode inlet relative humidity and temperature. Although the mixer outlet relative humidity oscillates at the same frequency as the temperature, the amplitude is not significant and is close to the measurement resolution of 0.025 or 2.5%.

PI closed loop experimental results during disturbances

Using feedforward control of the air mass flow rate and proportional integral control of the resistive heaters, another closed loop experiment was conducted by changing the desired cathode inlet temperature and relative humidity. Figure 4.25 shows the humidifier, bypass and mixer air outlet

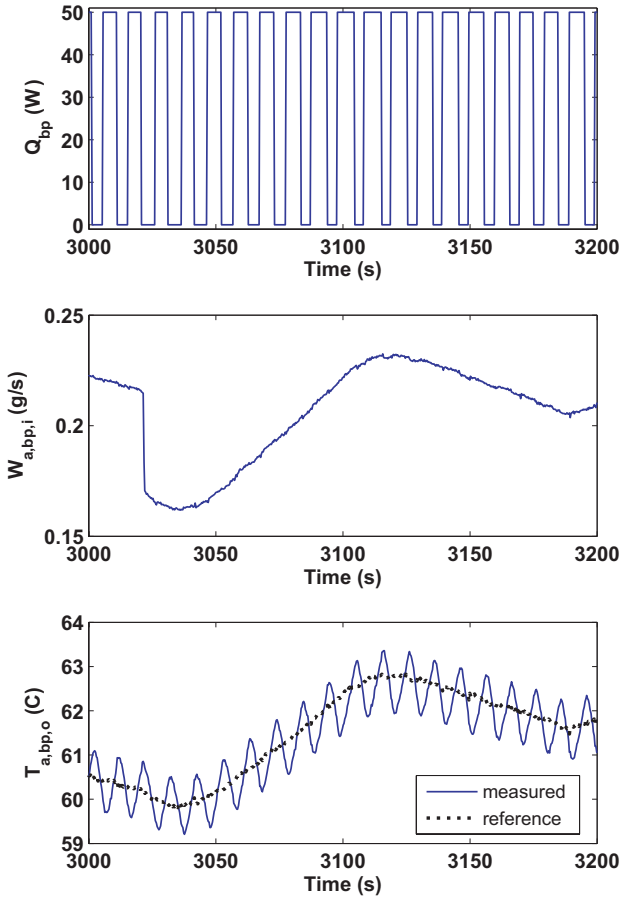

Figure 4.23: Bypass air outlet temperature thermostatic regulation during a step change in the desired cathode inlet temperature. The first subplot shows the bypass heater power, the second subplot shows the air mass flow rate supplied to the bypass using reference feedforward, and the third subplot shows the thermostatically regulated bypass air outlet temperature.

temperature responses during these changes in reference values along with a relatively large excursion in the ambient temperature due to cycling the room heater, a step change in the total air mass flow disturbance, and a reservoir fill event.

As expected the PI controller results in zero steady-state error. The overshoot and response time following step changes in reference temperature is approximately equal to the response the controller was tuned to achieve. Interestingly, the step in the reference (desired cathode inlet) temperature results in an increase in the air flow supplied to the humidifier, causing an initial decrease in the humidifier air outlet temperature which resembles a non-minimum phase response but is actually due to the difference in response times between the mass and thermal systems. Following the rapid 10^oC increase in ambient temperature, the humidifier air outlet temperature increased, requiring the humidifier heater power to decrease to regulate the humidifier air outlet temperature. The decrease in the total air mass flow rate disturbance resulted in a decrease in the air flow supplied to the humidifier, in turn increasing the humidifier air outlet temperature by approximately 1^oC.

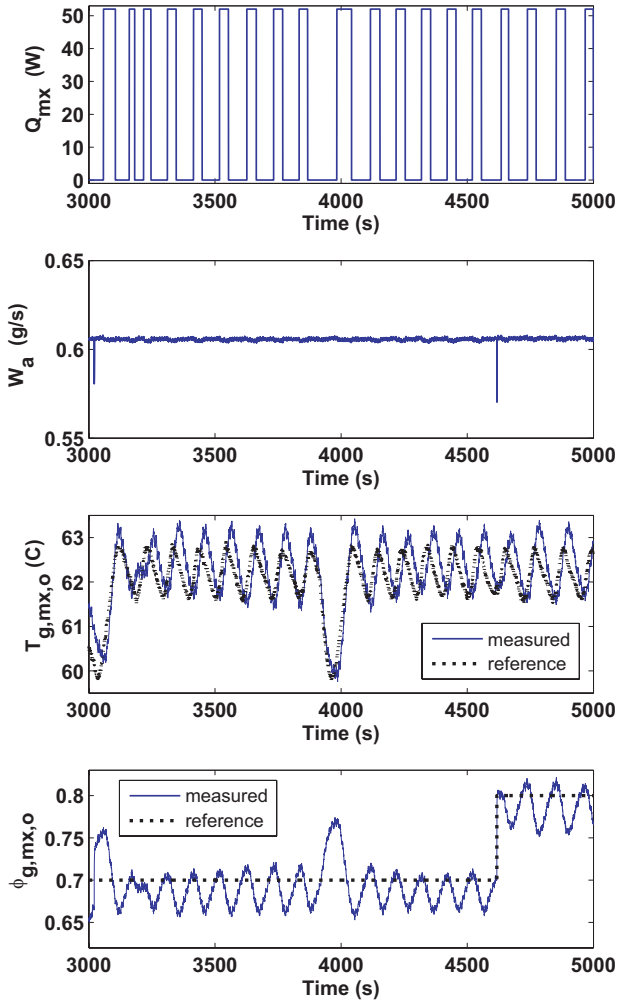

Figure 4.24: Mixer air outlet temperature thermostatic regulation during step changes in the reference temperature and the desired cathode inlet humidity. The first subplot shows the mixer heater power, the second subplot shows the total air mass flow rate disturbance, the third subplot shows the thermostatically regulated mixer air outlet temperature, and the fourth subplot shows the reference and estimated mixer outlet relative humidity.

The reservoir fill event, which injects cold water into the reservoir, causes a dramatic decrease in the humidifier air outlet temperature which saturates the water heater before reaching steady-state. Finally, the decrease in desired cathode inlet relative humidity results in a decrease in the air flow through the humidifier which increases the humidifier air outlet temperature.

Again, the intent of the bypass controller is to track the humidifier air outlet temperature. With the thermostatic regulation shown previously, the bypass temperature oscillated about the humidifier temperature. However, the bypass adequately tracks the humidifier air outlet temperature excursions well due to the difference in closed loop response times of these two systems. There is an insignificant difference between the bypass and humidifier air outlet temperatures throughout the experiment.

When the humidifier air outlet temperature initially decreases following the increase in the desired cathode inlet temperature, the mixer heater turns off and then proceeds to track the humidifier air outlet temperature. Because the closed loop mixer system response time is not as fast as the bypass, the mixer does not exactly track the humidifier air outlet temperature. However, the temperature tracking abilities are adequate. Additionally, the mixer outlet relative humidity is well regulated throughout the experiment.

Although the relative humidity at the mixer outlet is relatively well regulated with thermostatic control, the temperature oscillations may not be desirable depending upon the operating conditions of the PEMFC stack to which the air is supplied. To eliminate these oscillations, the proportional-integral (PI) controller is recommended to guarantee zero steady-state temperature error. However the added hardware complexity of a variable heater, in light of the potentially slower response time for small changes in the desired temperatures, may not justify use of PI control. If variable heaters are available with no cost or reliability penalty with respect to control implementation, then the PI controllers are recommended.

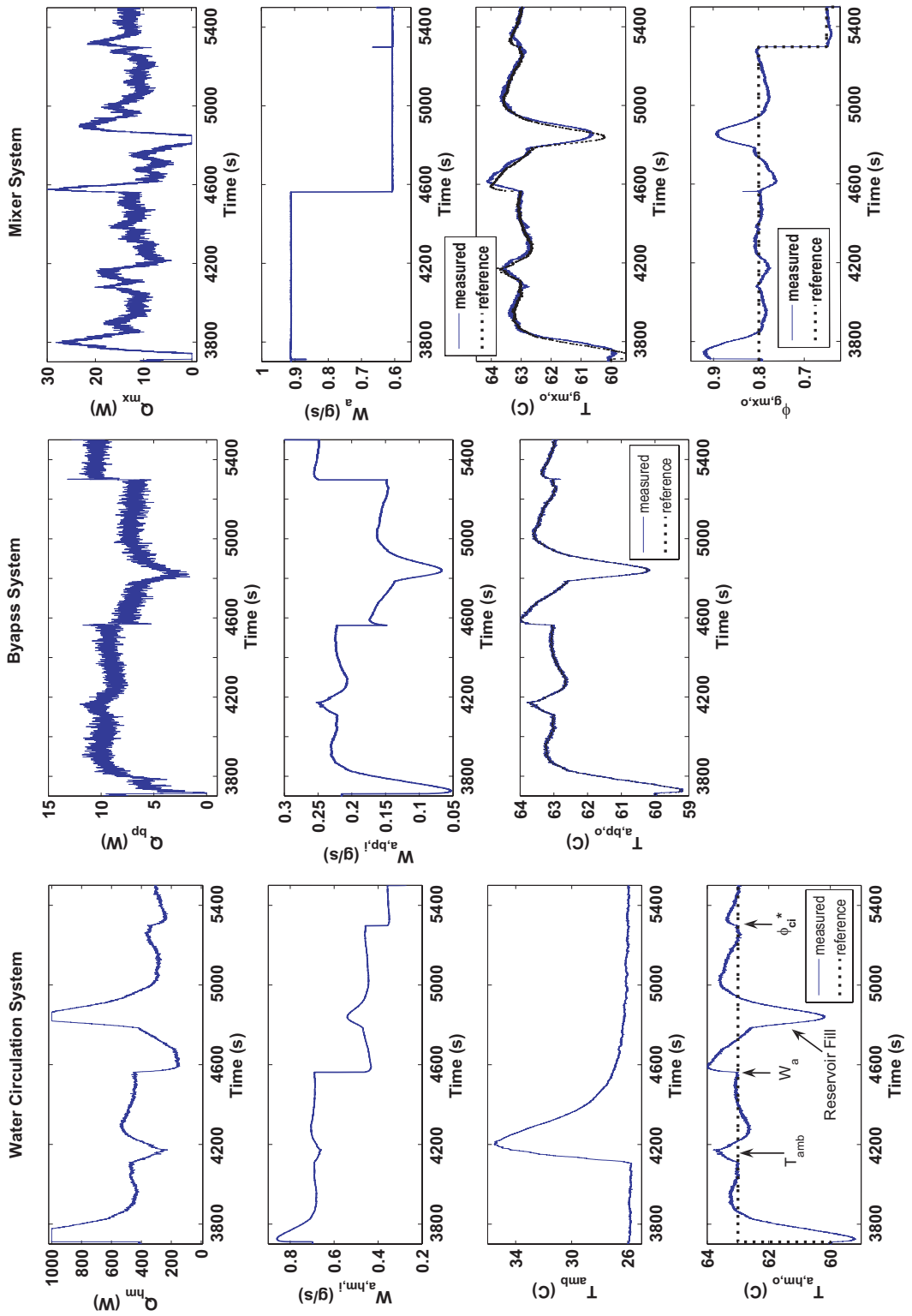

Figure 4.25: Humidification system response for PI regulation during step changes in the reference temperature, desired cathode inlet humidity, a reservoir fill event, and varying ambient temperature. Each column of subplots details the heater power, air mass flow rate disturbance, and regulated air outlet temperatures.

Chapter 5

Conclusions and Future Work

To actively manage water within the fuel cell, the influence of reactant and water dynamics on cell performance was quantified for a range of fuel cell operating conditions and a humidification apparatus was devised and controlled to regulate the amount of water vapor entrained in the gases supplied to the fuel cell. The dynamics of this gas humidification system were quantified to develop a control strategy capable of achieving the desired fuel cell inlet humidity conditions.

The application of first principles to these two different membrane-based systems was presented. Although the dynamics of interest are different for these two systems, motivating the application of a different set of assumptions in model development, a similar model calibration, experimental identification and validation process was employed. The models were calibrated using published properties, such as the specific heat of air; material properties, such as the membrane dry density; and geometric relations, such as the manifold volume. An appropriate cost function, where the model output used in the cost function can be directly measured, was then devised to identify the remaining model parameters by minimizing the estimation error. Using a wide range of typical operating conditions, the models were experimentally validated by directly comparing the dynamic response of modeled outputs to the measured variables.

5.1 Fuel Cell Reactant and Water Dynamics

A two-phase, one-dimensional (through the gas diffusion layer) model for a multi-cell stack was developed and validated using experimental transient data. The lumped parameter model depends on six tunable parameters that influence the voltage estimation. Two of these parameters, associated with the water exchanged between the cathode and anode through the membrane and the sensitivity of voltage to the liquid water accumulation in the anode channel, appear nonlinearly; whereas, the remaining four voltage parameters appear linearly and can be explicitly determined for a given set of water related parameters. As a result, an iterative tuning parameter tuning process involves the repeated calculation of the voltage parameters for varying values of the water related parameters until an optimal solution is attained.

During step changes in load, a good voltage prediction is achieved by reproducing both the steady-state and dynamic voltage response due to the instantaneous increase in current as well as

the excursions in oxygen partial pressure resulting from the manifold filling dynamics, as demonstrated. Finally the model predicted the dynamic effect of temperature on voltage as shown during the temperature transient from 50^o to 60^oC. Although simple, this model captures the voltage dynamics observed in a fuel cell stack at low and moderate current densities during anode flooding under the range of conditions tested. However, caution should be used in extending this model to conditions not examined, as the intent of this model is for estimation and control of fuel cell water and gas dynamics. The unique contributions of this work were in relating anode water flooding to the resultant dynamic voltage degradation; determining that a low-order, isothermal, lumped parameter model suitable for control applications could approximate the dynamic fuel cell response under a range of operating conditions; and developing a simple and reproducible stack-level tuning methodology leveraging standard off-the-shelf sensors and actuators.

5.2 Gas Humidification System

The elimination of a bulky and expensive humidity sensor was achieved by employing an estimator to predict the relative humidity dynamics of the air-vapor mixture leaving the humidifier system (supplied to the PEMFC). Experimental results showed that with accurate measurements of temperature, the dynamic response of relative humidity was adequately estimated under a range of operating conditions typical for this system. Moreover, these results indicated that the mixer outlet gas relative humidity can be accurately controlled if temperature is well regulated. As a result, the thermal dynamics of the various control volumes, related time constants, and impact of the operating conditions on the thermal response were characterized to generate an accurate estimation of gas temperatures for the purpose of coordinating the system thermal inputs to achieve the desired gas humidity level.

To achieve an understanding of the humidification system thermal dynamics with the intent of controller development, a physics based, low-order, lumped parameter model was developed and experimentally validated to regulate both PEMFC cathode inlet temperature and relative humidity. This model accurately estimated the thermal response of each of the system control volumes during changes in the air mass flow rate and heat injection. As expected, overshoot in the bypass temperature resulted in an undershoot in the cathode inlet relative humidity. Conversely, overshoot in the humidifier temperature, when not tracked by the bypass temperature, resulted in overshoot in the cathode inlet temperature, creating condensate.

Employing the experimentally validated model of the system thermal dynamics, controllers were designed and tuned to coordinate the humidification system thermal injections and the fraction of air supplied to the humidifier. Due to the cascaded nature of the humidification system, the dynamics of the mixer and bypass control volumes were analyzed separately from the water circulation system control volumes (including the reservoir, water heater and humidifier). The bandwidth separation associated with the system responses results in a limitation on the reference temperatures employed for thermal regulation. Requiring the mixer and bypass to track the humidifier air

dynamics results in a slower thermal response but well regulated humidity conditions.

The control architecture utilizes either thermostatic or proportional-integral (PI) controllers for thermal regulation and a static nonlinear feedforward map to control the mass fractional split of air between the humidifier and bypass. For constant disturbances, the humidification system dynamics are approximately linear and therefore, linear control theory was applied for controller design. As expected, thermostatic control of the humidifier system, tuned by employing a describing function methodology, resulted in significant temperature and relative humidity limit cycle oscillations. PI control, however, allowed for adequate control of both temperature and humidity with zero steady-state temperature error, while satisfactorily minimizing excursions in temperature following changes in the disturbances. Therefore a clear tradeoff exists between steady-state thermal regulation and hardware and controller simplicity, a critical consideration for automotive applications.

The unique contributions of this gas humidification system effort includes designing an apparatus that enables independent control of temperature and humidity of the reactant gases supplied to the PEMFC stack; developing a physics based model of the gas humidification system for controller tuning; composing a control strategy for simultaneously achieving thermal and humidity regulation; eliminating reliance on a humidity sensor by constructing an accurate humidity estimator; and providing a tuning methodology and thorough comparison of the use of on/off versus variable gas heaters in achieving thermal regulation.

5.3 Extensions of this Thesis

Based on the results of this work, there are several areas of future study that warrant consideration, as detailed below. Additionally, this work can be extended to examine system dynamics with similar time scales and sensor and actuator constraints.

5.3.1 Fuel Cell Modeling and Validation

Although the model of fuel cell reactant and water dynamics results in an accurate estimation of the voltage degradation between purges, we have made the assumption in this work that this degradation was solely due to the accumulation of liquid water in the anode gas channels. However, it is conceivable that some of this degradation could be due to the accumulation of nitrogen on the anode as a result of operation with air, rather than pure oxygen. Our model has tunable parameters that can compensate for these unmodeled dynamics and simplifying assumptions, and as Table 2.3 shows, the tuned α_w and t_{wl}, are reasonable and within the range of published results [10, 56]. It is thought that the impact of nitrogen on voltage degradation would be relatively constant due to the range of current densities (0-0.3A/cm^2) and air stoichiometries (200-300%) considered. However, for extensions to a wider range of operating conditions, these voltage degradation mechanisms should be clearly quantified.

Although the apparent current density calculation based on the water accumulation in the anode channels approximates the cell voltage behavior well during a range of transient and steady

conditions the stack typically operates in, more experimental evidence and justification of this simplification is needed if operation is expected to occur under a wider range of humidity conditions. The notion of apparent current density is a means for describing the impact of liquid water accumulation on the dynamic voltage behavior of a PEMFC. Future work is focused on extending and validating this simple GDL model at higher current density, and directly establishing the connection between the liquid water mass accumulation and voltage using neutron imaging techniques [62]. Although neutron imaging is not an applicable technique for rapid and cheap model calibration, it is appropriate for model validation on classes of material structures.

We have made the simplifying assumption that no liquid water leaves the electrodes, implying water is only carried from the gas channels in the vapor phase. Other authors [14] have forced all liquid water in the anode gas channel following a purge to be removed. However, their requirement does not allow for a non-complete voltage recovery between purges, where the voltage immediately following subsequent purging events continually decreases due to liquid water remaining in the gas channels and manifolds following purge events. If future work compares not only modeled and measured cell voltage, but also liquid water mass in the gas channels, the effect of dynamic liquid water removal from the gas channels should be considered.

For model simplicity with respect to the number of modeled states, we have assumed that the cell materials are in thermal equilibrium with the coolant water leaving the stack. Due to the coupling between water and thermal dynamics, through the water vapor saturation pressure, future work could consider the impact of a thermal gradient on the condensation and evaporation dynamics. However, care should be taken when adding complexity to the model due the implications on subsequent model order reduction, controllability and observability work [39] as well as controller development.

5.3.2 Humidification System

In this thesis, the mass flow rate of liquid water through the humidification water circulation system was assumed to be fixed, set by the position of a manual throttle valve. However, to increase the thermal response time of the water circulation system, the liquid water mass flow rate could be regulated either by an actuated throttle valve, or a pump motor controller. This modification would require an additional analog output signal and add controller complexity.

For regulating the relative humidity of the air-vapor mixture supplied to the PEMFC, a static nonlinear feedforward map was employed. During transients, when the desired relative humidity was not achieved, no additional compensation was used. Relative humidity feedback control could be considered; however, care should be taken in balancing the tradeoff between humidity and thermal regulation since varying the air mass flow rate through the humidifier or bypass has a significant impact on the system thermal response.

5.3.3 Extensions to Other Applications

The methodology used here, employing input-output measurements to develop and validate physics based models of system dynamics for controller design and tuning, could be applied to a variety of applications including membrane-based systems, such as electrolyzers which are receiving increased attention as viable hydrogen gas generators for fuel cell applications and bio-reactors for wastewater treatment; electrochemical processes, such as battery hybrid systems; humidity regulation, common in a variety of applications including agricultural production; and active solar thermal systems exhibiting similar operating conditions and bandwidth separation. Although the simplifying assumptions for these systems would be different than those employed here, especially for extensions to high pressure, these processes exhibit similar sensor and actuator constraints.

Appendices

Appendix A

Fuel Cell Orifice Constants

The fuel cell cathode orifice constant were identified using experimental back-pressure flow data gathered by varying the fuel cell load level at a given air stoichiometry and measuring the cathode inlet and outlet total pressures. Note, this relationship could also be determined at open circuit by varying the air mass flow rate manually. Figure A.1 shows experimental data detailing both the total air mass flow rate and the pressure drop between the cathode inlet and gas channel. The fluctuations in pressure at a given air mass flow rate are due to the fuel cell coolant temperature cycling.

To estimate the cathode channel pressure, since no direct measurement is available, it is first assumed that the cathode channel pressure, $p_{ca}(L+1)$, is a linear average between the inlet and outlet total pressures, $p_{ca,in}$ and $p_{ca,out}$, such that

$$p_{ca}(L+1) = \frac{p_{ca,in} + p_{ca,out}}{2} \ . \tag{A.1}$$

For an isothermal cell, this linear pressure distribution assumption implies that the cathode inlet and outlet orifice constants will be equal. For a linear orifice, the total gas mass flow rate, $W_{ca,in}$, supplied to the cathode is a function of the pressure drop by,

$$W_{ca,in} = k_{ca}(p_{ca,in} - p_{ca}(L+1)) \ , \tag{A.2}$$

where k_{ca} is the orifice constant requiring experimental identification. By substitution of Equation A.1, this back-pressure flow relationship can be expressed in terms of the measureable pressure drop as:

$$W_{ca,in} = 0.5k_{ca}(p_{ca,in} - p_{ca,out}) \ . \tag{A.3}$$

Knowing the humidity conditions at the cathode inlet, the vapor mass flow rate can be calculated using psychrometric properties where $W_{v,ca,in} = \omega_{ca,in} W_{da,ca,in}$. Additionally, assuming that half of the total loss of oxygen, due to the chemical reaction under load, occurs between the inlet and the middle of the cathode gas channel, the orifice constant is expressed as

$$k_{ca} = \frac{2W_{da,ca,in} - W_{O_2,ca}(0) + 2W_{v,ca,in}}{p_{ca,in} - p_{ca,out}} \ . \tag{A.4}$$

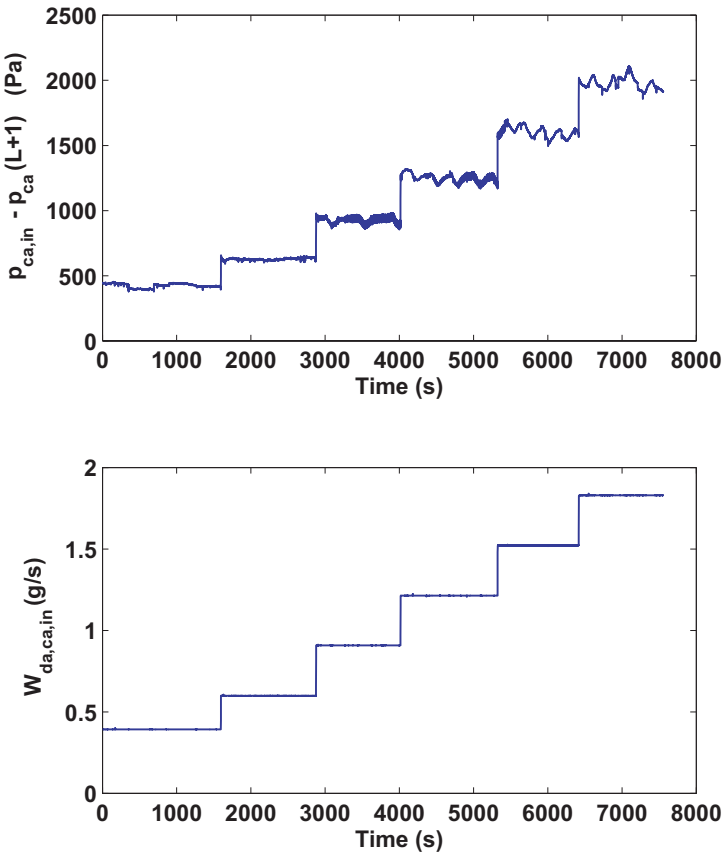

Figure A.1: Experimental back-pressure flow data used to tune the cathode orifice constant. The first subplot shows the difference in pressure between the cathode inlet and the cathode gas channel. The second subplot shows the total dry air mass flow rate supplied to the cathode gas channel.

For the experimental data shown in Figure A.1, the average cathode orifice constant was found to be k_{ca}=1.13x10^{-6} (m s). The estimated and measured back-pressure flow relationship is compared in Figure A.2. The relationship between back-pressure and flow is approximately linear under this range of operating conditions, resulting in a satisfactory estimate with an average estimation error of 0.035 g/s (3.9% of the dry air mass flow rate).

Due to the physical constraints associated with a pressure-regulated anode, the anode orifice constants were not approximated using experimental data. Instead, it was assumed that the anode and cathode channels resulted in similar restrictions. However, under some conditions, this orifice constant resulted in supersonic flow on the anode during purge events. As a result, the anode orifice constant was reduced until supersonic flow no longer occurred. The resulting anode orifice constant was found to be k_{an}=9.34x10^{-7} (m s), a 20% reduction from the cathode orifice constant.

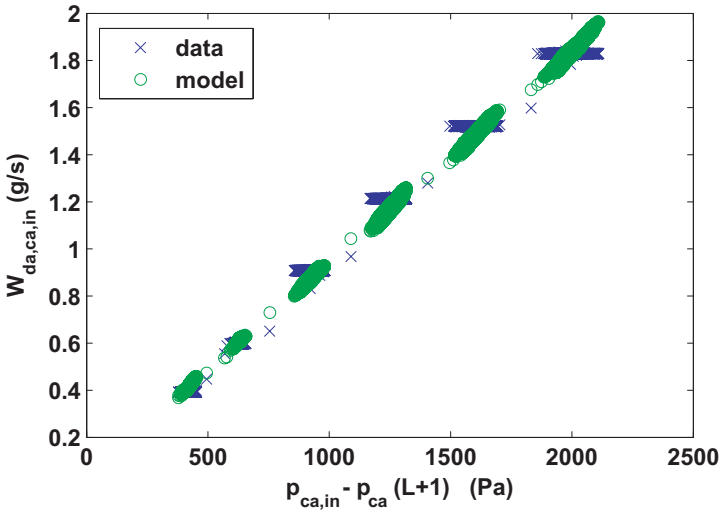

Figure A.2: Comparison of the experimental and modeled back-pressure flow relationship for the cathode channel.

Appendix B

A Review of Back Diffusion Models

The information in this appendix provides a literature review of the membrane water vapor mass transport models used to describe back diffusion.

Back Diffusion Flux

There are three commonly modeled mechanisms for back diffusion, namely Fickian diffusion and combinations of Fickian and convective diffusion. The use of humidified gases as well as the production of water at the cathode results in a water vapor concentration gradient, $[c_{v,ca,mb} - c_{v,an,mb}]/t_{mb}$, across the membrane thickness, t_{mb}. Additionally, a difference in the total or water pressure in the electrodes results in a pressure gradient across the membrane thickness $[(P_{ca}(1) - P_{an}(1)]/t_{mb}$ or $[P_{w,ca}(1) - P_{w,an}(1)]/t_{mb}$. The concentration and pressure gradients result in a diffusion of water through the membrane, referred to as back diffusion. The magnitude and direction of the net vapor flow through the membrane (anode to cathode or cathode to anode) are a function of the relative magnitudes of back diffusion and electroosmotic drag.

A model used extensively [16, 42, 49, 65, 77] for characterizing the flux of water vapor through the membrane due to back diffusion assumes Fickian diffusion with no water or total pressure gradients in the electrodes, described by:

$$N_{v,mb,diff} = - D_w^F \frac{(c_{v,ca,mb} - c_{v,an,mb})}{t_{mb}} \tag{B.1}$$

where D_w is used to denote the membrane water vapor Fickian diffusion coefficient.

When a significant water pressure gradient is present between the anode and the cathode, an additional convective flow of water should be considered. As discussed in [15] and [77], assuming Fickian diffusion to characterize the water concentration gradient (as previously described for Equation B.1), along with the application of Darcy's Law, the back diffusion water vapor transport across the membrane can be described by

$$N_{v,mb,diff} = - D_w \frac{(c_{v,ca,mb} - c_{v,an,mb})}{t_{mb}} + \frac{k_p c_{v,mb}}{\mu} \frac{(P_{w,ca,mb} - P_{w,an,mb})}{t_{mb}} \tag{B.2}$$

where k_p is the permeability of water in the membrane and μ is the water viscosity.

An alternative description for the convective transport of water through the membrane was presented by [12]. This model, applying Darcy's Law for flow through porous media and accounts for the total electrode pressure difference as the convective driving force rather than the water pressure, is characterized by

$$N_{v,mb,diff} = -D_w \frac{(c_{v,ca,mb} - c_{v,an,mb})}{t_{mb}} + \frac{3k_p c_{v,mb} \pi\theta (P_{ca,mb} - P_{an,mb})}{k_b T_{mb} t_{mb}} \tag{B.3}$$

where k_b is the Boltzmann constant and θ is the diameter of a water molecule.

Water Uptake Isotherms

Zawodzinski et al [80] equilibrated Nafion 117 membranes with aqueous LiCl solutions of known water activity at 30^{o}C. The membrane hydration state was controlled via isopiestic equilibration. By varying water activity, an isopiestic sorption curve was measured. Based on these experimental results, a model was then developed [65] as follows:

$$\lambda = 0.043 + 17.81a - 39.85a^2 + 36.0a^3, \tag{B.4}$$

where λ is defined as the membrane water content also referred to as the water content per charge site (H_2O/SO_3^-) and a is the water activity defined in [65] as:

$$a = \frac{x_w P}{P_{sat}}, \tag{B.5}$$

where x_w is the mole fraction of water[1], P is the total pressure, and P_{sat} is the water vapor saturation pressure.

Hinatsu et al [24] then measured both liquid and vapor water uptake in several perfluorosulfonic acid membranes of various thickness under a much wider range of temperatures than that used by [80]. Hinatsu measured water uptake via displacement by placing the sample in a basket on a spring. The sample was held at constant pressure with a vacuum system and constant temperature using a silicon oil circulation system in the housing of the apparatus. Water uptake was then carefully examined by controlling the relative humidity (vapor pressure) of air in contact with the membrane. Their work resulted in the following sorption curve at 80^{o}C,

$$\lambda = 0.300 + 10.8a - 16.0a^2 + 14.1a^3, \tag{B.6}$$

which provided a good fit of the experimental data for several membranes of various thicknesses, including Nafion 117.

Because these works ([80] and [24]) resulted in different sorption curves at two different tem-

[1] Experimental work was conducted with water in the vapor phase.

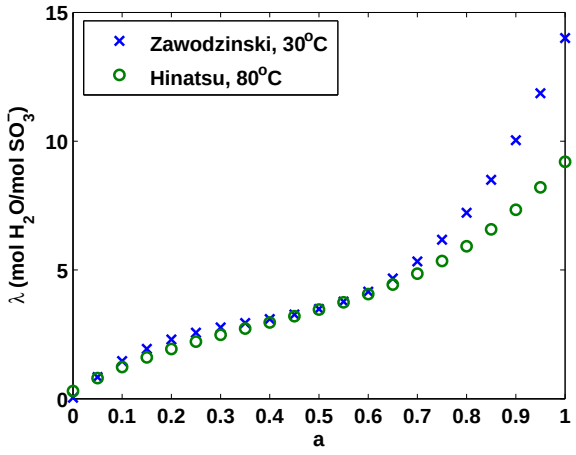

Figure B.1: Comparison of water sorption curves for Nafion 117 at 80^{o}C and 30^{o}C.

peratures, Dannenberg et al [13] performed a numerical interpolation for temperatures other than those under which the experiments were conducted. Specifically, for a given water activity, the water contents were calculated at 30^{o}C and 80^{o}C using the models presented in both [80] and [24], and interpolated to a different temperature between these bounds. It is important to note that this methodology was not confirmed with experiments.

Water Vapor Diffusion Coefficient

Springer et al, [65], based on the experimental work by [80], published a detailed model for the water vapor diffusion flux through a perflourinated ionomeric membrane. The model was experimentally calibrated using a pulsed-field gradient spin-echo nuclear magnetic resonance technique at 30^o C. The modeling and experimental work completed by Springer et al has been modified extensively to fit experimental data for cell assemblies of differing materials. Their work presents an isothermal, isobaric, one dimensional steady-state model of vapor diffusion in a cell utilizing Nafion® 117 membranes for $\lambda > 4$:

$$D_w = 10^{-10} exp\left[2416\left(\frac{1}{303} - \frac{1}{T_{mb}}\right)\right](2.563 - 0.33\lambda + 0.0264\lambda^2 - 0.000671\lambda^3)\,. \qquad \text{(B.7)}$$

The definition for water activity and water content shown in Equations B.5 and B.4 were employed. Due to the constant temperature and pressure testing conditions, their model accounts for Fickian diffusion and no convective diffusion. Although their model includes the presence of liquid water, their experimental results concentrated on the modeling of diffusion with no liquid water formation in the electrodes (sub-saturated conditions). To allow for an extension of their model to account for the accumulation of liquid water, they assume that any condensation forms in finely dispersed droplets that occupy no volume.

Dutta et al, [16], utilized Springer's published experimental data of the dependency of the dif-

fusion coefficient on the membrane water content and presented a piecewise linear approximation to the experimental data given by Springer in [65]. The resulting model is:

$$D_w = D_\lambda exp\left(2416\left(\frac{1}{303} - \frac{1}{T_{cell}}\right)\right) \tag{B.8}$$

(B.9)

$$D_\lambda = \begin{cases} 10^{-10} & ,\lambda < 2 \\ 10^{-10}(1+2(\lambda-2)) & ,2 \leq \lambda \leq 3 \\ 10^{-10}(3-1.67(\lambda-3)) & ,3 < \lambda < 4.5 \\ 1.25 \cdot 10^{-10} & ,\lambda \geq 4.5 \end{cases}$$

where D_λ is the corrected diffusion coefficient (m^2/s). Although this model allows for the accumulation of liquid water in the electrodes, it should be used with caution, as the experimental data gathered by Springer to formulate the model was taken under subsaturated conditions in the electrodes.

Fuller, [19] determined the water vapor diffusion coefficient for Nafion® 117 membranes by equilibrating a membrane with liquid, supplying a continuous flow of nitrogen across the surface of the membrane, and performing a water vapor mass balance. Using the water sorption curve from Zawodzinski et al [80] in Equation B.4, the following estimation of the diffusion coefficient was made,

$$D_w = 3.5 \cdot 10^{-6}\left(\frac{\lambda}{14}\right) exp\left[\frac{-2436}{T_{mb}}\right]. \tag{B.10}$$

Rodatz [56] assumed both Fickian and convective diffusion of vapor through the membrane based on the work presented by Yi and Nguyen [77] (shown in Equation B.2), used the description for the relationship between water content and water activity posed by Dannenberg et al [13] producing different sorption curves at different temperatures, and then added a tunable scaling factor, D_o, to the vapor diffusion equation described by Springer et al in Equation B.7. Finally, Rodatz parameterized the equation using experimental data to minimize the difference between a fuel cell system model predicted cell voltage and the measured cell voltage. The D_o coefficient, for a 6kW HyPower fuel cell vehicle, was found to be 5.3x10^{-11} m^2/s, rather than the 1.0x10^{-10} m^2/s published by Springer et al.

$$\begin{aligned} D_w =& D_o exp\left[2416\left(\frac{1}{303} - \frac{1}{T_{cell}}\right)\right] \\ & (2.563 - 0.33\lambda + 0.0264\lambda^2 - 0.000671\lambda^3) \end{aligned} \tag{B.11}$$

Yamada et al, [76], determined the water vapor diffusion coefficient for a 1 cm^2 single cell con-

structed of Nafion® 112 membranes, ETek ELATs, and catalyst loadings of 0.1 mg Pt/cm^2 and 0.4 mg Pt/cm^2 on the anode and cathode, respectively. Yamada employed mass balances at open circuit, assumed Fickian diffusion of water vapor through the membrane, and fit a new basis function for the vapor diffusion coefficient using the water uptake isotherm and definition of water activity published by [65] and [80] and described in Equations B.4 and B.5. The following isothermal model for the diffusion coefficient was found.

$$D_w = \begin{cases} 6.00 \cdot 10^{-12} exp(1.63\lambda), & \lambda < 3 \\ \\ 5.13 \cdot 10^{-9} \left[exp(-0.708\lambda) + 0.0339 \right], & \lambda \geq 3 \end{cases} \tag{B.12}$$

Motupally et al, [42], modified the work completed by [80] and [65] to present a revised model of the membrane water vapor diffusion coefficient. The water uptake isotherm in Equation B.4 was modified to instantaneously increase the membrane water content from $\lambda = 14$ to $\lambda = 17$ when water vapor condenses ($a \geq 1$). Additionally, the "Darken factor" was used to relate the intra and Fickian diffusion coefficients presented by [65] accounting for the transport number of electrons being 0 at open circuit. The resulting Fickian diffusion coefficient was finally corrected using the enthalpy of diffusion to allow for temperatures different than the results published by [80] at 30^{o}C. The final water vapor diffusion coefficient model:

$$D_w = \begin{cases} 3.10 \cdot 10^{-7} \lambda \left[-1 + exp(0.38\lambda) \right] exp\left(\frac{-2436}{T_{mb}} \right), & 0 < \lambda \leq 3 \\ \\ 4.17 \cdot 10^{-8} \lambda \left[1 + 161 exp(-\lambda) \right] exp\left(\frac{-2436}{T_{mb}} \right), & 3 \leq \lambda < 17 \end{cases} \tag{B.13}$$

was compared to experimental results using a 50cm^2 cell constructed of Nafion® 115 membranes, and ETEK®gas diffusion layers. A similar experimental apparatus and procedure as cited by Fuller et al [19] was used to perform a vapor mass balance on one electrode (with the membrane equilibrated with liquid water) using nitrogen as the carrier gas. The tests were conducted at a constant 80^{o}C.

A summary of these models is provided in Figure B.2. The first subplot displays the diffusion coefficients as a function of the water activity at a constant temperature of T_{cell} = 333.15 K. The second subplot shows the diffusion coefficients as a function of the cell temperature at a constant water activity of $a = 0.7$.

Note, due to the constraint imposed on Equation B.7, the diffusion coefficient is not plotted for $a < 0.6$ ($\lambda > 4$) for either the "Springer" or the "Rodatz" models. The model used by "Rodatz" is a shifted (by D_o) version of the model originally introduced by Springer. Thus, the results of these two models are quite similar. Interestingly, the model presented by "Dutta" was intended to be a linear piece-wise approximation of the work presented by "Springer", yet exhibits entirely different trends with respect to the water activity at this temperature. The models presented by "Yamada", "Springer", and "Rodatz" all predict that the diffusion coefficient will decrease with respect

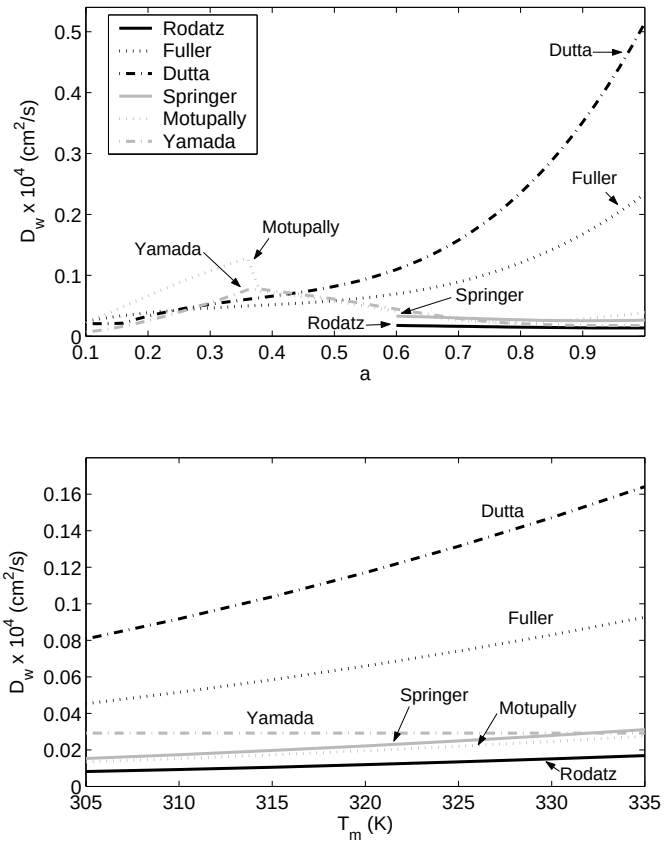

Figure B.2: Summary of published water vapor diffusion coefficient models.

to the water activity for $a > 0.6$. Whereas "Fuller" and "Dutta" predict the diffusion coefficient will monotonically increase for all water activities where $a < 1$. "Motupally's" model shows an increasing diffusion coefficient at low and high water activities, however, decreasing between $0.35 < a < 0.8$, quite similar to the graphical depiction originally provided by [65]. Additionally, all models depict the diffusion coefficient increasing with respect to the cell temperature, except "Yamada's" isothermal model.

Bibliography

[1] J.C. Amphlett, R.M. Baumert, R.F. Mann, B.A. Peppley, and P.R. Roberge. Performance modeling of the ballard mark iv solid polymer electrolyte fuel cell, i. mechanistic development. *Journal of the Electrochemical Society*, 142, 1995.

[2] K.J. Astrom and B. Wittenmark. *Computer Controlled Systems, Theory and Design*. Prentice Hall Information and System Sciences Series, 1990.

[3] F. Barbir. *PEM Fuel Cells: Theory and Practice*. Elsevier, Burlington, Ma, 2005.

[4] P. Berg, K. Promislow, J.St. Pierre, J. Stumper, and B. Wetton. Water management in pem fuel cells. *Journal of the Electrochemical Society*, 151(3), 2004.

[5] T. Berning and N. Djilali. A 3d, multiphase, multicomponent model of the cathode and anode of a pem fuel cell. *Journal of the Electrochemical Society*, 150(12):A1589–A1598, 2003.

[6] B. Carnes and N. Djilali. Systematic parameter estimation for pem fuel cell models. *Journal of Power Sources*, 144:83–93, 2005.

[7] Carrette, Friedrich, and Stimming. *Fuel Cells - Fundamentals and Applications*. Wiley InterScience, 2001.

[8] D. Chen and H. Peng. A thermodynamic model of membrane humidifiers for pem fuel cell humidification control. *Transaction of the ASME, Journal of Dynamic Systems, Measurement and Control*, 127:424–432, 2005.

[9] K.H. Choi, D.J. Park, Y.W. Rho, Y.T. Kho, , and T.H. Lee. A study of the internal humidification of an integrated pemfc stack. *Journal of Power Sources*, 74:146–150, 1998.

[10] P.-Y. A. Chuang, A. Turhan, A. K. Heller, J. S. Brenizer, T. A. Trabold, and M. Mench. The nature of flooding and drying in polymer electrolyte fuel cells. *Proceedings of the ASME 2ND International Conference on Fuel Cell Science, Engineering and Technology*, 2005.

[11] E. Cortona, C.H. Onder, and L. Guzzella. Engine thermomanagement with electrical components for fuel consumption reduction. *IMechE Int. Journal of Engine Research*, 3(3):157–170, 2002.

[12] P. Costamagna. Transport phenomena in polymeric membrane fuel cells. *Chemical Engineering Science*, 56:323–332, 2001.

[13] K. Dannenberg, P. Ekdunge, and G. Lindbergh. Mathematical model of the pemfc. *Journal of Applied Electrochemistry*, 30:1377–1387, 2000.

[14] A.J. del Real, A. Arce, and C. Bordons. Development and experimental validation of a pem fuel cell dynamic model. *Journal of Power Sources*, 2007.

[15] N. Djilali and D. Lu. Influence of heat transfer on gas and water transport in fuel cells. *International Journal of Thermal Science*, 41:29–40, 2002.

[16] S. Dutta, S. Shimpalee, and J.W. Van Zee. Numerical prediction of mass-exchange between cathode and anode channels in a pem fuel cell. *International Journal of Heat and Mass Transfer*, 44:2029–2042, 2001.

[17] J. Freudenberg. *A First Graduate Course in Feedback Control*. University of Michigan, EECS 565 Coursepack, 2005.

[18] T. Fuller and J. Newman. Water and thermal management in solid-polymer-electrolyte fuel cells. *Journal of the Electrochemical Society*, 140(5), 1993.

[19] T.F. Fuller. *Solid polymer-electrolyte Fuel Cells*. PhD thesis, University of California, Berkeley, 1992.

[20] Q. Guo, V.A. Sethuraman, and R.E. White. Parameter estimates for a pemfc cathode. *Journal of the Electrochemistry Society*, 151(7):A983–A993, 2004.

[21] C.C. Hang, K.J. Astrom, and Q.G. Wang. Relay feddback auto-tuning of process controllers - a tutorial review. *Journal of Process Control*, 12(1), 2002.

[22] A. Hernandez, D. Hissel, and R. Outbib. Nonlinear state space modeling of a pemfc. *Fuel Cells*, 06(1):38–46, 2005.

[23] M.A. Hickner, N.P. Siegel, K.S. Chen, D.N. McBrayer, D.S. Hussey, D.L. Jacobson, and M. Arif. Real-time imaging of liquid water in an operating proton exchange membrane fuel cell. *Journal of the Electrochemical Society*, 153:A902–A908, 2006.

[24] J. Hinatsu, M. Mizuhata, and H. Takenaka. Water uptake of perfluorosulfonic acid membranes from liquid water and water vapor. *Journal of the Electrochemical Society*, 141:1493–1498, 1994.

[25] H. Ju and C.Y. Wang. Experimental validation of a pem fuel cell model by current distribution data. *Journal of the Electrochemical Society*, 151(11):A1954–A1960, 2004.

[26] H. Ju, C.Y. Wang, S. Cleghorn, and U. Beuscher. Nonisothermal modeling of polymer electrolyte fuel cells. *Journal of the Electrochemical Society*, 152:A1645–A1653, 2005.

[27] A.Y. Karnik, A.G. Stefanopoulou, and J. Sun. Water equilibria and management using a two-volume model of a polymer electrolyte fuel cell. *Journal of Power Sources*, 164:590–605, 2007.

[28] M. Kaviany. *Principles of Heat Transfer in Porous Media, second ed.* Springer, New York, 1999.

[29] M. Kaviany. *Principles of Heat Transfer*. John Wiley and Sons, New York, 2002.

[30] H. Khalil. *Nonlinear Systems*. Prentice Hall, 2002.

[31] S.S. Kocha, J.D. Yang, and J.S. Yi. Characterization of gas crossover and its implications in pem fuel cells. *AIChE*, 52(5):1916–1925, 2006.

[32] D. Kramer, J. Zhang, R. Shimoi, E. Lehmann, A. Wokaun, K. Shinohara, and G.G. Scherer. In situ diagnostic of two-phase flow phenomena in polymer electrolyte fuel cells by neturon imaging part a. experimental, data treatment, and quantification. *Electrochimica Acta*, 50:2603–2614, 2005.

[33] E.C. Kumbur, K.V. Sharp, and M.M. Mench. Liquid droplet behaviour and instability in a polymer electrolyte fuel cell flow channel. *Journal of Power Sources*, 161:333–345, 2006.

[34] B. Kuo and F. Golnaraghi. *Automatic Control Systems*. John Wiley and Sons, Inc., 2003.

[35] J. Laraminie and A. Dicks. *Fuel Cell Systems Explained*. Wiley InterScience, 2003.

[36] G. Lin, W. He, and T.V. Nguyen. Modeling liquid water effects in the gas diffusion and catalyst layers of the cathode of a pem fuel cell. *Journal of The Electrochemical Society*, 151(12):A1999–A2006, 2004.

[37] S. Litster, D. Sinton, and N. Djilali. Ex situ visualization of liquid water transport in pem fuel cell gas diffusion layers. *Journal of Power Sources*, 154:95–105, 2006.

[38] A. Love, S. Middleman, and A.K. Hochberg. The dynamics of bubblers as vapor delivery systems. *Journal of Crystal Growth*, 129:119–133, 1993.

[39] B.A. McCain and A.G. Stefanopoulou. Order reduction for a control-oriented model of the water dynamics in fuel cells. In *Proceedings of 4th International Conference on Fuel Cell Science, Engineering and Technology*, volume FUELCELL2006-97075, 2006.

[40] D.A. McKay, W.T. Ott, and A.G. Stefanopoulou. Modeling, parameter identification, and validation of water dynamics for a fuel cell stack. In *Proceedings of 2005 ASME International Mechanical Engineering Congress & Exposition*, volume IMECE 2005-81484, Nov 2005.

[41] R. Middleton and S. Graebe. Slow stable open-loop poles: to cancel or not to cancel. *Automatia*, 35:877–886, 1999.

[42] S. Motupally, A. Becker, and J. Weidner. Diffusion of water in nafion 115 membranes. *Journal of The Electrochemical Society*, 147(9), 2000.

[43] E.A. Mueller and A.G. Stefanopoulou. Analysis, modeling, and validation for the thermal dynamics of a polymer electrolyte membrane fuel cell sytems. *Proceedings of the ASME 3rd International Conference on Fuel Cell Science, Engineering and Technology*, FUELCELL2005-74050, 2005.

[44] J.H. Nam and M. Kaviany. Effective diffusivity and water-saturation distribution in single and two-layer pemfc diffusion medium. *International Journal of Heat and Mass Transfer*, 46:4595–4611, 2003.

[45] D. Natarajan and T.V. Nguyen. A two-dimensional, two-phase, multicomponent, transient model for the cathode of a proton exchange membrane fuel cell using conventional gas distributors. *Journal of The Electrochemical Society*, 148(12):A1324–A1335, 2001.

[46] D. Natarajan and T.V. Nguyen. Curent distribution in pem fuel cells. part 1: Oxygen and fuel flow rate effects. *AIChE Journal*, 51(9):2587–2598, 2005.

[47] K. Ogata. *System Dynamics*. Prentice Hall, 1998.

[48] R.P. O'Hayre, S.W. Cha, W. Colella, and F.B. Prinz. *Fuel Cell Fundamentals*. Wiley, Hoboken, NJ, 2006.

[49] T. Okada, G. Xie, and M. Meeg. Simulation for water management in membranes for polymer electrolyte fuel cells. *Electrochimica Acta*, 43(14-15):2141–2155, 1998.

[50] U. Pasaogullari and C.-Y. Wang. Two-phase modeling and flooding prediction of polymer electrolyte fuel cells. *Journal of the Electrochemical Society*, 152(2), 2005.

[51] N. Pekula, K. Heller, P. Chuang, A. Turhan, M. Mench, J. Brenizer, and K. Unlu. Study of water distribution and transport in a polymer electrolyte fuel cell using neutron imaging. *Nuclear Instruments and Methods in Physics Research Section A: Accelerators, Spectrometers, Detectors and Associated Equipment, Proceedings of the Fifth International Topical Meeting on Neutron Radiography*, 542:134–141, 2005.

[52] J.T. Pukrushpan, H. Peng, and A.G. Stefanopoulou. Modeling and analysis of fuel cell reactant flow for automotive applications. *Journal of Dynamic Systems, Measurement and Control*, 126(1):14–25, 2004.

[53] J.T. Pukrushpan, A.G. Stefanopoulou, and H. Peng. Controlling fuel cell breathing. *IEEE Control Systems Magazine*, 24(2):30–46, 2004.

[54] N. Rajalakshmi, P. Sridhar, and K.S. Dhathathreyan. Identification and characterization of parameters for external humidification used in polymer electrolyte membrane fuel cells. *Journal of Power Sources*, 109, 2002.

[55] R. Reid. Humidification of a pem fuel cell by air-air moisture. U.S. Patent number 6403249, June 2002.

[56] P.H. Rodatz. *Dynamics of the Polymer Electrolyte Fuel Cell: Experiments and Model-Based Analysis*. PhD thesis, Swiss Federal Institute of Technology, ETH, 2003.

[57] A.L. Schilter, D.A. McKay, and A.G. Stefanopoulou. Parameterization of fuel cell stack voltage: Issues on sensitivity, cell-to-cell variation, and transient response. *Proceedings of the ASME 4th International Conference on Fuel Cell Science, Engineering and Technology*, FUELCELL2006-97177, 2006.

[58] P. Setlur, J.R. Wagner, D.M. Dawson, and E. Marotta. An advanced engine thermal management system: Nonlinear control and test. *IEEE/ASME Transactions on Mechatronics*, 10(2), 2005.

[59] Y. Shan, S.-Y. Choe, and S.-H. Choi. Unsteady 2d pem fuel cell modeling for a stack emphasizing thermal effects. *Journal of Power Sources*, 165:196–209, 2007.

[60] H. Shimanuki, T. Katagiri, M. Suzuki, and Y. Kusano. Humidifier for use with a fuel cell. U.S. Patent number 6471195, October 2002.

[61] S. Shimpalee, D. Spuckler, and J.W. Van Zee. Prediction of transient response for a 25-cm2 pem fuel cell. *Journal of Power Sources*, 167:130–138, 2007.

[62] J.B. Siegel, D.A. McKay, and A.G. Stefanopoulou. Modeling and neutron imaging of water accumulation in low temperature fuel cells. *Proceedings of the American Controls Conference*, Seattle, WA, 2008.

[63] J.-J. Slotine and W. Li. *Applied Nonlinear Control*. Prentice-Hall, Inc., 1991.

[64] Sonntag, Borgnakke, and Van Wylen. *Fundamentals of Thermodynamics*. John Wiley and Sons, 2003.

[65] T.E. Springer, T.A. Zawodzinski, and S. Gottesfeld. Polymer electrolyte fuel cell model. *Journal of the Electrochemical Society*, 138(8), 1991.

[66] D. Staschewski. Internal humidifying of pem fuel cells. *International Journal of Hydrogen Energy*, 21(5), 1996.

[67] G.E. Suares and K.A. Hoo. Parameter estimation of a proton-exchange membrane fuel cell using voltage-current data. *Chemical Engineering Science*, 55:2237–2247, 2000.

[68] G.E. Suares and K.A. Kosanovich. Parameter and state estimation of a proton-exchange membrane fuel cell using sequential quadratic programming. *Industrial and Engineering Chemical Research*, 36:4264–4272, 1997.

[69] J.H. Taylor. Describing functions. In *Electrical Engineering Encyclopedia*. John Wiley and Sons, Inc., New York, 1999.

[70] T.A. Trabold, J.P. Owejan, D.L. Jacobsen, M. Arif, and P.R. Huffman. In situ investigation of water transport in an operating pem fuel cell using neutron radiography: Part i-experimental method and serpentine flow field results. *International Journal of Heat and Mass Transfer*, 49:4712–4720, 2006.

[71] C. Vermillion, J. Sun, K. Butts, and A. Hall. Modeling and analysis of a thermal management system for engine calibration. In *Proceedings of the 2006 IEEE, International Conference*, Oct. 2006.

[72] Y. Wang and C.Y. Wang. Transient analysis of polymer electrolyte fuel cells. *Electrochimica Acta*, 50:1307–1315, 2005.

[73] Y. Wang and C.Y. Wang. Dynamics of polymer electrolyte fuel cells undergoing load changes. *Electrochimica Acta*, 51:3924–3933, 2006.

[74] Y. Wang and C.Y. Wang. Two-phase transients of polymer electrolyte fuel cells. *Journal of the Electrochemical Society*, 154(7):B636–B643, 2007.

[75] W.S. Wheat, B.J. Clingerman, and M.K. Hortop. Electronic by-pass control of gas around the humidifier to the fuel cell. U.S. Patent number 6884534, April 2005.

[76] H. Yamada and Y. Morimoto. Practical approach to polymer electroyte fuel cell modeling. *Research and Development Review of Toyota CRDL*, 39(3), 2004.

[77] J.S. Yi and T.V. Nguyen. An along the channel model for proton exchange membrane fuel cells. *Journal of the Electrochemical Society*, 145(4), 1998.

[78] L. You and H. Liu. A two-phase flow and transport model for the cathode of pem fuel cells. *International Hournal of Heat and Mass Transfer*, 45:2277–2287, 2002.

[79] T. Zawodzinski, C. Derouin, S. Radzinski, R. Sherman, V. Smith, T. Springer, and S. Gottesfeld. Water uptake by and transport through nafion 117 membranes. *Journal of the Electrochemical Society*, 140(4), 1993.

[80] T. Zawodzinski, M. Neeman, L.O. Sillerud, and S. Gottesfeld. Determination of water diffusion coefficients in perfluorisulfonate ionomeirc membranes. *Journal of Physical Chemistry*, 95, 1991.

[81] T. Zawodzinski, T. Springer, F. Uribe, and S. Gottesfeld. Characterization of polymer electrolytes for fuel cell applications. *Solid State Ionics*, 60, 1993.

[82] J. Zhang, D. Kramer, R. Shimoi, Y. Ono, E. Lehmann, A. Wokaun, K. Shinohara, and G.G. Scherer. In situ diagnostic of two-phase flow phenomena in polymer electrolyte fuel cells by neutron imaging: Part b. material variations. *Electrochimica Acta*, 51:2715–2727, 2006.